ABSTRACT

Title of dissertation: FLOW AND INTERFACIAL DYNAMICS
IN VASCULAR VESSELS AND MICROFLUIDICS

Yechun Wang, Doctor of Philosophy, 2007

Dissertation directed by: Professor Panagiotis Dimitrakopoulos
Department of Chemical and Biomolecular Engineering

This dissertation investigates the hemodynamic forces on endothelial cells and leukocytes adherent on vascular vessels as well as the interfacial dynamics of droplet motion in microfluidic channels. In addition, we develop a novel three-dimensional spectral boundary element algorithm for interfacial dynamics in Stokes flow.

The hemodynamic forces exerted on endothelial cells or white blood cells adhered to the inner wall of vascular vessels affect the physiological behavior of these cells via mechano-transduction or receptor-ligand binding. The current study investigates the relative importance and nature of the two components of the hemodynamic force, i.e., the shear and normal force, exerted on the cell. We consider a wide range of vascular vessels (from capillaries to arteries) and the spreading angles of the cell. Based on computational investigation and scaling analysis, our study demonstrates that the normal force contributes significantly to the total force on the cell and its influence is much more substantial in small vessels. We also show that the spreading of the cell on the vessel wall should not be ignored especially in small vessels. Our results may also be applied to the fluid forces on other protuberances of biological nature attached to vascular vessels (e.g. cancer cells and biofilm) and to the fluid forces over humps in microfluidic channels and porous media.

In addition, we develop a novel three-dimensional spectral boundary element algorithm for interfacial dynamics in Stokes flow by utilizing a Hermitian interfacial smoothing and an element-based adaptive mesh reconstruction. The main attraction of this approach is that it exploits all the benefits of the spectral methods (i.e., exponential convergence and numerical stability) without being affected by the disadvantage of the spectral methods employed in volume discretization which create denser systems.

We also investigate the droplet motion in confined geometries which is primarily motivated by the recent development of microfluidic devices and has applications in the enhanced oil recovery, lubrication and coating processes. Our study on the inertialess motion of a buoyant droplet left to rise (or sediment) near a vertical solid wall reveals the influence of the Bond number and viscosity ratio on the droplet rising and migration velocity. We also show that analytical solutions fail to predict the correct droplet migration velocity.

In addition, we consider the pressure-driven motion of a surfactant-free droplet in a square micro-channel where we focus our interest on droplets whose size is comparable to the channel size. The influence of the capillary number, viscosity ratio and drop size on the droplet deformation and traveling velocity is investigated.

FLOW AND INTERFACIAL DYNAMICS IN VASCULAR VESSELS AND MICROFLUIDICS

by

Yechun Wang

Dissertation submitted to the Faculty of the Graduate School of the
University of Maryland, College Park in partial fulfillment
of the requirements for the degree of
Doctor of Philosophy
2007

Advisory Committee:

Professor Panagiotis Dimitrakopoulos, Chair/Advisor
Professor Raymond A. Adomaitis
Professor Kyu Yong Choi
Professor Kenneth Kiger
Professor Evanghelos Zafiriou

Acknowledgements

My sincere gratitude goes to my advisor, Professor Panagiotis Dimitrakopoulos for his advice, support and patience in guiding my graduate study. I would never accomplished my projects without his encouragement and motivation. In addition, from him I also learned and developed good attitudes in research and grasped the necessary skills in scientific writing. I would also like to acknowledge my committee members, Professors Raymond Adomaitis, Kyu Yong Choi, Kenneth Kiger and Evanghelos Zafiriou for their valuable time and insight.

I am grateful for the discussion and friendship of Professor Dimitrakopoulos' group members Inuka Dissanayake and Walter Dodson, as well as all the Chinese graduate students in the department. I am also thankful to the staff of the Department of Chemical and Biomolecular Engineering for their kind assistance in my study.

I own my gratitude to my dearest parents, Feng Wang and Hui Yang, and my husband, Chao You, for their love and support. I would also like to thank my friends and host family here in the United States for their kindness and companionship.

This research was supported in part by the National Science Foundation (grant CTS-0218770), the Petroleum Research Fund of the American Chemical Society, and the National Center for Supercomputing Applications in Illinois.

Table of Contents

List of Figures

Chapter 1

Introduction

This dissertation considers the following projects: i) the flow in vascular vessels and the hemodynamic forces exerted on the biological cells adhered to the surface of a blood vessel, ii) the development of a three-dimensional spectral boundary algorithm for interfacial dynamics in Stokes flow, iii) the buoyancy-driven motion of a droplet moving along a vertical solid wall, and iv) the interfacial dynamics in a microfluidic channel. In this chapter, background information is provided for all these projects.

1.1 Flow in Vascular Vessels

In physiological systems, the hemodynamic forces exerted on endothelial cells play a pivotal role in the mechano-transduction phenomena (which relates the hemodynamic forces received by endothelial cells and the chemical/biological signals they send out) [19, 26, 27, 36, 42, 67, 72, 74, 96]. Balanced by the receptor-ligand binding forces [28, 40], hemodynamic forces are also of great importance in the adhesion of the leukocytes onto the surface of blood vessels. Other protuberances in vascular vessels such as the blood clots and cancer cells are also subject to the influence of the hemodynamic force and its components [10].

The hemodynamic forces exerted on biological cells (either endothelial cells or leukocytes) protruding from the blood vessel wall have been determined by a variety of computational models. Hazel and Pedley [34] studied the hemodynamic force on vascular endothelial cells in large arteries. The cell was modeled as an ellipsoidal solid protuberance, while the artery was simplified into a solid plane due to the large diameter of the artery relative to the cell size. Several combinations of the cell height, length and width were considered to determine the cell configuration which minimizes the total hemodynamic force on the cell. Gaver and Kute [28] modeled a micro-channel and the adhered endothelial cell or leukocyte as two parallel plates and a semi-circular bulge. A two-dimensional flow between the plates were assumed. The lubrication theory was then employed in the study to validate the numerical results.

Studies have considered the fluid forces on leukocytes in post-capillary vessels by modeling the cells as solid spheres and the vessels as cylindrical tubes. Chapman and Cokelet [9, 10] determined the drag force on a single adherent leukocyte as a function of the leukocyte-to-vessel diameter ratio and the Reynolds number based on dimensionless analysis, experiments and computations. They showed that the drag force increases considerably with the cell size in small vessels. The same authors later extended their study to multiple adherent leukocytes in post-capillary vessels [11]. They found that the drag force on a leukocyte may be greatly affected by the relative configuration of neighbor leukocytes. Similar results were reported by Sugihara-Seki and Skalak [77, 78]. In a later study, Sugihara-Seki [79] showed that for moderate and small vessels, the flow around an adherent leukocyte in a cylindrical vessel cannot be

approximated by a parallel-plate channel. Sugihara-Seki and Schmid-Schonbein [80] also determined the shear stress distribution on the leukocyte membrane and its vicinity for adherent, rolling and free-suspended leukocytes.

In the afore-mentioned studies the surrounding liquid was modeled as a Newtonian fluid, and the cells were considered as rigid spheres or protuberances. Das, Johnson and Popel [16] determined the flow resistance due to leukocyte adhesion by modeling the surrounding liquid as a non-Newtonian Casson fluid except very close to the vessel wall. Based on that study, the increase of vascular resistance due to the leukocyte adhesion is smaller for a non-Newtonian fluid than that for a Newtonian fluid, but the difference is rather small. Liu and Wang accounted for the cell's interfacial deformation by considering three possible models (a single drop, a compound drop and a nucleus drop) for a two-dimensional adherent leukocyte in steady shear flow [48]. Models to describe the receptor-ligand bindings for cell adhesion have also been employed, e.g. [40, 56].

Our interest in these physical systems focuses on determining the nature of the hemodynamic force on these cells as well as the relative importance of the two components of the hemodynamic force, i.e., the shear stress and the normal force. We emphasize that previous studies, mainly in the last two decades, have attributed the behavior, or changes in the behavior, of the endothelium to the influence of one of the two components of the hemodynamic force, i.e., the influence of the shear stress. For example, the shear stress was found to affect the production of prostacyclin and nitric oxide [26, 27], the endothelial hydraulic conductivity through signal transduction [74], and the regulation of occludin content and phosphorylation [19].

The ability of endothelial cells to induce adhesion and migration of flowing enutrophils was found to be affected by the magnitude of shear stress in the presence of tumor necrosis factor-a [72]; the ability was also found to be affected by oscillatory shear stress [42]. The endothelial surface layer (glycocalyx) was found to act as a mechano-transducer of the fluid shear stress to the actin cortical cytoskeleton of the endothelial cells [96]. The biomechanical forces also affect the endothelial structure and functions such as the permeability to macromolecules, lipoprotein accumulation and the repair near branch points [67]. In addition, shear stress acting at the endothelium surface was found to produce rapid deformation of intermediate filament networks [36]. Thus, the influence of the second component of the hydrodynamic force on the endothelium, i.e., the normal force or pressure, has been overlooked.

In Chapter 4, we focus on the hemodynamic forces exerted on protuberances of biological nature in vascular vessels, such as endothelial cells, adherent leukocytes and cancer cells, as well as the blood clots formed during coagulations [10]. A wide range of spreading angles and vascular vessels are considered. The nature of the normal and shear force components, as well as their relative importance on the adherent cells are identified. We point out the importance of the normal force exerting on the endothelial cells and leukoctyes adherent to the inner surface of blood vessels, and we expect to inspire experimental or clinical studies on the normal force affecting the cell behavior. A comprehensive study on this topic, via both numerical calculations and scaling analysis, has been included in our recent publications [93, 94].

1.2 Interfacial Dynamics in Stokes Flow

Studies on particle movement in wall-bounded flows have been conducted ever since the discovery by Segue and Silberberg [68, 69], who demonstrated that neutrally buoyant rigid particles moving in a Poiseuille flow experience a migration towards the center of the flow and tend to accumulate in an annulus with a well-defined radius. The same phenomenon has also been observed in deformable red blood cells migrating in blood vessels as well as in rigid glass tubes.

The study on the deformation and migration of neutrally buoyant droplets in micro-channels is intrigued by the recent development of microfluidic devices. For example, micro-channels are employed for droplet sorting and fission [84, 47]. Droplets moving in microfluidic channels are utilized as "micro-reactors" in order to control chemical reactions on the milli-second scale [76]. The theoretical study on the deformation of the fluid droplets in the micro-channels may give advice on appropriate design or operation of microfluidics devices for stabilizing (e.g. in foam generation) or eliminating (e.g. in fuel cells) droplets.

Besides microfluidics, non-wetting droplets in micro-channels are also encountered in other industrial processes. In the lubrication process, lubricants usually contain a small amount of immersed bubbles altering the performance of journal bearings and squeezing film dampers [70]. According to the theoretical approach used by Bretherton [6], the equilibrium shape of an elongated droplet (the size of which is much larger than the width of the solid channel) in capillaries can be divided into three regions: bubble cap, transition region and the uniform film region.

The film thickness of the third region is of great interest in the enhanced oil recovery technology and coating process. In the enhanced oil recovery, foam is generated within the underground porous media to displace the oil. An accurate estimation of the wetting film thickness between the long droplet and the pore wall is desired in order to predict the percentage of recoverable oil. In the coating process, the wetting film thickness is also a direct measure of the coating load in monolithic channels [46]. The fundamental physics of bubble behavior in micro-channels is also essential in the operating and design of fuel cells, e.g. the removal of CO_2 bubbles in the anode channel of a direct methanol fuel cell(DMFC) [51]. In addition, the investigation on the dynamics of droplets moving in solid tubes or channels may provide information on the development of prescription to destroy or destabilize intra-vascular bubbles which occlude blood vessels and may lead to vital organ damage or sickness [18], e.g. the decompression sickness suffered by deep sea divers.

In order to provide physical insight for the interfacial dynamics in wall-bounded flows, we analyze the droplet motion in the following two cases: i) the buoyancy-driven motion of a droplet along a vertical solid wall and ii) the droplet dynamics in microfluidic channels.

1.2.1 Buoyancy-Driven Motion of a Droplet Along a Solid Wall

Determining the rising or sedimenting velocity of droplets near a wall is pivotal for designing and predicting the efficiency of processes involving multi-phase flows. Since 1960's, people have been investigating the motion a spherical-like particle (either fluid or solid spheres) moving parallel to a single infinite solid wall or between

parallel plates [31, 33, 43, 58, 70, 71, 81, 82, 83, 91, 101]. Recently, theoretical and experimental studies started to consider deformable droplets moving along solid walls by shear or Poiseuille flows [75, 52, 89, 90]. Efforts were also made to the buoyancy driven motion of droplets in an otherwise quiescent fluid. Magnaudet, Takagi and Legendre [52] analytically investigated the drag and deformation of a slightly deformed droplet by shear flow as well as by buoyancy along a solid wall at low Reynolds numbers. Takemura, Takagi, Magnaudet and Matsumoto [81], Takemura [83], and Takemura and Magnaudet [82] experimentally determined the drag acting on a spherical bubble rising near a vertical wall in a quiescent liquid for small and moderate Reynolds numbers respectively. Zeng, Balachandar and Fischer [101] performed numerical simulations for a rigid sphere at finite Reynolds numbers. Nevertheless, to our knowledge no numerical determination for the wall effect on a deformable droplet rising or sedimenting in a quiescent liquid at low Reynolds number has been carried out so far.

In Chapter 5, we investigate the inertialess motion of a buoyant surfactant-free droplet left to rise from an initially spherical shape close to a vertical wall. This problem has been included in the recent analytical study of Magnaudet, Takagi and Legendre [52] who considered the effects of deformation, inertia and linear shear flow on the motion of a buoyant droplet near a solid vertical wall. We note that the afore-mentioned analytical investigation is based on quasi-steady conditions, i.e., the time plays no direct role in the droplet motion. Thus, the goal of the current study is to investigate the initial transient effects on the droplet motion. We also compare our numerical results with the analytical predictions [52] to verify their

range of validity. Of particular importance is the verification (or rejection) of the analytical prediction that the direction of lateral migration depends on the viscosity ratio [52]. This study has been included in our recent publication [95].

1.2.2 Droplet Dynamics in a Microfluidic Channel

A plethora of studies have been conducted to investigate the motion of a long droplet/bubble with an open end displacing the wetting fluid filled in cylindrical capillaries. Bretherton [6] and Chen[12] both observed from their experiments that the film thickness in the uniform film region monotonically decreases as the capillary number $Ca = \mu U_b/\gamma$ decreases until it approaches a plateau at low Ca. The bubble velocity is denoted as U_b, and γ is the interfacial tension. Bordan and Pallinti [5] experimentally examined the buoyancy-driven motion of a viscous droplet ($\lambda \neq 0$) through a vertical cylindrical capillary. The results showed that the thickness of the liquid film surrounding a large droplet increases with the Bond number and approaches a plateau at high Bond number B_d. For bubbles ($\lambda = 0$), Bretherton [6] derived by lubrication theory that the film thickness is proportional to $Ca^{2/3}$ for vanishing capillary number Ca. By an arc-length formulation of a composite lubrication equation, Ratulowski and Chang [66] extended Bretherton's analysis [6] to higher capillary numbers. Hodges, Jensen and Rallison [41] theoretically investigated the effect of viscosity ratio λ on the drop motion and the film thickness. They predicted that the film thickness increases monotonically with λ until it reaches a plateau when $Ca^{-1/3} \ll \lambda \ll Ca^{-2/3}$ and then falls down as $\lambda \to \infty$. Finite element analysis (Shen and Udell [73], Giavedoni and Saita [29, 30]) was also applied to

describe the steady-state shape of the bubble-liquid interface for the long bubble or air finger in the tube.

A few studies have been contributed to the investigation on drops whose size is comparable to the size of the tube. Ho and Leal [39] experimentally studied the shape and mobility (i.e., velocity) of a periodic array of droplets with size ranging from 0.7 up to 1.1 times the tube radius, and with a capillary number up to 0.1. Olbricht and Kung [57] expended the afore-mentioned study to include the capillary number of $O(1)$ and investigated the conditions that lead to droplet breakup. These experiments demonstrated the bullet-like droplet shape with a tapered nose and a blunt end, as a result of the shearing force on the interface. They also showed that the droplet speed is strongly correlated with the drop shape, and both of them are influenced significantly by the capillary number. The boundary integral equations were applied in the numerical studies (e.g. Tsai and Miksis [88], Martinez and Udell [53]) conducted for this problem. The droplet size ranges from 0.5 to 1.2 times of the tube radius. Axisymmetric conditions were applied. Coulliette and Pozrikidis [14] employed a fully three-dimensional boundary integral method incorporated with a periodic Green's function to study the motion of an array of droplets moving in the cylindrical tube. The situation of a droplet released off the centerline of the tube was also considered. However the drop size only ranged from 0.1 to 0.7 times of the tube radius, and the viscosity ratio was fixed as 1 due to the constraints of this particular numerical method.

Droplet behavior in non-axisymmetric (i.e., square, rectangular or elliptic) capillaries, however, has received less attention, although those capillaries may be

employed as models better than circular ones in describing the irregular and angular nature of porous media [46, 97]. Traditionally, the investigation of this problem was intrigued by the applications in porous media involving droplet mobilization, such as enhanced oil recovery which utilizes gas bubbles to displace oil remaining in the reservoir [65, 66]. More recently, the development of coating technologies, biomechanics and microfluidic devices has raised a great interest in the problem of droplet motion in channels with non-axisymmetric cross-sections. In the coating of monolithic structures in the manufacturing of catalytic converters, long bubbles with the end open (i.e., air fingers) are pushed through polygonal capillaries filled with another fluid, the thickness of the film left on the capillary wall is the critical parameter in determining the quality of the coating process [44, 46]. According to Hazel and Heil [35], a long air finger is believed to reopen collapsed airway suffering from lung diseases. The study on the pressure drop need to push a long bubble through a non-axisymmetric tube may provide information in the mechanism of the airway reopening problem. The bubbly flow has also been encountered in microfluidic devices such as high-density multi-chip modules in supercomputers, high-flux heat exchangers in aerospace systems, cryogenic cooling systems in satellites [4].

Previous studies concerning the interfacial dynamics in channels focused mostly on the motion of highly elongated bubbles (with a size much larger than that of the channel cross-section), or air fingers (long bubbles with one end open). Ransohoff and Radke [65] investigated the behavior of a long bubble or droplet under the weeping flow of a wetting liquid in a constricted noncircular capillary. Ratulowski and Chang [66] studied the problem of a neutrally buoyant long bubble with a constant

velocity pushed through a straight noncircular capillary. Lubrication analysis was employed to compute the pressure drop and wetting film thickness for a single bubble and bubble trains moving in square capillaries. Kolb and Cerro [44, 46] conducted both experimental studies and the lubrication analysis on the motion of an air finger in a square capillary. In their studies, the density difference between the bubble and the suspending fluid was taken into consideration. The flow field between the bubble and the square solid channel was determined experimentally via a sequential particle tracking technique [44] as well as analytically by assuming the bubble has a circular cross section [45]. Thulasidas, Abraham and Cerro [87] later augmented Kolb and Cerro's experiments by including the investigation of bubble-train flow in square capillaries. For a train of bubbles and an air finger bubble, they considered the bubble velocity and the volume fraction of the gas under the influence of the flow rates of feeding gas or liquid. Wong, Radke and Morris [97, 98] determined the pressure-velocity relation for a long bubble moving in polygonal capillaries in the limit of $Ca \to 0$. By employing the finite element analysis, Hazel and Heil [35] extended Wong *et al.*'s study [97, 98] into $Ca = O(1)$ for square capillaries, and also included in-depth investigation for the steady motion of a long bubble in both rectangular and elliptical capillaries.

So far, to our knowledge the only computational study on the motion of a deformable droplet with a comparable size to the square channel was conducted by Mortazavi and Tryggvason [54]. They considered the droplet motion under the influence of the viscosity ratio, the capillary number and the Weber number. However, their study was restricted to 2D droplets at low Reynolds numbers.

In Chapter 6, we study the deformation and velocity of a deformable droplet moving in a micro-channel with a square cross-section. The droplet size is smaller than or comparable to the size of the channel. We emphasize that this study is important since droplets with comparable size to the channel is frequently encountered in microfluidics as well as in the enhanced oil recovery, while the previous results based on the theoretical analysis for very large bubbles are not applicable to the current problem. We first study the droplet deformation/shape and the velocity under the influence of the capillary number, viscosity ratio and the droplet size, as the droplet moves along the channel centerline. The last two influencing factors are encountered frequently in microfluidics, but have long been overlooked in previous studies for long bubbles or air fingers. We then proceed to study the cross-stream migration of a droplet released at a location off the channel centerline. To our knowledge, so far the cross-stream migration of the droplet in a micro-channel has not been investigated in a fully three-dimensional manner. The results of this study may provide guide to the operation and design of microfluidic devices such as foam generation or droplet sorting devices.

1.3 Summary

The spectral boundary element method [21, 37] is employed to analyze the hemodynamic force and its components (i.e., shear stress and normal force) over a biological cell (endothelial cells or leukocytes) adhered on the surface of blood vessels. The importance of this study lies in the fact that the hemodynamic forces play a pivotal

role in the behavior of vascular endothelial cells via mechano-transduction, as well as in the adhesion of leukocytes onto the blood vessel wall. Our study on both the force and the local stress over the cell surface suggests that the normal force contributes significantly to the total force and thus cannot be neglected. For less spread leukocytes, cancer cells or blood clots adhering to the surface of blood vessels, the effects of the normal force are even more pronounced. A scaling analysis is employed to provide more physical insight for the understanding of the nature of the fluid force components. The conclusion of this study may affect the studies on cell adhesion and the progress of associated diseases. Moreover, our study also helps explain the nature of fluid forces over protuberances in microfluidics and porous media, e.g. the ones formed by the adhesion of capsules and cells in microfluidic devices and biofilm formation.

In addition, we have developed a novel three-dimensional spectral boundary element algorithm for interfacial dynamics in Stokes flow as described in Chapter 3. The main attraction of this approach is that it exploits all the benefits of the spectral methods (i.e., exponential convergence and numerical stability) with the versatility of the finite element method (i.e., the ability to handle the most complicated geometries). Our method also exploits all the benefits of the boundary element techniques, i.e., reduction of the problem dimensionality and great parallel scalability. Our algorithm is the only available high-order methodology for the problem of droplet deformation in viscous flows. In order to preserve the continuity of the interfacial geometry and its derivatives, a suitable interfacial smoothing algorithm based on a Hermitian-like interpolation was developed. The smoothing technique preserves

the main advantage of the spectral method, i.e., , the exponential convergence in the interfacial accuracy as the number of spectral points increases. An adaptive mesh reconstructing procedure based on relative lengths of the spectral elements was also developed. By applying this algorithm to several interfacial problems in extensional and shear flows, we find that our results are in excellent agreement with experimental findings, analytical predictions and previous numerical computations.

This dissertation also consider the rising/sedimenting motion of a buoyant droplet along a vertical solid wall. The droplet velocity and deformation are closely monitored and evaluated under the influence of viscosity ratio and Bond number. We find that as the droplet rises along a vertical solid wall due to buoyancy, the droplet deforms and migrates away from the wall with a migration velocity inversely proportional to the square of the droplet-to-wall distance. In the circumstance of negligible inertia, the droplet deformation as well as the rate of deformation decide the velocity of the droplet migrating away from the wall. We closely compare our findings with previous analytical solutions, and find that the analytical models predicted quite well the rising velocity and the deformation of droplets near solid walls for the viscosity number $\lambda = O(1)$ and Bond number $B_d = O(1)$, but they erroneously predicted the droplet lateral motion towards the solid wall for $0.21 < \lambda < 3.12$.

As the last part of the dissertation, we examine the motion of a droplet moving in a microfluidic channel. We find larger droplets travel more slowly in the flow direction due to the confinement of the channel wall. Droplets with a larger capillary number or a smaller viscosity are found to translate with a higher velocity. In

addition, we compared the droplet behavior in the square channel with that in a cylindrical tube which has a radius identical to the circle subscribing the square channel. We note that the droplet deformation is smaller but the droplet speed is higher if the cross-section is square. For a droplet released at a position off the centerline, we find a larger droplet migrates faster towards the channel centerline. For a droplet with a larger capillary number, the higher deformation of the droplet interface may also accelerate the drop's migration towards the centerline.

Our study on the hemodynamic forces exerted on biological cells adhered on vascular vessels has resulted in two publications: the first paper was published in Physical Review Letters [93] while the second one was published in Physics of Fluids [94]. The novel interfacial algorithm along with the buoyancy-driven droplet motion near the solid wall was also published in Physics of Fluids [95]. Our work on the droplet dynamics in a microfluidic channel will be submitted for publication in the near future. In addition, our results were presented in national and international meetings including AIChE, the Society of Rheology and Burgers Program for Fluid Dynamics.

Chapter 2

Mathematical Formulation

Since the pioneering work of Youngren and Acrivos in 1970's [100], the boundary integral algorithm has been developed considerably and applied successfully in interfacial dynamics in Stokes flow. The main benefits of this approach are the reduction of the problem dimensionality by one and the great parallel scalability. In this chapter, we describe the basic boundary integral equation (BIE) in section 2.1. By combining with different boundary conditions and geometries, we then present a variety of BIEs employed by the computational studies of the physical problems discussed in this dissertation.

2.1 Boundary Integral Equations (BIE) for Stokes Flow

When the Reynolds number is sufficiently small, the inertial terms in the Navier-Stokes equations are neglected and the flow is governed by Stokes equations

$$\nabla \cdot \boldsymbol{\sigma} \equiv -\nabla p + \mu \nabla^2 \boldsymbol{u} = 0 \tag{2.1}$$

and the continuity

$$\nabla \cdot \boldsymbol{u} = 0 \tag{2.2}$$

where $\boldsymbol{\sigma}$ represents the stress tensor, p the dynamic pressure, μ the viscosity of the fluid and $\boldsymbol{u}$ the velocity vector.

By introducing the fundamental solutions S_{ij} and T_{ijk} for the three-dimensional Stokes equation (2.1) and the continuity (2.2), and by integrating over a volume of fluid bounded by a surface S_B shown in figure 2.1(a), the velocity at a point $\boldsymbol{x}_0$ on the surface may be expressed as the following boundary integral equation,

$$\boldsymbol{u}(\boldsymbol{x_0}) = -\frac{1}{4\pi\mu}\int_{S_B} (\boldsymbol{S}\cdot\boldsymbol{f} - \mu\boldsymbol{T}\cdot\boldsymbol{u}\cdot\boldsymbol{n})\, dS \tag{2.3}$$

which relates the velocity $\boldsymbol{u}$ at each point $\boldsymbol{x_0}$ along the boundary S_B by the surface integral of the stress and velocity over all the points $\boldsymbol{x}$ on the same boundary. The normal vector $\boldsymbol{n}$ points into the domain surrounded by the boundary S_B while the force vector $\boldsymbol{f}$ is defined by $f_j(\boldsymbol{x}) = \sigma_{jk}(\boldsymbol{x})n_k(\boldsymbol{x})$. The fundamental solution for the velocity S_{ij} and the corresponding stress T_{ijk} are given by

$$S_{ij} = \frac{\delta_{ij}}{r} + \frac{\hat{x}_i\hat{x}_j}{r^3} \tag{2.4}$$

$$T_{ijk} = -6\frac{\hat{x}_i\hat{x}_j\hat{x}_k}{r^5} \tag{2.5}$$

where $\hat{\boldsymbol{x}} = \boldsymbol{x} - \boldsymbol{x}_0$ and $r = |\hat{\boldsymbol{x}}|$. A detailed derivation may be found in Pozrikidis[60].

Equation (2.3) can be named as the "inner" equation since it solves for the fluid flow inside a specific boundary S_B shown in figure 2.1(a). The boundary S_B may be composed of both fluid and solid surface. By applying different boundary conditions, the "inner" equation itself may have numerous applications; one example is the numerical study of the hemodynamic forces exerted on biological cells adherent on the inner surface of a blood vessel as discussed in Chapter 4.

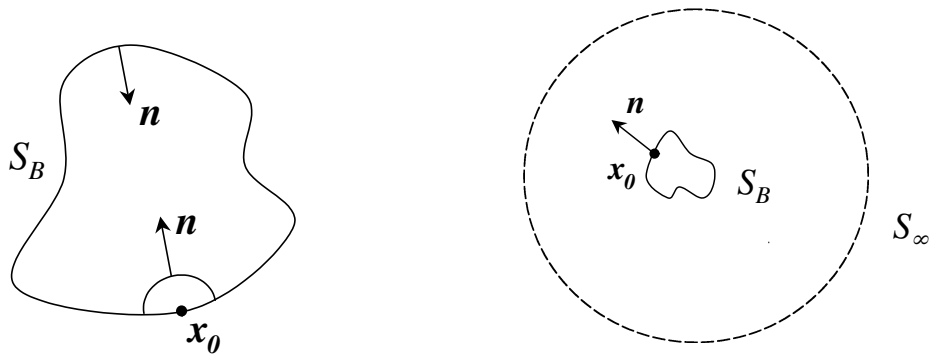

(a) (b)

Figure 2.1: Illustrations for the geometry of the BIEs (2.3) and (2.6).

Similar to the "inner" equation, an "outer" equation can be derived to express the flow field outside a boundary S_B as shown in figure 2.1(b). It is given by

$$\boldsymbol{u}(\boldsymbol{x}_0) - 2\boldsymbol{u}^{\infty}(\boldsymbol{x}_0) = -\frac{1}{4\pi\mu}\int_{S_B} (\boldsymbol{S}\cdot\boldsymbol{f} - \mu\boldsymbol{T}\cdot\boldsymbol{u}\cdot\boldsymbol{n})\, dS \tag{2.6}$$

where $\boldsymbol{u}^{\infty}$ is the velocity far from the surface boundary S_B and the normal vector $\boldsymbol{n}$ points into the flow (i.e., out of the boundary S_B). Both the "inner" and "outer" equations are important in deriving boundary integral equations for Stokes flow in various complex geometries which we are going to explore throughout the study.

2.2 BIE for a Free Suspended Droplet

Consider the case of a droplet with density ρ_1 and viscosity $\mu_1 = \lambda\mu$ suspended in an infinite fluid with density ρ_2 and viscosity $\mu_2 = \mu$, as illustrated in figure 2.2. The interfacial tension γ is assumed to be constant while $\boldsymbol{u}^{\infty}$ is the flow velocity far from the droplet interface S_B. The magnitude of the gravity acceleration is g. The

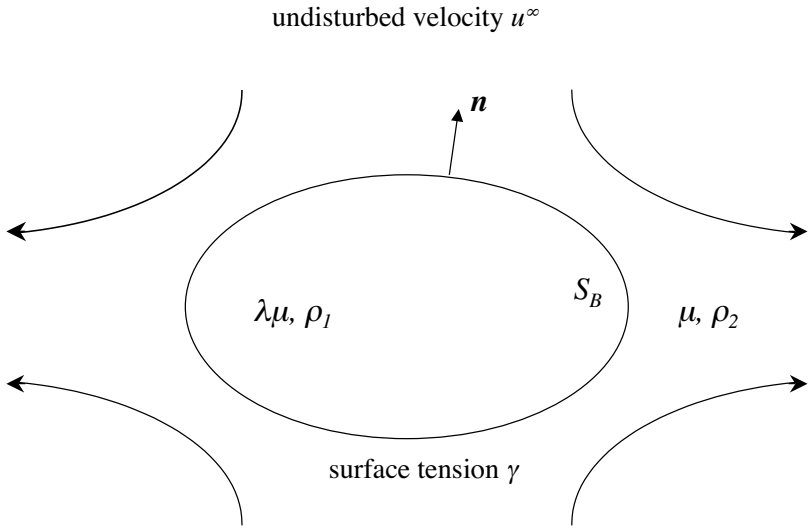

Figure 2.2: Illustration of a droplet freely suspended in an infinite fluid.

normal vector $\boldsymbol{n}$ points into the fluid outside the interface S_B.

The interior fluid is driven to flow by the exterior flow. The "inner" and "outer" equations (2.3) and (2.6) now apply to the interior and exterior domains, respectively. After subtracting equation (2.3) from equation (2.6), the velocity of a point $\boldsymbol{x}_0$ on the interface S_B is given as

$$\begin{aligned}&(1+\lambda)\boldsymbol{u}(\boldsymbol{x}_0) - 2\boldsymbol{u}^\infty(\boldsymbol{x}_0)\\ &= -\frac{1}{4\pi\mu}\int_{S_B}(\boldsymbol{S}\cdot\Delta\boldsymbol{f} - \mu(1-\lambda)\boldsymbol{T}\cdot\boldsymbol{u}\cdot\boldsymbol{n})\,dS\end{aligned} \tag{2.7}$$

where the velocity $\boldsymbol{u}$ and the jump of the interfacial stress $\Delta\boldsymbol{f}$ are defined by the interfacial boundary conditions:

$$\boldsymbol{u} = \boldsymbol{u}_1 = \boldsymbol{u}_2 \tag{2.8}$$

$$\Delta\boldsymbol{f} \equiv \boldsymbol{f}_2 - \boldsymbol{f}_1 = \gamma(\nabla\cdot\boldsymbol{n})\boldsymbol{n} + (\rho_2-\rho_1)(\boldsymbol{g}\cdot\boldsymbol{x})\boldsymbol{n} \tag{2.9}$$

where the subscripts "1" and "2" represent the internal and external flow, respectively. If $\Delta \boldsymbol{f}$ is known, then equation (2.7) becomes a Fredholm integral equation of the second kind in solving for the interfacial velocity $\boldsymbol{u}$.

2.3 BIE for a Droplet Moving Near a Solid Surface

We consider a droplet with density ρ_1 and viscosity $\lambda\mu$ suspended in a fluid with density ρ_2 and viscosity μ bounded by a solid wall with an arbitrary shape (note that the solid surface is much larger than the size of the droplet and it may be assumed to extend to infinity). The surface tension γ on the droplet interface Γ is assumed to be constant while $\boldsymbol{u}^\infty$ and $\boldsymbol{f}^\infty$ are the flow velocity and force far from the droplet. The magnitude of the gravity acceleration is g.

Consider a close domain formed by a fluid boundary S^f and the solid surface S^w around the droplet interface Γ, as shown in figure 2.3. We define the normal vector $\boldsymbol{n}$ on boundaries pointing to the fluid outside the droplet, the velocity at a point $\boldsymbol{x}_0$ on the boundary is given as,

$$\begin{aligned} \Omega \boldsymbol{u}(\boldsymbol{x}_0) - \Omega_0 \boldsymbol{u}^\infty(\boldsymbol{x}_0) &= -\int_\Gamma [\boldsymbol{S}\cdot(\Delta\boldsymbol{f}-\boldsymbol{f}^\infty) - \mu\boldsymbol{T}\cdot(\boldsymbol{u}(1-\lambda)-\boldsymbol{u}^\infty)\cdot\boldsymbol{n}]\, dS \\ &\quad -\int_{S^w} [\boldsymbol{S}\cdot(\boldsymbol{f}_2-\boldsymbol{f}^\infty) - \mu\boldsymbol{T}\cdot(\boldsymbol{u}_2-\boldsymbol{u}^\infty)\cdot\boldsymbol{n}]\, dS \end{aligned} \quad (2.10)$$

where $\Omega = 4\pi\mu(1+\lambda)$ and $4\pi\mu$ for $\boldsymbol{x_0}$ on Γ and S^w, respectively; $\Omega_0 = 4\pi\mu$ for $\boldsymbol{x_0}$ both on Γ and on S^w. The integral on S^f vanishes in the limit as the fluid boundary S^f approaches infinity.

Boundary conditions (2.8, 2.9) are applied for the velocity $\boldsymbol{u}$ and the jump in the interfacial stress $\Delta\boldsymbol{f}$ on the droplet interface. The boundary conditions on the

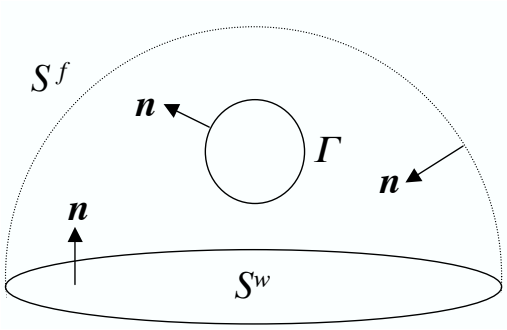

Figure 2.3: Droplet interface Γ enclosed by a fluid surface S^f and a solid plane S^w.

solid wall S^w and on the fluid boundary S^f far away from the droplet give

$$\boldsymbol{u} = 0 \quad \text{on} \quad \text{solid surface} \quad S^w \tag{2.11}$$

$$\boldsymbol{u} \to \boldsymbol{u}^\infty \quad \text{on} \quad \text{fluid surface} \quad S^f \tag{2.12}$$

2.4 BIE for a Droplet in a Microfluidic Channel

We consider the case when a droplet with density ρ_1 and viscosity $\lambda\mu$ translates through a solid capillary (i.e., either a channel or a tube) filled with a second fluid with density ρ_2 and viscosity μ. The surface tension γ on the droplet interface is assumed constant while $\boldsymbol{u}^\infty$ and $\boldsymbol{f}^\infty$ are the velocity and force of the Poiseuille flow far from the droplet in the capillary.

The droplet Γ is enclosed by a fluid boundary S^f at the inlet and outlet of the capillary and the capillary wall S^w as shown in figure 2.4. The normal vector $\boldsymbol{n}$ is defined to point into the fluid inside the capillary. Based on the Stokes equations and the continuity, the boundary integral equation for a point $\boldsymbol{x}_0$ on any of the

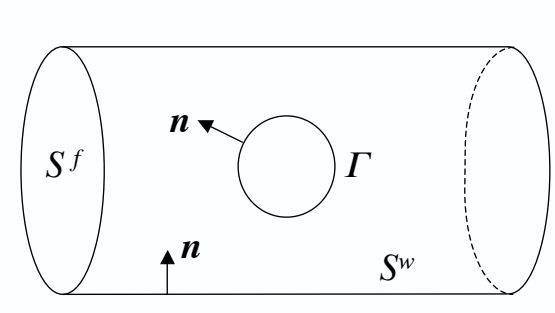

Figure 2.4: Drop interface Γ enclosed by a fluid surface S^f and a solid capillary S^w.

boundaries is given as,

$$\begin{aligned}\Omega \boldsymbol{u}(\boldsymbol{x}_0) &= -\int_\Gamma [\boldsymbol{S}\cdot\Delta\boldsymbol{f} - \mu(1-\lambda)\boldsymbol{T}\cdot\boldsymbol{u}\cdot\boldsymbol{n}]\,dS \\ &\quad -\int_{S^w} [\boldsymbol{S}\cdot\boldsymbol{f}_2 - \mu\boldsymbol{T}\cdot\boldsymbol{u}_2\cdot\boldsymbol{n}]\,dS \\ &\quad -\int_{S^f} [\boldsymbol{S}\cdot\boldsymbol{f}_2 - \mu\boldsymbol{T}\cdot\boldsymbol{u}_2\cdot\boldsymbol{n}]\,dS \end{aligned} \tag{2.13}$$

where $\Omega = 4\pi\mu(1+\lambda)$ for $\boldsymbol{x_0}$ on the droplet interface Γ, and $\Omega = 4\pi\mu$ on the fluid boundary S^f and the solid boundary S^w. The boundary conditions (2.8,2.9,2.11,2.12) are also applied.

Chapter 3

Numerical Method for Interfacial Dynamics

Considerable progress has been made to determine the deformation of droplets and bubbles in external flows. Several numerical methodologies have been developed based on low-order interpolation schemes [1, 49, 63, 64, 102]. In this study, we develop a three-dimensional spectral boundary element method, which includes a high-order discretization and interpolation algorithm (section 3.1), a time advancing scheme (section 3.2), an interfacial smoothing scheme which preserves the geometric continuity over the interface (section 3.3), as well as adaptive mesh reconstruction methods developed to adjust the interfacial discretization as the interface deforms (section 3.4). We then calculate the deformation of a single droplet freely suspended in an unbounded viscous flow in section 3.5. The properties of this interfacial algorithm, i.e., the convergence of the method with respect to the droplet deformation, are examined. Comparisons with previous studies have been made to verify the reliability and robustness of our algorithm.

3.1 Spectral Boundary Discretization

The boundary integral equations are solved using the spectral boundary element method as described in Muldowney and Higdon [55]. Its accuracy, efficiency and convergence have been demonstrated in applications involving rigid particles, deformable droplets and interacting particles. Higdon and Muldowney [37] applied this method in the study of the resistance functions for Stokes flow past spherical particles, droplets and bubbles in cylindrical tubes. Dimitrakopoulos and Higdon employed both the 2D [20] and 3D [21, 23, 24, 25] boundary element methods in studies on the displacement of droplets or fluid bridges from solid surfaces in Stokes flows. In addition, this method has been employed in studies on hemodynamic forces exerting on biological cells adhered to blood vessels [93, 94].

According to this method, the boundary is divided into a moderate number N_E of curvilinear quadrilateral surface elements (e.g. figure 3.1), each of which is mapped onto a two-dimensional domain in terms of the parametric variables ξ and η. The variables are zeros of orthogonal polynomials, such as Legendre, Chebyshev or Jacobi polynomials, on $[-1, 1]$. (In this study, we employ basis points of the Gauss-Lobatto quadrature [7] which facilitate the interfacial smoothing technique described in section 3.3.) If N_B basis points are used, then the geometry $\boldsymbol{x}$ can be represented by

$$\boldsymbol{x}(\xi, \eta) = \sum_{i=1}^{N_B} \sum_{j=1}^{N_B} \boldsymbol{x}(\xi_i, \eta_j) h_j(\eta) h_i(\xi) \tag{3.1}$$

where $h_i(\xi)$ and $h_j(\eta)$ are the $(N_B - 1)$-order Lagrangian interpolant polynomial. The physical variables $\boldsymbol{u}$ and $\boldsymbol{f}$ are represented similarly.

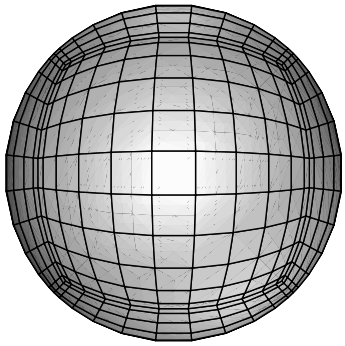

Figure 3.1: Spectral boundary element discretization of a spherical droplet into $N_E = 6$ elements. The figure illustrates Gauss-Lobatto Legendre distribution of nodal lines with $N_B = 12$ spectral points in each direction.

There are two types of points involved in boundary integral equations: i) the collocation points $\boldsymbol{x}_0$ on the left-hand side of the BIE where the equation is required to hold, and ii) the basis points $\boldsymbol{x}$ on the right-hand side where the physical variables $\boldsymbol{u}$ and $\boldsymbol{f}$ are defined. This method defines the collocation points as zeros of a Jacobi polynomial $P_N^{\alpha,\beta}$ with $\alpha = \beta > -1$, so that the collocation points are located in the interior of an element. As a result, the boundary integral equation holds even for singular points where the normal vector is not uniquely defines (this usually occurs at the edge of an element).

The discretized expressions for the geometry and the physical variables are substituted into the boundary integral equations yielding a linear system of $3N_E\,N_B^2$ algebraic equations

$$\boldsymbol{u} = \boldsymbol{A}\boldsymbol{f} + \boldsymbol{B}\boldsymbol{u} \tag{3.2}$$

The system matrices $\boldsymbol{A}$ and $\boldsymbol{B}$ are defined as integrals of the kernels $\boldsymbol{S}$ and $\boldsymbol{T}$ (see

equations (2.4) and (2.5)) and the basis functions over the set of the surface elements. The numerical integration is performed by Gauss-Legendre quadrature with the aid of variable transformations described by Higdon[55]. The BIEs, combined with the boundary data at the $N_E N_B^2$ basis points, yield, for a known interface, a consistent set of $3N_E N_B^2$ equations in $3N_E N_B^2$ unknowns which is solved using Gaussian elimination since the system matrix is dense.

3.2 Time-Integration Algorithm

In interfacial dynamics, the shape of the droplet $\boldsymbol{x}$ is a function of time t. In order to determine the interfacial shape, an explicit time-integration algorithm is employed to solve the kinematic condition at the droplet interface

$$\frac{\mathrm{d}\boldsymbol{x}}{\mathrm{d}t} = (\boldsymbol{u} \cdot \boldsymbol{n})\boldsymbol{n} + U_t \boldsymbol{t} \tag{3.3}$$

where the first term at the right-hand side denotes the contribution of the normal interfacial velocity while the second term includes some velocity tangential to the interface. Vector $\boldsymbol{n}$ is the normal vector of the known shape and $\boldsymbol{t}$ is a unit tangent vector of the interface. Note that the interfacial shape is determined by the normal interfacial velocity; the tangential velocity is employed to produce an even distribution of the spectral points during the time evolution of the interface. The interfacial tangential velocity may be given by

$$U_t \, \boldsymbol{t} = c_t[(\boldsymbol{u} \cdot \boldsymbol{t}_1)\boldsymbol{t}_1 + (\boldsymbol{u} \cdot \boldsymbol{t}_2)\boldsymbol{t}_2] \tag{3.4}$$

where c_t is a scalar determining the contribution of the tangential velocity. Vectors $\boldsymbol{t}_1$ and $\boldsymbol{t}_2$ are the two unit tangent vectors on the drop interface. Similar techniques

were employed in other boundary integral implementations, e.g. [1, 49, 50, 102].

An explicit Euler or Runge-Kutta method is employed for the time-integration. The explicit Euler scheme can be written as

$$\boldsymbol{x}(t+\Delta t) = \boldsymbol{x}(t) + \Delta t[(\boldsymbol{u}\cdot\boldsymbol{n})\boldsymbol{n} + U_t\boldsymbol{t}] \tag{3.5}$$

We determine the interfacial velocity $\boldsymbol{u}$ of the known shape $\boldsymbol{x}(t)$ from boundary integral equations, and then the discretized points of the interface are advanced by a time interval Δt to obtain the new shape $\boldsymbol{x}(t+\Delta t)$.

For the interfacial dynamics of a free suspended droplet, the time step Δt should be sufficiently small to ensure numerical stability according to the well-known Courant condition, which in dimensionless form may be written as

$$\Delta t < O(Ca\Delta x_{min}) \tag{3.6}$$

where Δx_{min} is the minimum length scale in a the computational problem, e.g. the minimum grid spacing or the distance between interfaces in close contact [15, 49, 64, 102, 103]. The capillary number Ca is a dimensionless number measuring the relative importance between the viscous force and the surface tension force. (The capillary number Ca, viscosity ratio λ, deformation parameter D, pertaining to the free suspended droplet under external flows will be described later in section 3.5.) In our computations, we reduce the time step if a lower capillary number is encountered, or if a larger N_B is employed. For gravity-only induced deformation, the time step should be reduced as the Bond number decreases [17]. The Courant condition is associated with the explicit nature of the time integration, and thus it is independent of the type of interfacial discretization. On the other hand, due to its high accuracy

nature, our method may not require as dense a numerical grid as low-order boundary element methods, and thus the required time step may be larger.

If we apply the advancing scheme described above without adequate geometric constraints, the resulting algorithm is unstable after a few time steps. Numerically, this instability is caused by the discontinuity at the edges of the spectral elements. Figure 3.2 shows the deformation of a free suspended droplet in a planar extensional flow with capillary number $Ca = 0.2$ and viscosity ratio $\lambda = 0.01$. The number of time steps is denoted as N_{st} while u_n is the maximum normal velocity at the interface. Although we have enforced coincidence of the basis points on the edges of the spectral elements, the discontinuity on the element edges can still be witnessed in figure 3.2(d) and the droplet interface breaks at the step $N_{st} = 156$, i.e., the time $t = 0.312$. We note that small differences in numerical accuracy across neighbor elements accumulate substantially with time after a few steps and eventually lead to the discrepancies at element edges.

A first-order smoothing technique is derived to resolve this problem. In every time step, the smoothing scheme adjusts the grid of each element so that the position, the tangent and the normal vectors on the element edges are continuous across the spectral elements. The details of the novel smoothing technique is described in the next section.

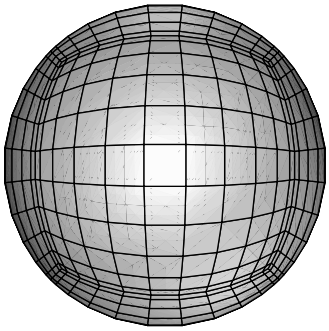

(a) $N_{st} = 0$, time $t = 0.000$,

D= 0.000, u_n= 1.59

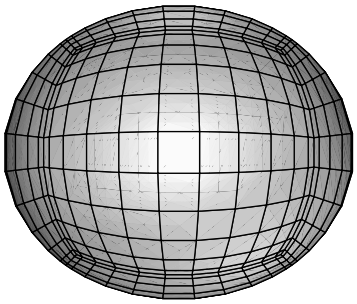

(b) $N_{st} = 30$, time $t = 0.060$,

D= 0.0877, u_n= 1.33

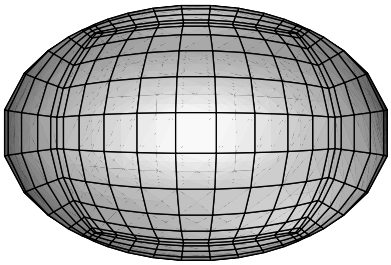

(c) $N_{st} = 90$, time $t = 0.180$,

D=0.206, u_n=0.890

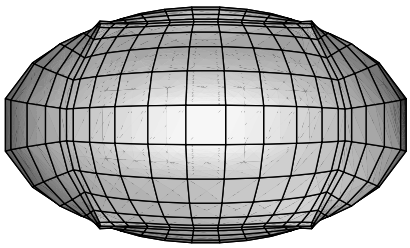

(d) $N_{st} = 140$, time $t = 0.280$,

D= 0.268, u_n= -281

Figure 3.2: The time evolution of a drop deforming in a planar extensional flow for $Ca = 0.2$ and $\lambda = 0.01$. A 4th-order Runge-Kutta (RK4) method without interfacial smoothing is employed with $N_E = 6$, $N_B = 12$ and $\Delta t = 2 \times 10^{-3}$. The droplet deformation parameter D will be defined in section 3.5.

3.3 Interfacial Smoothing

Our first-order smoothing scheme eliminates the discrepancies in the position, the tangent and normal vectors at the element edges across the spectral elements which are caused by the numerical advancing of the interface. In this section, we first describe how we smooth the position, the tangent and normal vectors at the element edges and then we explain how we update the position for all the points on each spectral element by a two-dimensional Hermitian interpolation.

Let the non-smoothed interfacial shape at time $t + \Delta t$, derived by the time integration of equation (3.3) above, be identified as $\boldsymbol{x}(\xi,\eta)$ where ξ and η are the two parametric variables describing the interface. We also define a local Cartesian coordinate system $\boldsymbol{x}^L$ at each point with the x_1^L- and x_2^L-axes in the tangent plane and the x_3^L-axis parallel to the normal vector $\boldsymbol{n}$. As shown in figure 3.3, the points a and b are two coincident points belonging to the consecutive elements A and B, respectively. The solid arrows represent the curvilinear coordinates (ξ, η) and the dashed arrows the local Cartesian coordinates (x_1^L, x_2^L). The normal vector $\boldsymbol{n}$ and the third local Cartesian coordinate x_3^L are not plotted. In the situation illustrated, the parametric variable η at the point a coincides with the variable ξ at the point b and they both point at the same direction. In fact, due to the surface discretization, other combinations are possible, e.g. ξ at the point a coincides with ξ at the point b in the opposite direction.

To perform the interfacial smoothing, we first average the position $\boldsymbol{x}$ of the

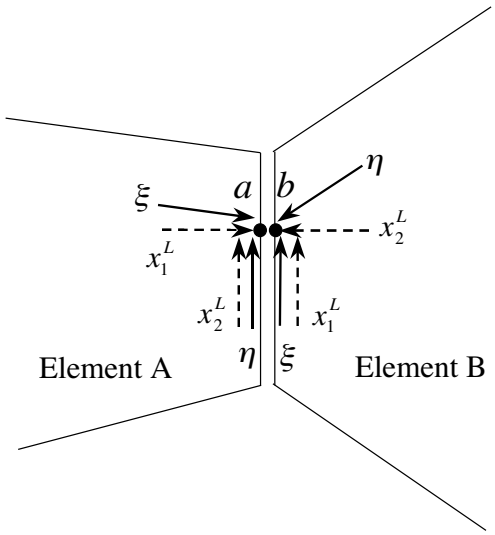

Figure 3.3: Illustration for the curvilinear coordinates (ξ, η) and the local Cartesian coordinates (x_1^L, x_2^L). Two neighbor elements A and B are displayed. The points a and b are two coincident points belonging to elements A and B, respectively, and should overlap after the interfacial smoothing.

edge points across neighbor elements

$$\boldsymbol{x}_a^{new} = \boldsymbol{x}_b^{new} = 0.5\,(\boldsymbol{x}_a^{old} + \boldsymbol{x}_b^{old}) \tag{3.7}$$

and then we calculate the geometric properties of the updated shape $\boldsymbol{x}^{new}$. In this way, for our specific example the derivatives $(\partial \boldsymbol{x}/\partial \eta)_a$ and $(\partial \boldsymbol{x}/\partial \xi)_b$ are identical. We next calculate the unit tangent vector

$$(\boldsymbol{t}_1^L)_a = \frac{\left(\frac{\partial \boldsymbol{x}}{\partial \eta}\right)_a \times \boldsymbol{v}_a}{\left|\left(\frac{\partial \boldsymbol{x}}{\partial \eta}\right)_a \times \boldsymbol{v}_a\right|} \tag{3.8}$$

where $\boldsymbol{v}_a$ is the non-unit normal at point a, $\boldsymbol{v}_a = (\partial \boldsymbol{x}/\partial \xi)_a \times (\partial \boldsymbol{x}/\partial \eta)_a$. The unit tangent $(\boldsymbol{t}_2^L)_b$ is found in a similar way. Note that the tangent vectors $(\boldsymbol{t}_1^L)_a$ and $(\boldsymbol{t}_2^L)_b$ lie on the x_1^L-axis at the point a and the x_2^L-axis at the point b, respectively.

In order to achieve continuity in this tangent direction, we average the unit tangent vectors,

$$(\boldsymbol{t}_1^L)_a^{new} = -(\boldsymbol{t}_2^L)_b^{new} = 0.5\left[(\boldsymbol{t}_1^L)_a^{old} - (\boldsymbol{t}_2^L)_b^{old}\right] \tag{3.9}$$

where the minus sign appears due to the specific geometry shown in figure 3.3.

At this point, both the position and the tangent vectors at the edge points are continuous. The next goal is to determine the updated first-order derivatives $(\partial \boldsymbol{x}/\partial\xi)_a^{new}$ and $(\partial \boldsymbol{x}/\partial\eta)_b^{new}$. From the tangent vectors, we calculate the unit normal vectors

$$\boldsymbol{n}_a^{new} = \frac{(\boldsymbol{t}_1^L)_a^{new} \times \left(\frac{\partial \boldsymbol{x}}{\partial \eta}\right)_a}{\left|(\boldsymbol{t}_1^L)_a^{new} \times \left(\frac{\partial \boldsymbol{x}}{\partial \eta}\right)_a\right|} \tag{3.10}$$

$$\boldsymbol{n}_b^{new} = \frac{\left(\frac{\partial \boldsymbol{x}}{\partial \xi}\right)_b \times (\boldsymbol{t}_2^L)_b^{new}}{\left|\left(\frac{\partial \boldsymbol{x}}{\partial \xi}\right)_b \times (\boldsymbol{t}_2^L)_b^{new}\right|} \tag{3.11}$$

Note that $\boldsymbol{n}_a^{new}$ and $\boldsymbol{n}_b^{new}$ are identical now due to the interfacial smoothing we have performed. In order to calculate the updated derivative $(\partial \boldsymbol{x}/\partial\xi)_a^{new}$, the following relations for the point a are applied

$$\boldsymbol{n}_a^{new} \cdot \left(\frac{\partial \boldsymbol{x}}{\partial \xi}\right)_a^{new} = 0 \tag{3.12}$$

$$\left(\frac{\partial \boldsymbol{x}}{\partial \xi}\right)_a^{new} \cdot \left(\frac{\partial \boldsymbol{x}}{\partial \eta}\right)_a = \left(\frac{\partial \boldsymbol{x}}{\partial \xi}\right)_a^{old} \cdot \left(\frac{\partial \boldsymbol{x}}{\partial \eta}\right)_a \tag{3.13}$$

$$\left|\left(\frac{\partial \boldsymbol{x}}{\partial \xi}\right)_a^{new}\right| = \left|\left(\frac{\partial \boldsymbol{x}}{\partial \xi}\right)_a^{old}\right| \tag{3.14}$$

The new derivative $(\partial \boldsymbol{x}/\partial\eta)_b^{new}$ can be found in a similar way.

So far, we have smoothed the position $\boldsymbol{x}$ and the first derivatives, $(\partial \boldsymbol{x}/\partial\xi)$ and $(\partial \boldsymbol{x}/\partial\eta)$, at the edge points across the spectral elements. We want to employ this updated information of the edge points to derive a smoothed interfacial shape.

For this, we generate $(N_B-4)\times(N_B-4)$ interior Jacobi points from the $N_B \times N_B$ Lobatto points (i.e., end and interior points) on each spectral element. By combining these Jacobi points with the smoothed position $\boldsymbol{x}$ and the first-order derivatives $(\partial \boldsymbol{x}/\partial\xi)$ and $(\partial \boldsymbol{x}/\partial\eta)$ at the edge points, a two-dimensional Hermitian interpolation is employed to produce a new set of $N_B \times N_B$ Lobatto points which represents the final smoothed interfacial shape at time $t+\Delta t$. The two-dimensional Hermitian interpolation involves two nested one-dimensional Hermitian interpolations. The specific one-dimensional Hermitian interpolation was derived in Dimitrakopoulos[22] and it is given by

$$\begin{aligned} f(x) = (x^2-1)^2 \sum_{i=1}^{M} \frac{1}{(x_i^2-1)^2} \prod_{j\neq i}^{M} \left(\frac{x-x_j}{x_i-x_j}\right) f(x_i) + \\ \prod_{j=1}^{M} \left(\frac{x-x_j}{-1-x_j}\right) \frac{(x-1)^2}{4}(x+1) f'(-1) + \\ \prod_{j=1}^{M} \left(\frac{x-x_j}{1-x_j}\right) \frac{(x+1)^2}{4}(x-1) f'(+1) + \\ \prod_{j=1}^{M} \left(\frac{x-x_j}{-1-x_j}\right) \frac{(x-1)^2}{4}[1+b_{(-1)}(x+1)] f(-1) + \\ \prod_{j=1}^{M} \left(\frac{x-x_j}{1-x_j}\right) \frac{(x+1)^2}{4}[1-b_{(+1)}(x-1)] f(+1) \end{aligned} \tag{3.15}$$

The function values $f(-1)$ and $f(+1)$ correspond to the refreshed position $\boldsymbol{x}$ of the edge points while the derivatives $f'(-1)$ and $f'(+1)$ correspond to the updated $(\partial \boldsymbol{x}/\partial\xi)$ or $(\partial \boldsymbol{x}/\partial\eta)$ of the edge points. The coefficients $b_{(-1)}$ and $b_{(+1)}$ are chosen to yield zero slope at the element edges,

$$b_{(-1)} = -\left[\sum_{j=1}^{M}\left(\frac{1}{x-x_j}\right) + \frac{2}{x-1}\right]_{x=-1} = \sum_{j=1}^{M}\left(\frac{1}{1+x_j}\right) + 1 \tag{3.16}$$

$$b_{(+1)} = +\left[\sum_{j=1}^{M}\left(\frac{1}{x-x_j}\right) + \frac{2}{x+1}\right]_{x=+1} = \sum_{j=1}^{M}\left(\frac{1}{1-x_j}\right) + 1 \tag{3.17}$$

We emphasize that, for each one-dimensional Hermitian interpolation, the position and the first derivative at the two edges count for 4 degrees of freedom which, combined with the $(N_B - 4)$ degrees of freedom of the interior Jacobi points, produce the same total number of degrees of freedom as the Lobatto points N_B. We also note that by employing our first-order smoothing scheme, we formally achieve the continuity of the position and the tangent/normal vectors at the edges of the spectral elements. However, for the problems we have studied in this thesis, our results show that this technique also achieves the continuity of the curvature at the element edges, i.e., the second-order derivative of the interfacial geometry.

Figure 3.4 shows that, by applying the smoothing scheme, the continuity of the droplet interface is preserved. The capillary number and the viscosity ratio are the same with those in figure 3.2, i.e., $Ca = 0.2$ and $\lambda = 0.01$. In contrast to figure 3.2(d), at time $t = 0.280$, the elements on the droplet interface smoothly connect with each other and the drop doesn't breakup even until time $t = 7.07$ where we stop our computation.

3.4 Adaptive Mesh Reconstruction

In strong flows, especially those corresponding to supercritical conditions, the droplet may elongate significantly. The droplet is also found to elongate when it is pushed through a micro-channel filled with another immiscible fluid. An interfacial neck may also appear under severe deformation. In those circumstances, the original spectral discretization may not be sufficient to describe the very deformed interfa-

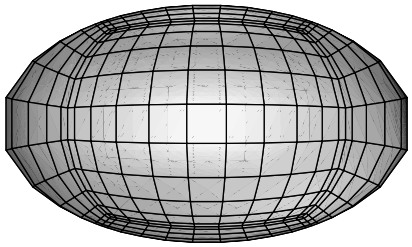

Figure 3.4: The time evolution of a drop deforming in a planar extensional flow for the same parameters as in figure 3.2 except that now the first-order interfacial smoothing is employed in each time step. The droplet shape is shown for time $t = 0.28$, i.e., step $N_s = 140$. The current deformation is $D = 0.267$.

cial shape. To resolve this issue, one may change one or both of the discretization parameters of the spectral boundary elements, i.e., N_E and N_B. In our current algorithm, it is more efficient to vary only the number of element, N_E.

Two distinct cases may be found in the mesh reconstruction since the spectral elements we employ are quadrilateral. First, the relevant length of a spectral element is increased above a prescribed maximum limit along only one curvilinear direction. In such a case the element is divided into two halves with $N_B \times N_B$ basis points, as shown in figure 3.5(a). This case may represent the development of an interfacial neck. On the other hand, the relevant length of a spectral element along both curvilinear directions is increased above the prescribed maximum limit. In such a case the element should be divided in both directions; our preference is to divide the element into 5 elements as shown in figure 3.5(b). This second case may stand

for the two ends of an elongated droplet which show large interfacial curvature. For each case, the opposite happens when the relevant length of a spectral element is decreased below a prescribed minimum limit. Under this circumstance, the reverse of the afore-mentioned process takes place; the element is combined with its neighbor(s) while $N_B \times N_B$ new basis points are defined on the resulting new element. The employed time step Δt is accordingly adjusted to satisfy the Courant condition, equation (3.6).

The goal of the adaptive mesh reconstruction is to produce a reasonable spectral element discretization of the interfacial shape with respect to the elements' arc lengths or the variation of curvature on the interface. In most computations involving significant droplet elongation, we perform necessary mesh reconstructions based on the measurement of the arc length ($L_{arc} = \int_{elem} dl$) of a spectral element. For problems involving surfaces in close contact, the gap between surfaces may be considered as another relevant length. Note that our procedure is based on the size of the spectral elements, and not of successive grid points; thus it requires a smaller number of comparisons and decision making operations.

This strategy has been employed to determine large deformations of droplets in supercritical conditions. Figure 3.6 demonstrates the interfacial shape of a droplet with $\lambda = 0.5$ and $Ca = 0.25$, a supercritical condition, in a planar extensional flow. The initial spherical shape is discretized into $N_E = 6$ spectral elements. As the drop deformation increases more elements are employed by dividing each of the two edges of the droplet into five new elements.

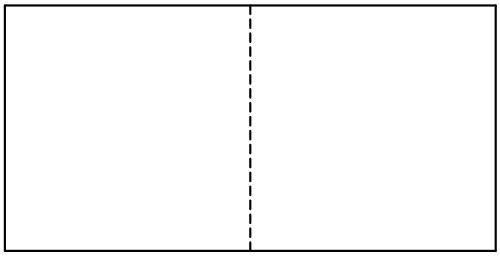

(a)

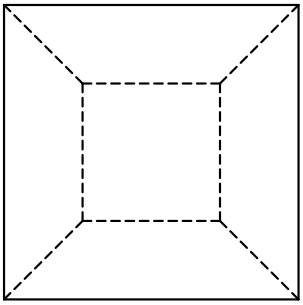

(b)

Figure 3.5: Layout for element division into (a) two, and (b) five elements. The solid line represents the original element while the dashed lines show the resulting elements after division.

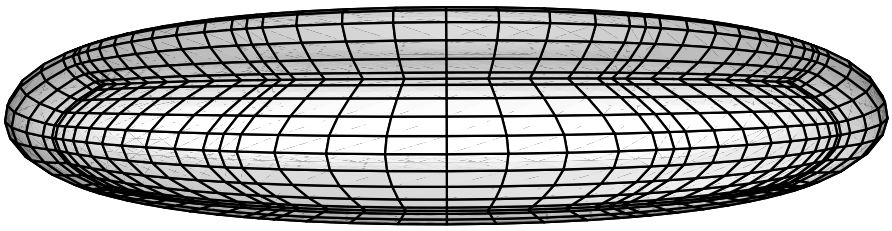

Figure 3.6: A significantly elongated droplet with $\lambda = 0.5$ and $Ca = 0.25$ at time $t = 1.35$ in a planar extensional flow. The current droplet deformation is $D = 0.61$. The length is increased by 126.5% while the width is reduced by 46%. The droplet evolves from an initially spherical shape with 6 elements. After dividing the two ends into 5 elements each, the current droplet interface contains 14 elements.

3.5 Interfacial Dynamics of a Free Suspended Droplet

The problem of interfacial dynamics of a free suspended droplet is governed by two dimensionless numbers: the viscosity ratio λ and the capillary number Ca given by

$$\lambda = \frac{\mu_1}{\mu} \tag{3.18}$$

$$Ca = \frac{\mu G a}{\gamma} \tag{3.19}$$

where μ_1 is the viscosity of the fluid inside the drop, μ is the viscosity of the imposed flow with $\boldsymbol{u}^\infty$ as the undisturbed velocity far from the droplet. The surface tension on the interface is denoted as γ. The constant G designates the shear rate of the external flow and a is the characteristic length of the droplet defined from the drop volume V as

$$a = \left(\frac{3V}{4\pi}\right)^{1/3} \tag{3.20}$$

The capillary number Ca measures two competing forces: the viscous force and the surface tension force. The viscous stress imposed on the interface by the exterior flow induces the flow inside the drop and causes the interfacial deformation, while the surface tension force resists the deformation. When an equilibrium state is reached, the surface tension force balances the viscous force so that the droplet deformation ceases. In this study, we assume there is no density difference between the droplet and the suspending fluid.

The droplet deforms from an initially spherical shape to an ellipsoid-like shape. The degree of deformation is measured via the parameter D defined by

$$D = \frac{L - S}{L + S} \tag{3.21}$$

where L is the length of the longest axis of the drop and S is that of the shortest axis. Equation (3.21) is especially suitable to describe the deformation of a free suspended droplet under the influence of external two-dimensional flows. Other deformation parameters may be employed for droplets deforming under other types of flows, e.g. Poiseuille flow. We identify the characteristic length of the drop a as the length scale of the problem, the velocity scale is Ga, and the time scale is $1/G$.

For a given droplet interface S_B, the boundary integral equation (2.7) and boundary conditions (2.8,2.9) can be applied. (Please refer to section 2.2 for a detailed explanation.)

Numerous tests have been performed to verify the robustness and the reliability of our algorithm for a free suspended droplet under external flows, e.g. the planar extensional flow with $\boldsymbol{u} = G(x, -y, 0)$ and the simple shear flow with $\boldsymbol{u} = G(y, 0, 0)$.

Comparisons have been made with previous numerical results, analytical predictions and experimental findings.

For a droplet deforming in an imposed planar extensional flow, we compared the the transient behavior of the deformation D with the numerical results by Bazhlekov, Anderson and Meijer [1]. For small capillary numbers, our numerical results are in excellent agreement with the analytical predictions by Taylor [85]. In the case of an external shear flow, a good agreement has been found between our computations and the experimental data by Guido and Villone [32]. We also compared with the experimental results of Bentley and Leal [2] for droplets deforming in a planar four-roll mill flow. Excellent agreements have been found in the deformation D and the droplet profiles at steady state. Detailed comparisons can be found in Ref. [92] and Ref. [95].

In this study, we consider the droplet dynamics near the critical conditions. Figure 3.7 shows the dynamics for a droplet with viscosity ratio $\lambda = 0.5$ in a planar extensional flow. The capillary number ranges from 0.1 to 0.2. The critical capillary number for this case is $Ca \approx 0.1355$ [2]. As shown in figure 3.7, the maximum normal velocity (i.e., the deformation speed) on the interface behaves differently at subcritical conditions and supercritical conditions. For subcritical capillary numbers, the maximum normal velocity is dramatically reduced as the deformation and time increases. Steady state may be achieved, as shown clearly for the curve of $Ca = 0.1$. For supercritical capillary numbers, the deformation speed first decreases slowly with the deformation and time, and then increases after the minimum is reached. No equilibrium shape can be obtained and thus the droplet

tends to stretch infinitely, or breaks into smaller droplets if disturbed.

One of the advantages of the spectral method is the exponential convergence in the numerical accuracy with the increase of the number of spectral points. To determine the convergence of our method, the droplet deformation has been calculated for different grid sizes by varying the number of basis points N_B on each spectral element. Figure 3.8 shows the exponential convergence in the numerical accuracy for the computation of the interfacial shape (i.e., deformation D) for a droplet with $\lambda = 0.5$ in a planar extensional flow. Both subcritical and supercritical capillary numbers are considered. We investigate two situations: i) only the normal velocity is applied to advance the interfacial spectral points, and ii) the interfacial tangential velocity contributes to improve the distribution of the spectral points on the interface. In both cases, our algorithm shows the typical exponential convergence of the spectral methods with the increasing number of spectral points $N = N_E \times N_B^2$. Moreover, the utilization of the tangential velocity $U_t \boldsymbol{t}$ produces a more uniform distribution of the interfacial points. As a result, the accuracy is improved up to almost two orders of magnitude. We emphasize that the difference in the interfacial accuracy between our spectral algorithm and low-order methods is dramatic since the latter commonly achieve linear convergence by increasing the number of the employed grid points.

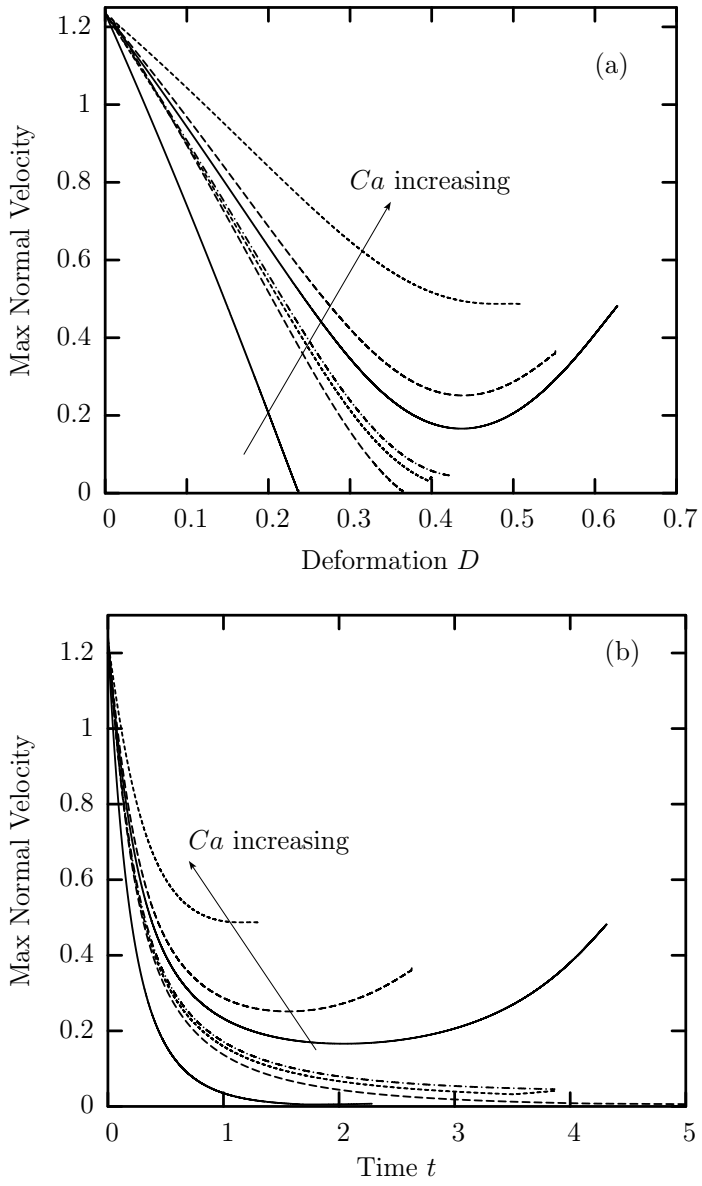

Figure 3.7: Dynamics near the critical condition for a droplet with viscosity ratio $\lambda = 0.5$ in a planar extensional flow: (a) the maximum normal velocity versus deformation D; (b) the maximum normal velocity versus time t. The capillary number varies $Ca = 0.1, 0.13, 0.1355, 0.138, 0.15, 0.16, 0.2$. Curves are generated by employing the 4th-order Runge-Kutta time-integration algorithm with $\Delta t = 1\times10^{-4}$ and the first-order smoothing technique. The tangential velocity is applied with $c_t = 0.2$.

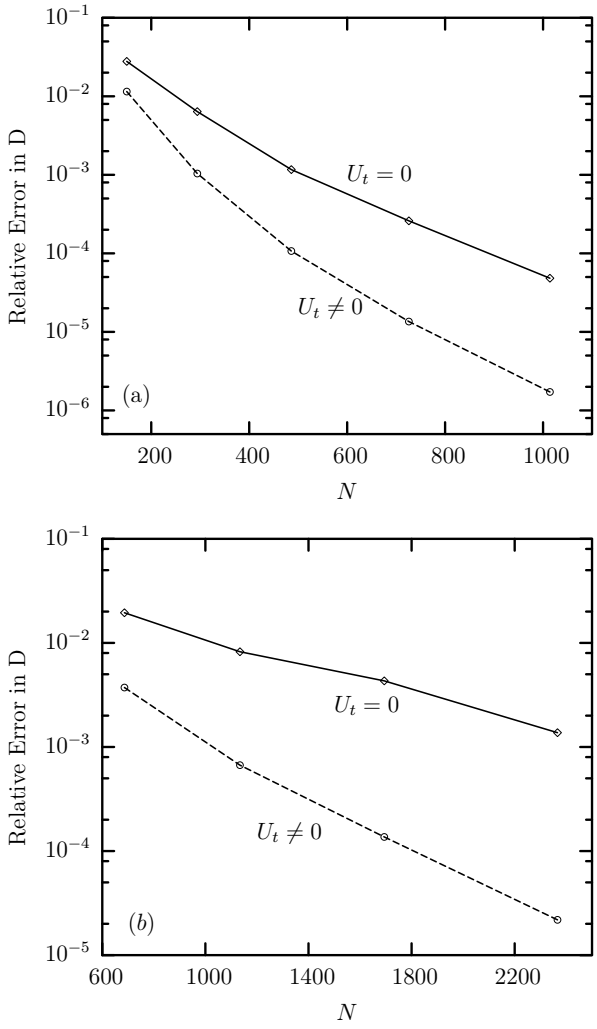

Figure 3.8: Relative error in the computed deformation D versus the number of spectral points N for a droplet with $\lambda = 0.5$ in a planar extensional flow. (a) Subcritical flow with $Ca = 0.13$ at time $t = 0.3$ when the droplet length has been increased by 24% while the width decreased by 18% ($D = 0.205$). $N_E = 6$ spectral elements are employed. (b) Supercritical flow with $Ca = 0.25$ at time $t = 1$ when the droplet length has been increased by 91% and the width decreased by 40% ($D = 0.523$). $N_E = 14$ spectral elements are employed. In both cases, the number of basis points N_B varies from 7 to 13 and the results for $N_B = 15$ were employed to determine the numerical error. The tangential velocity is employed with $c_t = 0.5$ in (a) and $c_t = 1.5D$ in (b).

Chapter 4

Flow in Vascular Vessels

Hemodynamic forces play an important role in the normal and pathological behavior of vascular endothelial cells via mechano-transduction. Hemodynamic forces exerted on leukocytes are also of great importance in the leukocyte adhesion process since they need to be balanced by the receptor-ligand binding forces on the surface of the cells [28, 40]. Fluid forces exerted on other protuberance in vascular vessels such as cancer cells and blood clots are also essential. A plethora of studies, mainly in the last two decades, has attributed the behavior, or changes in the behavior, of the endothelium as a result of one of the two components of the hemodynamic force, i.e., as effects of the shear stress. Thus, the second component of the hemodynamic force on the endothelium, i.e., the normal force or pressure, has been overlooked. In this study, we consider the relative importance of the shear and normal forces exerted on a biological cell (either an endothelial cell or a leukocyte) adherent to a wide range of blood vessels (from capillaries to large arteries) with various spreading angles of the cell. Based on the our results computed via the three-dimensional spectral boundary element method [21, 37], we show that the normal force contributes significantly to the total force on the biological cells and thus cannot be ignored. A scaling analysis is also employed to provide further physical insight.

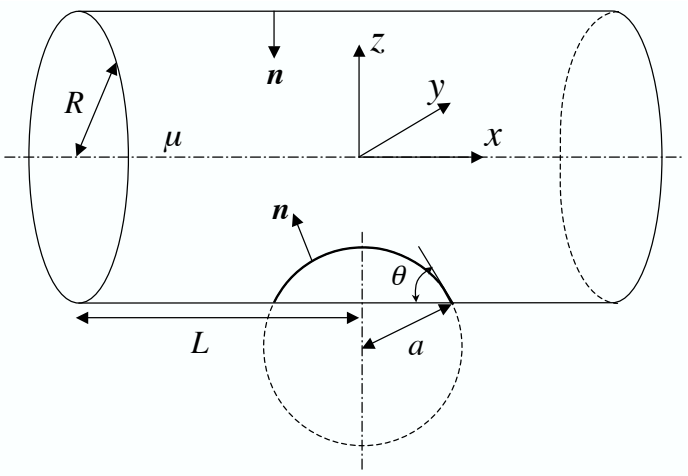

Figure 4.1: A cell attached to the inner surface of a blood vessel.

4.1 Assumptions and Problem Description

As illustrated in figure 4.1, the blood vessels are modeled as rigid cylindrical tubes with radius R and half length L. A solid spherical-like hump with radius a protruding from the tube wall represents the cell adhered to the blood vessel. The cell size is specified by its volume V or equivalently by the radius $\tilde{a}$ of a spherical cell with identical volume, i.e.,

$$\tilde{a} = \left(\frac{3V}{4\pi}\right)^{1/3} \tag{4.1}$$

The Stokes flow of a Newtonian fluid around the hump is assumed. The undisturbed flow far from the cell in the vessel is a Poiseuille flow $u^{\infty} = U\,(1-(y^2+z^2)/R^2, 0, 0)$ where U is the (maximum) velocity at the vessel centerline.

We investigate the shear stress and normal force over the cell and its vicinity as the spreading of the cell and its size (relative to the vessel radius) change. For small and moderate spreading angles, our modeling represents vascular endothelial cells

while large spreading angles better represent adherent leukocytes. In the former case, the hump represents the nucleus of the endothelial cell protruding above the rest of the cellular surface [34]. Since the cell size is a few microns, if we consider flow in capillaries (with a typical diameter of 8 μm) as well as in arterioles and venules (with a typical diameter of 10-140 μm) [3], the curvature of the vessel wall cannot be neglected, and thus a cylindrical tube is a proper geometry to represent the blood vessel. By considering a wide range of hump sizes, from very small values to $\tilde{a}/R \sim 1$, our results represent the entire range of blood vessels, i.e., from large arteries and veins down to small capillaries. In the case of adherent leukocytes, since the typical diameter of a leukocyte is 8 μm and we consider cylindrical vessels with radius comparable to or greater than the leukocyte size, our modeling applies to the case of adherent leukocytes in post-capillary or larger vessels.

In these systems, due to the small size of the cell (and possibly that of the vessel), the Reynolds number of the flow near the cell is very small and thus the assumption of Stokes flow is well justified [3, 59]. Based on the recent experimental findings [13], both endothelial cells and and leukocytes may spread into different configurations on a vessel; thus, our model is suitable to predict the hemodynamic force exerted on both endothelial cells and leukocytes. The assumption of the Newtonian surrounding fluid is well justified based on the results of Das, Johnson and Popel [16]. We emphasize that in the case of endothelial cells, the influence from neighboring cells is weak due to the fast decay of the perturbation force on the cell and the large separation distance between cells with respect to the cell size [34]; thus our investigation of a single endothelial cell is well justified. Similarly, in the case of

less spread cells, our investigation also represents multiple adherent cells assuming that these cells are not very close together. (Based on experimental findings, the inter-cell influence is negligible if the distance of adherent leukocytes is only a few times their sizes [10].) Therefore, in both physiological systems, i.e., endothelial cells and leukocytes adhering to blood vessels, our simplified model is able to capture the important physics of the complicated realistic problem.

For a given cell volume V and vessel radius R, the spreading of the cell on the vessel surface is controlled by the spreading angle θ defined in figure 4.1. Due to the vessel's cylindrical shape, the spreading angle θ along the contact line (i.e., the intersection of the cell surface with the vessel surface) is a function of the azimuthal angel ϕ as shown in figure 4.2. For a given size $\tilde{a}/R$ of a spherical-like cell, the relationship between the spreading angle θ and the azimuthal angle ϕ may be determined by the spreading angle θ_0 at $\phi = 0^\circ$. Hence, in this dissertation, the angle θ_0 is employed to define the spreading of the cell on the vessel surface. A wide range of spreading cells with $\theta_0 = 5^\circ$, 10°, 20°, ..., 160° (increments of 10°) is considered in this study. The small and moderate angles better represent vascular endothelial cells as shown in figure 4.3(a), while for large spreading angles, our modeling stands for adherent leukocytes as seen in figure 4.3(b).

Due to the small size of the cell, the flow near the cell occurs at low Reynolds numbers. The governing equations are the Stokes equation along with continuity. The associated boundary integral equation (2.3) is described in Chapter 2. For the current problem, the boundary is consisted of the solid surface S^w of the cell and the vessel, as well as the fluid boundary S^f of the vessel's inlet and outlet far from

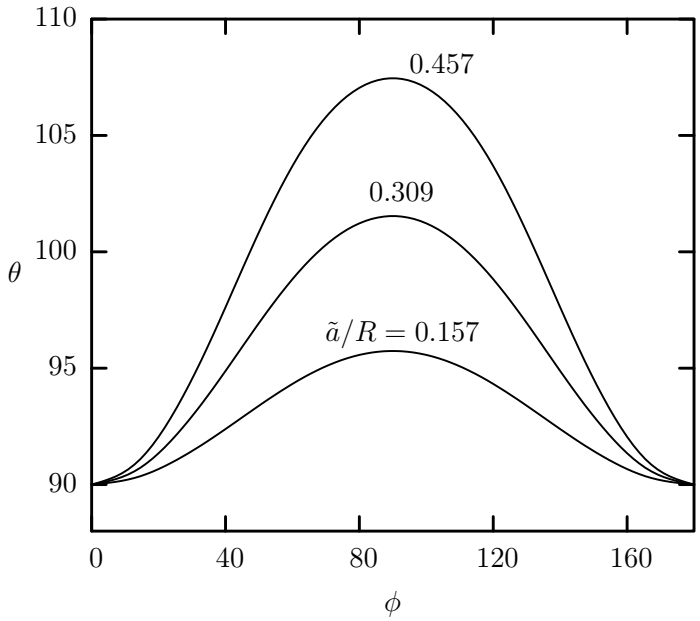

Figure 4.2: The variation of the spreading angle θ as a function of the azimuthal angle ϕ for $\theta_0 = 90^\circ$ and different cell sizes $\tilde{a}/R$. For this θ_0 the depicted values of $\tilde{a}/R$ correspond to $a/R = 0.2, 0.4, 0.6$.

the cell. The corresponding boundary conditions are

$$\boldsymbol{u} = 0 \quad \text{on the cell and vessel wall } S^w \tag{4.2}$$

$$\boldsymbol{u} = \boldsymbol{u}^\infty \text{ or } \boldsymbol{f} = \boldsymbol{f}^\infty \quad \text{on the fluid inlet and outlet } S^f \tag{4.3}$$

where $\boldsymbol{f}^\infty$ is the force associated with the undisturbed Poiseuille flow with velocity $\boldsymbol{u}^\infty$ far from the cell. The numerical solution of the boundary integral equation is achieved by employing the spectral boundary element method, which is described in depth in section 3.1.

The surface discretization of the current problem is illustrated in figure 4.3. The geometry for the biological cell and its immediate vicinity on the vessel is shown in figure 4.3(a) (for an endothelial cell) and figure 4.3(b) (for a leukocyte).

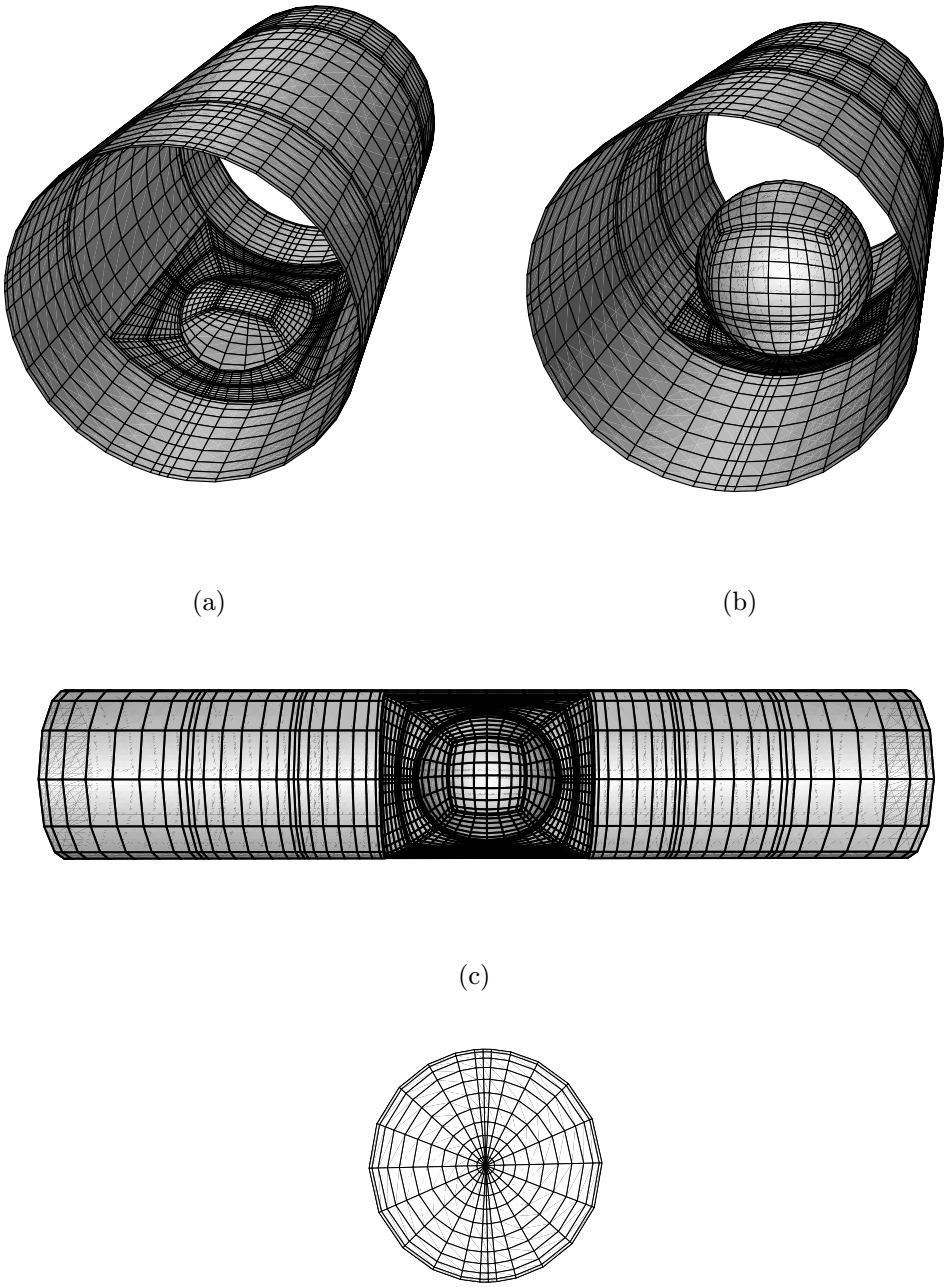

(a) (b)

(c)

(d)

Figure 4.3: Three-dimensional view of a cell adhering to the surface of a blood vessel and the discretization of the geometry: (a) an endothelial cell with $\theta_0 = 30^\circ$ and its vicinity on the vessel; (b) a leukocyte with $\theta_0 = 160^\circ$ and its vicinity on the vessel; (c) the bottom view of the entire geometry; (d) the fluid surface of the vessel's inlet and outlet.

Figure 4.3(c) demonstrates the entire discretization of the vessel. Figure 4.3(d) shows the discretization of the fluid boundary at the vessel's inlet and In this study the majority of computations are performed with a discretization employing $N_E = 39$ elements. The surface of the cell is divided into a total of 5 elements as shown in figure 4.3(a) for spreading angle $\theta_0 \leq 90°$, otherwise, 9 elements are employed as shown in figure 4.3(b). As shown later in section 4.3, the immediate vicinity of the cell on the vessel surface experiences a rapid change in the shear stress and the normal force. To achieve a sufficient accuracy in this area, two rows with eight elements each are employed as shown in figure 4.3(c). The vessel surface above the cell is usually discretized into either 2 or 4 spectral elements depending on the size of the cells and how close it is to the vessel wall above it. The rest cylindrical surface is divided into three rows with at least two elements each; the length of each row progressively increases with the distance from the cell surface as seen in figure 4.3(c). To determine the sufficient length of the tube (which formally should extend to infinity), we calculate the total force exerted on the cell with the half length L varying from 3 to 35 times the radius of the cylinder R. We find that with a half length of $L = 23R$ our computation is able to produce a relative error of $O(10^{-4})$ in the force. Additional tests concerning other physical properties have also been performed with similar results. The vessel's inlet and outlet are discretized into 2 elements each as shown in figure 4.3(d). This specific element distribution produces a sufficient accuracy even in the most challenging cases. Moreover, in most cases, a sufficient accuracy may be achieved even with a smaller number of spectral elements N_E.

The number of basis points N_B on each element is determined via several convergence tests for different cell sizes $\tilde{a}/R$ and spreading angles θ_0, by increasing the number of basis points N_B from 5 to 15. The results show an exponential convergence associated with the spectral discretization. For instance, figure 4.4 shows a typical exponential decay of the total force F_x (which is defined in the following section) with increasing number of basis points N_B. In this study, we have employed $N_B = 11$ or 13 basis points, which is sufficient to produce a negligible error for all cases. In addition, two levels of symmetry about the planes $y = 0$ and $x = 0$ are admitted in the study. Thus the memory requirement is reduced by a factor of 4^2; the computational time for the system matrices is reduced by a factor of 4 and the solution time for the linear systems by a factor of 4^3.

4.2 Definition of Physical Variables

The local shear stress magnitude τ and normal force f_n on the cell surface and its vicinity may be defined by

$$\tau = \sqrt{(f_x^L)^2 + (f_y^L)^2} \quad \text{and} \quad f_n = f_z^L \tag{4.4}$$

respectively. And the total force F_x on the cell is given by

$$F_x = \int_{S_c} f_x dS \tag{4.5}$$

where S_c is the cell's surface area. Due to the symmetry, total force components F_y and F_z are identically zero. In the above equations, $\boldsymbol{f}$ is the force vector defined at the global Cartesian coordinate system. Its corresponding vector defined at a

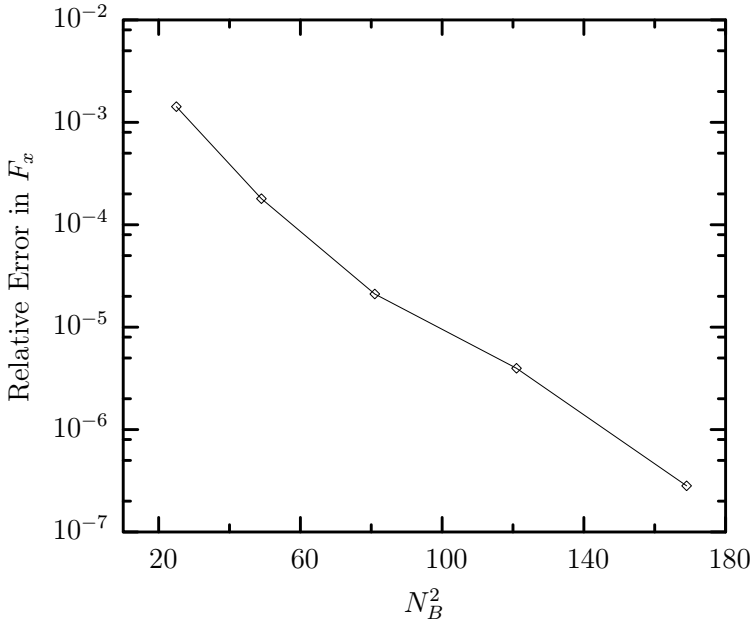

Figure 4.4: Relative error in the computed total force F_x on the cell for a typical problem with $\tilde{a}/R = 0.384$ (corresponding to $a/R = 0.5$) and $\theta_0 = 90^\circ$, as the number of basis points N_B increases form 5 to 13. The results for $N_B = 15$ is employed for the error determination. This figure is generated by applying $N_E = 39$ spectral elements; the resulting exponential convergence is mainly associated with the spectral discretization on the cell and thus it can also be achieved with a smaller number of spectral elements on the vessel wall.

local Cartesian coordinate system (x^L, y^L, z^L) is denoted as $\boldsymbol{f}^L = (f_x^L, f_y^L, f_z^L)$. (The local coordinate system has the x^L- and y^L-axes in the tangent plane and the z^L-axis parallel to the vector $\boldsymbol{n}$ normal to the surface.)

The vessel radius R is employed as the length scale and the maximum undisturbed velocity U as the velocity scale. We employ the shear stress on the vessel wall far from the cell, $\tau_{wall}^{\infty} = 2\mu U/R$, as the scale for the shear stress τ and normal force f_n. On the other hand, for shear stress on the cell and its vicinity, the ratio $\tau/\tau_{wall}^{\infty}$ demonstrates the amplification in the shear stress induced by the presence of the cell. From equation 4.5, $F_x \sim R^2\boldsymbol{f} \sim R^2\tau_{wall}^{\infty}$ and thus in this study we select $R^2\tau_{wall}^{\infty}$ as the scale for the total force.

For a fixed flow rate $Q = \pi R^2 U/2$, the problem of determining the force field on the cell and its vicinity is determined by two independent geometric parameters: the relative cell size with respect to the vessel radius, $\tilde{a}/R$, and the spreading angle θ_0. As shown in figure 4.2, for a given vessel radius R and spreading angle θ_0, by increasing the cell size $\tilde{a}$, the surface area, the height and the frontal area of the cell increase all together, which results in a larger blocking in the flow. An equivalent physical problem could be the decrease of the vessel radius R for a constant cell volume $\tilde{a}$ and cell spreading angle θ_0. Therefore, our results provide insight on the blocking of the endothelial cells or leukocytes as vessel size varies. On the other hand, for a constant cell volume $\tilde{a}$ and vessel radius R, by increasing the spreading angle θ_0, the cell's height and the blocking to the flow also increases as shown in figure 4.2. Therefore, by increasing $\tilde{a}/R$ or θ_0, an increase in the force on the cell is expected due to the higher blocking. A discussion on the total force as well as the

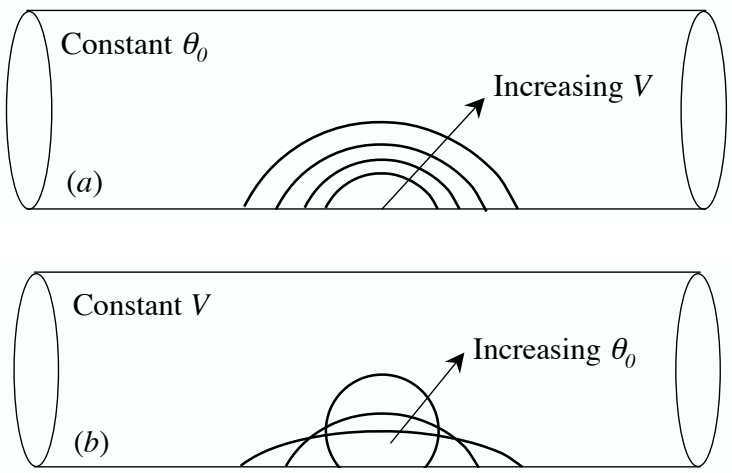

Figure 4.5: Illustration of the variation of the two independent geometric parameters of the current problem: (a) the increase in the cell volume V (or length $\tilde{a}$) for a given vessel radius R while the spreading angle θ_0 remains constant; (b) the increase in the angle θ_0 with constant cell volume and vessel radius.

local stress distribution on the cell and its vicinity will be provided quantitatively in section 4.3.

4.3 Results, Analysis and Discussion

Figure 4.6 shows the shear stress $\boldsymbol{\tau} = (f_x^L, f_y^L, 0)$ over the cell and its vicinity on the vessel for a cell with a radius half the vessels radius (or $\tilde{a}/R = 0.384$) and spreading angle $\theta_0 = 90°$. This figure is a three-dimensional quiver plot where the arrows start from the geometry surface and their length is proportional to the magnitude of the shear stress vectors. As shown in the figure, the shear stress increases with the height along the cell surface and reaches the maximum at the cell peak due to symmetry.

It is also prominent according to the figure that the shear stress diminishes at the lower part of the cell and its nearby area on the vessel.

Figure 4.7 shows the magnitude of the shear stress $\tau = \sqrt{(f_x^L)^2 + (f_y^L)^2}$ as a function of the arc length s_{xz} (measured from the cell peak) along the cross-section of the geometry surface with the plane $y = 0$ for a spreading angle $\theta_0 = 90^\circ$ with different cell sizes $\tilde{a}/R$. This figure clearly shows that the shear stress distribution has been greatly influenced by the presence of the cell due to the associated flow blocking. Figure 4.7 agrees with the previous quiver plot in a quantitative way. The shear stress on the upper part of the cell surface is much larger than that on the vessel far from the cell, τ_{wall}^{∞}, with a maximum at the cell peak due to symmetry. On the other hand, the shear stress diminishes on the lower part of the cell and its neighbor area on the vessel wall and even approaches zero near the contact line. This behavior is similar to those found in the case of two- or three-dimensional protuberances on solid planes [28, 38, 61, 62]. This figure also demonstrates the influence of the cell size $\tilde{a}/R$ on the shear stress distribution. In particular, by increasing the cell size from small values, the maximum shear stress magnitude τ (the shear stress on the cell peak) decreases until $\tilde{a}/R \approx 0.384$. Further increase in the cell size results, otherwise, in an increase in the shear stress. The same behavior is also shown in figure 4.8 where the variation of the shear stress magnitude is plotted along the cross-section of the geometry surface with the plane $x = 0$.

The influence of the spreading angle θ_0 on the shear stress distribution is shown in figure 4.9, where a typical cell size $\tilde{a}/R = 0.30$ is given to plot shear stress magnitude τ versus the arc length along the cross-section of the geometry surface

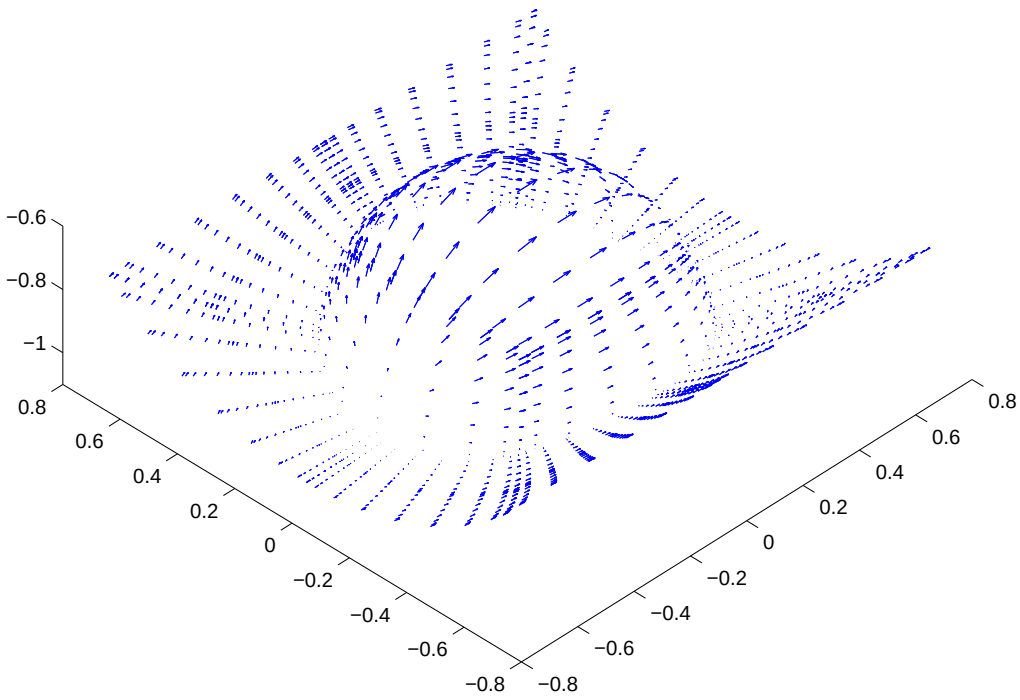

Figure 4.6: A three-dimensional quiver plot for the shear stress vector $\boldsymbol{\tau} = (f_x^L, f_y^L, 0)$ for a cell with $\theta_0 = 90^\circ$ and $\tilde{a}/R = 0.384$ (which corresponds to $a/R = 0.5$).

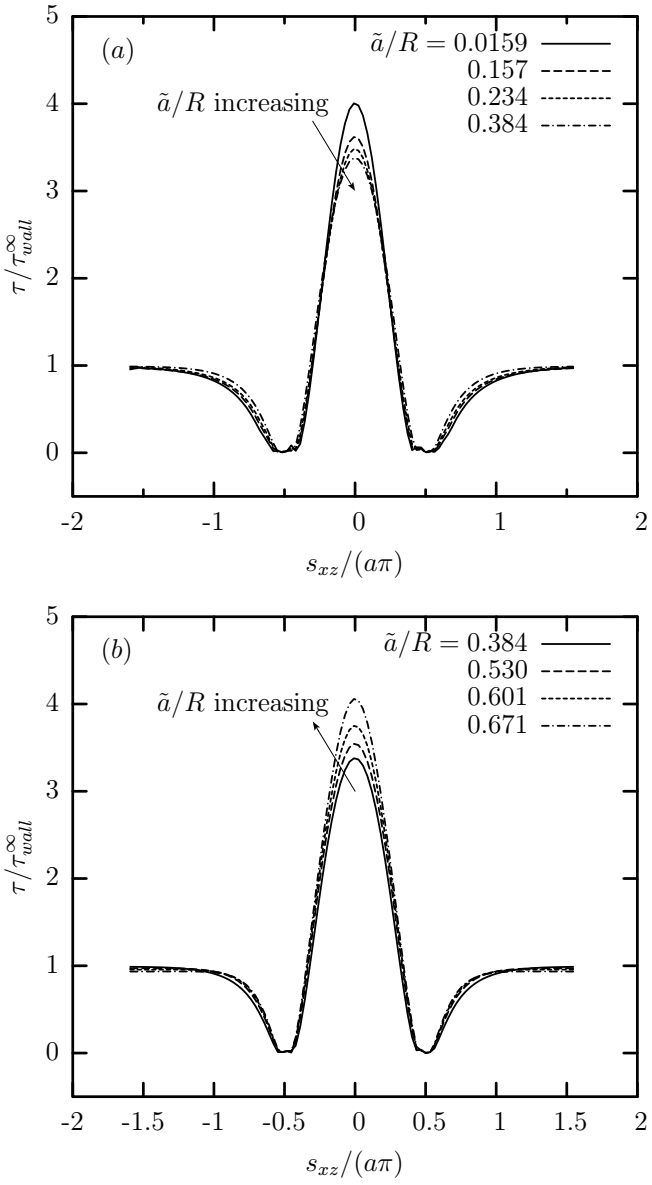

Figure 4.7: Influence of the cell size $\tilde{a}/R$ on the shear stress. (a) Variation of the shear stress magnitude τ as a function of the arc length s_{xz} (the measurement starts from the cell peak) along the cross-section of the geometry surface with the plane $y = 0$ for the spreading angle $\theta_0 = 90°$. The depicted values of $\tilde{a}/R$ correspond to $a/R = 0.02, 0.2, 0.3, 0.5$. (b) As in (a) but for values of $\tilde{a}/R$ corresponding to $a/R = 0.5, 0.7, 0.8, 0.9$.

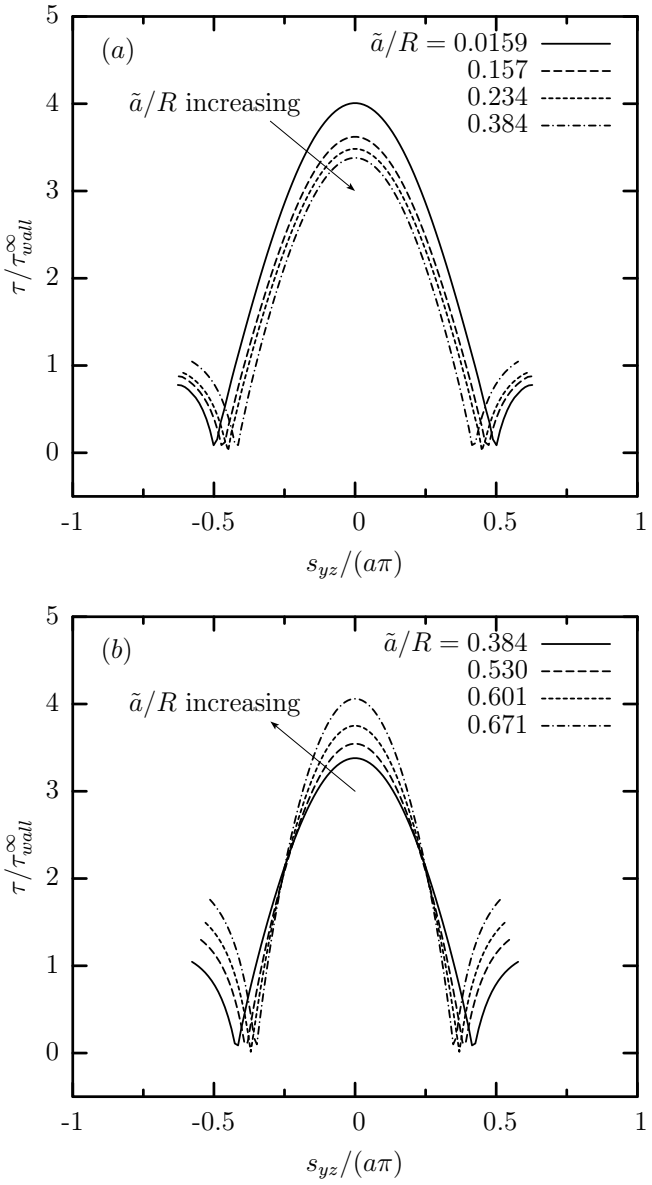

Figure 4.8: Influence of the cell size $\tilde{a}/R$ on the shear stress. (a) Variation of the shear stress magnitude τ as a function of the arc length s_{yz} (the measurement starts from the cell peak) along the cross-section of the geometry surface with the plane $x = 0$ for the spreading angle $\theta_0 = 90°$. The depicted values of $\tilde{a}/R$ correspond to $a/R = 0.02, 0.2, 0.3, 0.5$. (b) As in (a) but for values of $\tilde{a}/R$ corresponding to $a/R = 0.5, 0.7, 0.8, 0.9$.

with the planes $y = 0$ and $x = 0$. This figure reveals that on the upper part of the cell, the shear stress magnitude τ demonstrates a monotonic increase with the spreading angle. This is expected by the simple analysis discussed in the previous section. The increasing spreading angle causes the increase of the height and the frontal area of the cell, and thus a higher blocking to the vessel flow is formed.

A comprehensive plot is shown in figure 4.10 demonstrating the influence of both the cell size $\tilde{a}/R$ and spreading angle θ_0 on the maximum shear stress magnitude τ^{max}. For small angles, the maximum shear stress is independent of the cell size $\tilde{a}/R$ as the curves for $\theta_0 = 5^\circ - 40^\circ$ reveal, while for large angles, the shear stress magnitude τ^{max} at the cell peak shows a minimum at a moderate cell size $\tilde{a}/R = 0.384$: a weak increase in τ^{max} when the cell size decreases from 0.384 and a large increase in τ^{max} when the cell size increases from 0.385 are demonstrated. The strong dependence of τ^{max} on the cell size $\tilde{a}/R$ is much more pronounced at large angles as the curves for $\theta_0 = 100^\circ - 160^\circ$ reveal. In addition, for a given cell size $\tilde{a}/R$, τ^{max} increases monotonically with the spreading angle θ_0; the increase is much more pronounced at large cell sizes.

Figure 4.11 shows a three-dimensional quiver plot of the normal force vector $\boldsymbol{f}_n = (0, 0, f_z^L)$ for a cell with $\tilde{a}/R = 0.384$ and $\theta_0 = 90^\circ$. At the upstream, the normal force points towards the solid or the cell surface, i.e., in the opposite direction with respect to the normal vector $\boldsymbol{n}$, while the normal force points into the flow at the downstream. In addition, the normal force appears stronger near the intersection of the cell with the vessel while it decreases as it move towards the top of the cell.

The normal force distribution on the cell and its vicinity is shown in figure 4.12

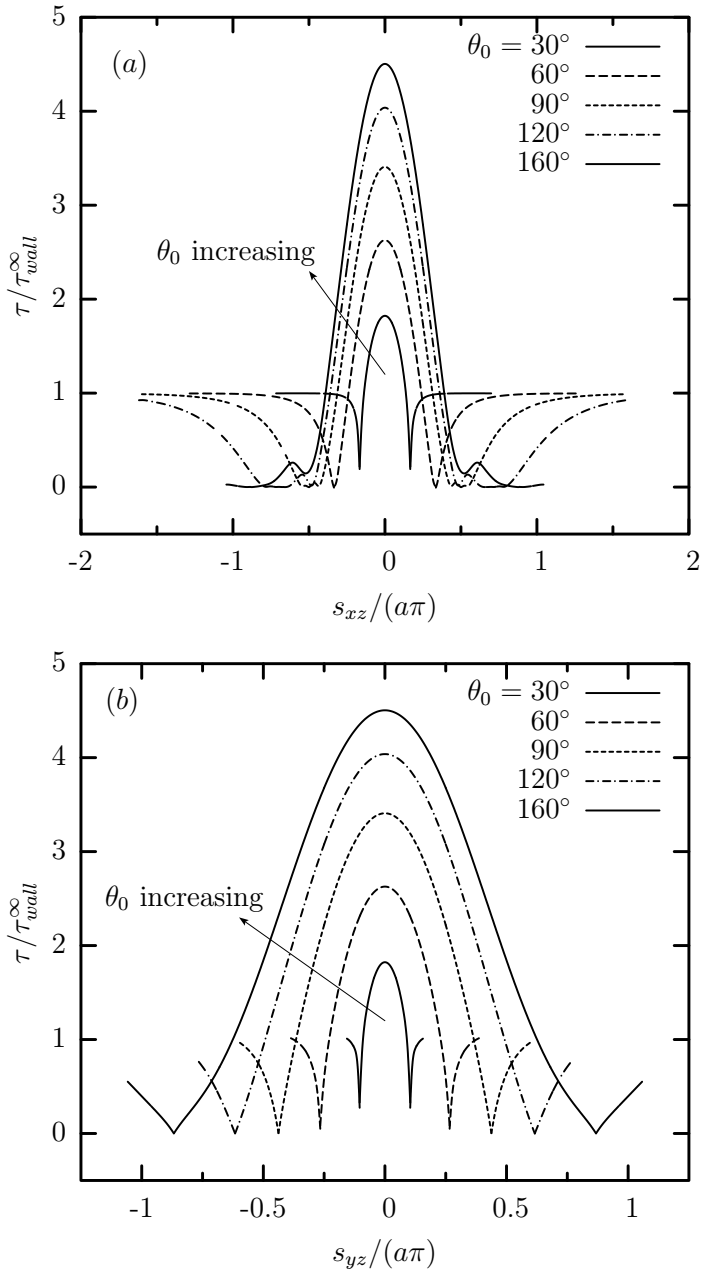

Figure 4.9: Influence of the spreading angle θ_0 on the shear stress. (a) Variation of the shear stress magnitude τ as a function of the arc length s_{xz} (the measurement starts from the cell peak) along the cross-section of the geometry surface with the plane $y = 0$ for a cell with $\tilde{a}/R = 0.30$ and for $\theta_0 = 30°, 60°, 90°, 120°$. (b) As in (a) but for the plane $x = 0$.

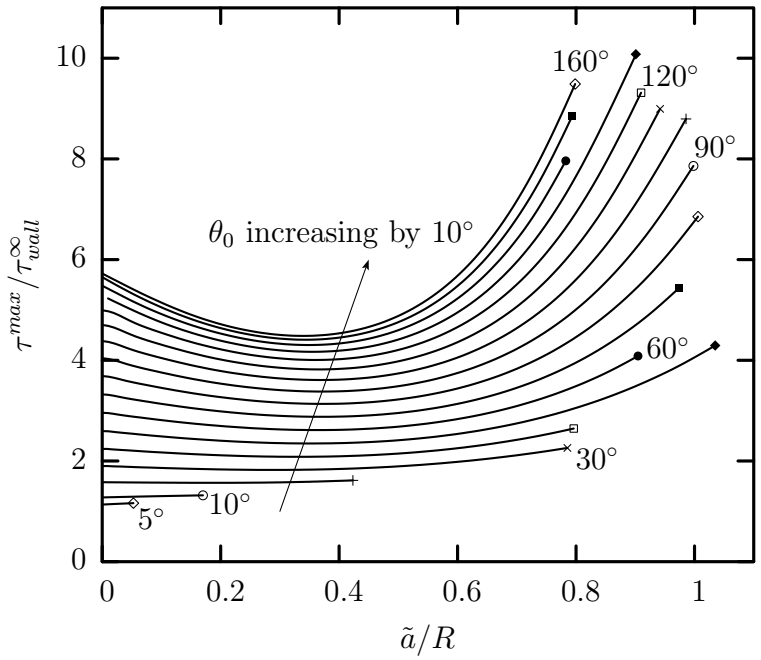

Figure 4.10: Maximum magnitude of the shear stress τ^{max} versus the cell size $\tilde{a}/R$. The spreading angle θ_0 varies from 5° to 160°.

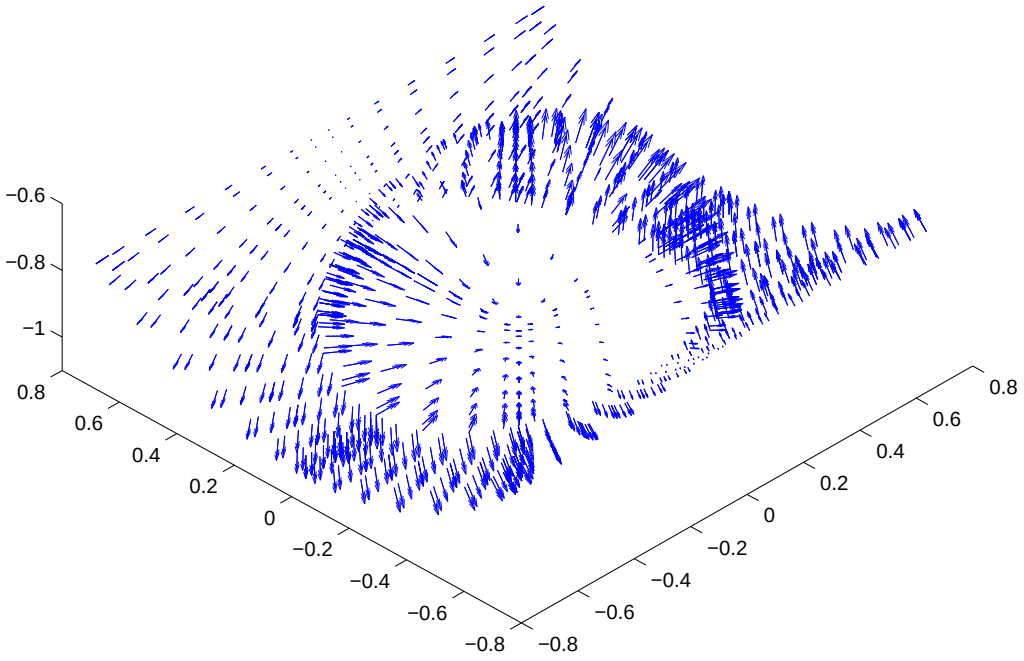

Figure 4.11: A three-dimensional quiver plot of the normal force $\boldsymbol{f}_n = (0, 0, f_z^L)$ for a cell with $\theta_0 = 90^\circ$ and $\tilde{a}/R = 0.384$ (which corresponds to $a/R = 0.5$). The arrows start from the geometry surface while their length is proportional to the magnitude of the normal force.

where the normal force magnitude f_n is plotted along the cross-section of the geometry surface with the plane $y = 0$ for a cell with spreading angle $\theta_0 = 90^\circ$ and various sizes $\tilde{a}/R$. The existence of the cell results in a significant modification of the normal force over the cell and its vicinity on the vessel. By increasing the cell size, the upstream and downstream normal force increases monotonically in distinct contrast to the behavior of the shear stress shown earlier in figure 4.7. We notice that the undisturbed normal force (far from the cell on the vessel) shows a linear variation with the position s_{xz}, which preserves the normal force behavior on the vessel with the absence of the cell.

Figure 4.13 shows the influence of the spreading angle θ_0 on the normal force for a typical cell volume, $\tilde{a}/R = 0.30$. By increasing the spreading angle θ_0 for a given cell size, the upstream and downstream change in the normal force increases monotonically due to the corresponding increase in the flow blocking.

Besides the local shear stress and normal force on the cell and its vicinity, the total hemodynamic forces exerted on the adhered leukocyte is essential in measuring the balancing biological forces, e.g. receptor-ligand binding forces. Figure 4.14 demonstrates that the total force F_x exerted on the cell along the flow direction increases with the cell size $\tilde{a}/R$ for any spreading angle. The increase is much more pronounced at large sizes and spreading angles, especially for $\theta_0 \geq 90^\circ$, due to the higher blocking to the vessel flow. For small cell sizes, by increasing the spreading angle from small values, the total force F_x decreases up to $\theta_0 \approx 50^\circ$ as shown in the figure's inset; for higher values (i.e., $\theta_0 > 50^\circ$) the total force increases with the spreading angle.

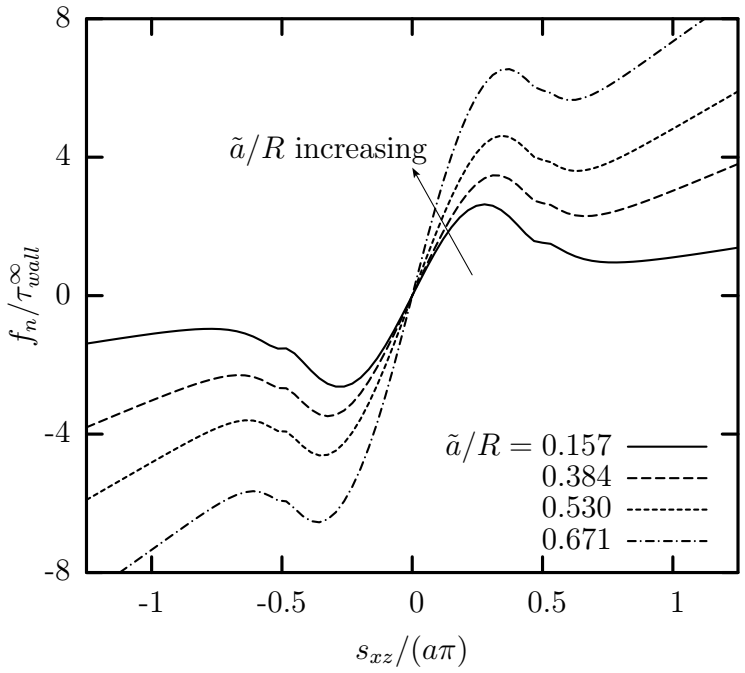

Figure 4.12: Influence of the cell size $\tilde{a}/R$ on the normal force: variation of the normal force f_n as a function of the arc length s_{xz} (the measurement starts from the cell peak) along the cross-section of the geometry surface with the plane $y = 0$ for the spreading angle $\theta_0 = 90°$. The depicted values of $\tilde{a}/R$ correspond to $a/R = 0.2, 0.5, 0.7, 0.9$. Note that the normal force is the opposite of the pressure, i.e., $p = -f_n$ while the reference pressure $p_0 = 0$ is taken at the peak of the cell.

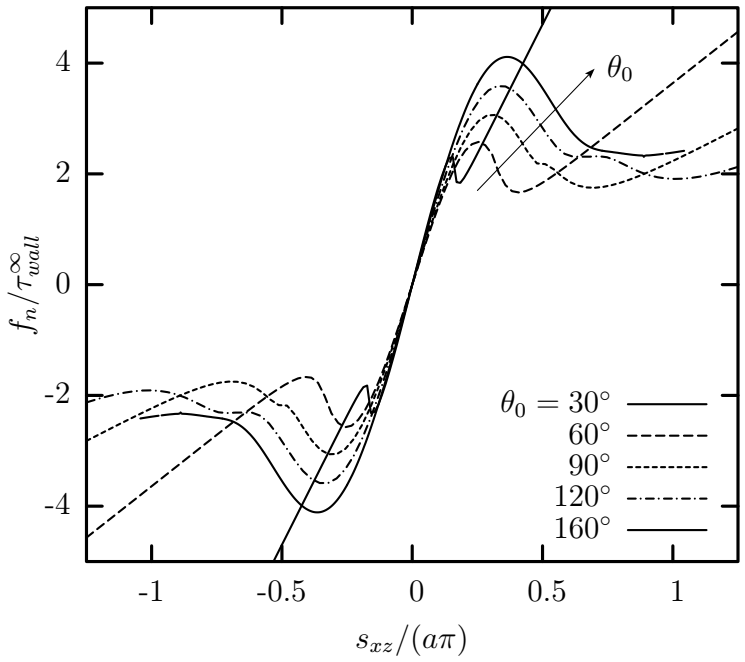

Figure 4.13: Influence of the spreading angle θ_0 on the normal force: variation of the normal force f_n as a function of the arc length s_{xz} (the measurement starts from the cell peak) along the cross-section of the geometry surface with the plane $y = 0$ for a cell with $\tilde{a}/R = 0.30$ and for $\theta_0 = 30°, 60°, 90°, 120°, 160°$.

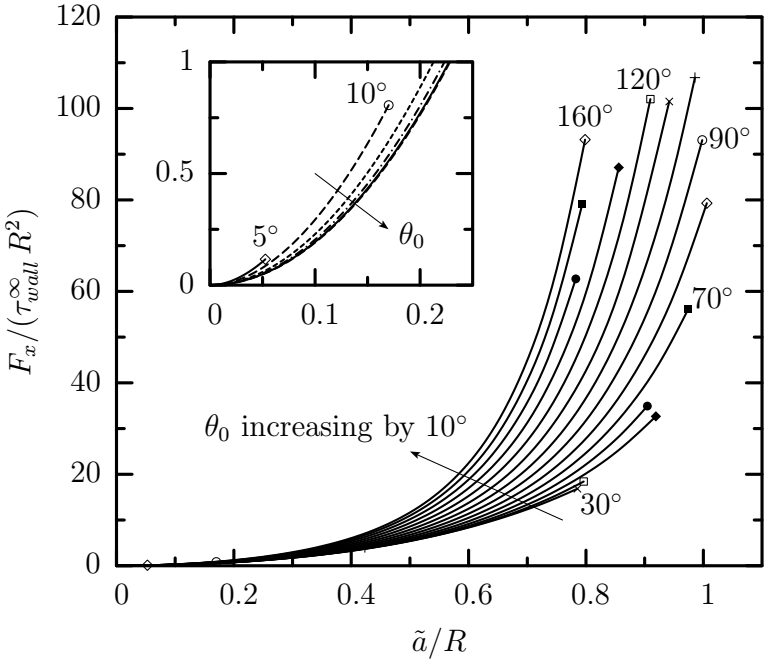

Figure 4.14: The total force F_x exerted on the cell as a function of the cell size $\tilde{a}/R$ for spreading angles $\theta_0 = 5°, 10°, 20°, ..., 160°$ (increments of 10°). The inset shows the same variation for small and moderate angles $\theta_0 = 5°, 10°, 20°, ..., 50°$. Note that τ^{∞}_{wall} is the undisturbed shear stress on the vessel wall far from the cell.

In order to further investigate the nature of the force exerted on the cell, we divide the hemodynamic force on the cell into its two components, i.e., the shear force F_x^{shear} and the normal force F_x^n. The relative magnitude of the two force components is shown in figure 4.15. For large vessels (i.e., small $\tilde{a}/R$), the shear force F_x^{shear} dominates the total force but the contribution of the normal force cannot be neglected especially at large spreading angles. For an instance, even for $\tilde{a}/R \to 0$ the normal force on an endothelial cell with $\theta_0 = 60^\circ$ is 30% of the shear force; while for an adhered leukocyte with $\theta_0 = 160^\circ$, the normal force is nearly 57% of the shear force. As the vessel radius decreases (i.e., $\tilde{a}/R$ increases), the normal force increases its contribution to the total hemodynamic force and it becomes dominant at large cell sizes. For example, for a cell with spreading angle $\theta_0 = 120^\circ$ and size $\tilde{a}/R = 0.9$, the normal force F_x^n is 4.6 times greater than the shear force F_x^{shear}. We also observe that the increase of the relative contribution of the normal force with the cell size is much faster for large spreading angles.

In order to further explain the behavior of the hemodynamic forces, we then proceed to conduct a scaling analysis for the shear and normal force acting on the cells. For very small cell sizes and spreading angles, the analysis predicts that the shear force F_x^{shear} on the cell is proportional to the cell surface area S_c and the shear stress on the cell τ_c. The cell surface area S_c is then related to the cell size $\tilde{a}$ and the spreading angle θ_0, while τ_c is proportional to the shear stress far from the cell τ_{wall}^{∞}. The above relations can be given by

$$S_c \sim \tilde{a}^2 \, \theta_0^{-2/3} \tag{4.6}$$

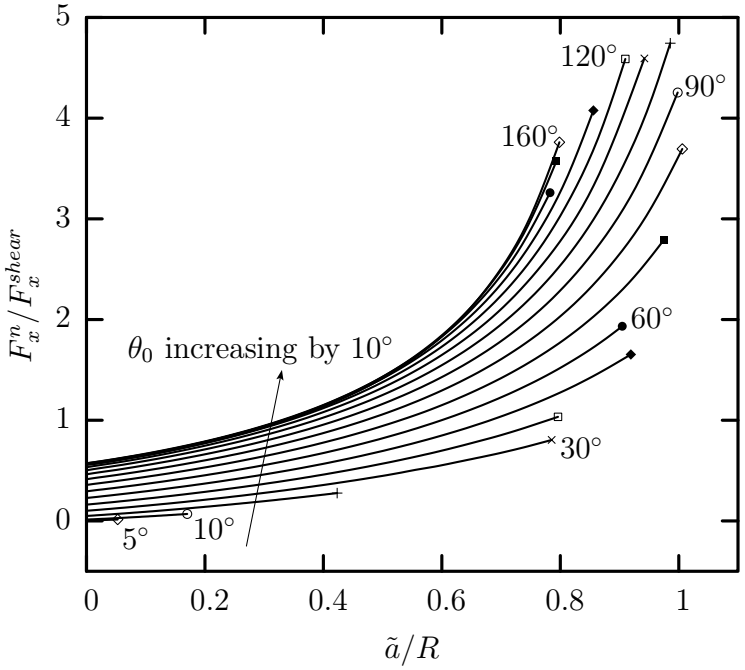

Figure 4.15: Relative magnitude of the normal force F_x^n with respect to the shear force F_x^{shear} exerted on the cell as a function of the cell size $\tilde{a}/R$. The spreading angle θ_0 varies form 5° to 160°.

$$\tau_c \sim \tau_{wall}^{\infty} \tag{4.7}$$

$$F_x^{shear} \sim \tau_c S_c \sim \tau_{wall}^{\infty}\, \tilde{a}^2\, \theta_0^{-2/3} \tag{4.8}$$

Figure 4.16 shows the numerically calculated surface area S_c as a function of the cell size $\tilde{a}/R$ for a variety of spreading angles. This figure demonstrates that equation (4.6) predicts qualitatively the correct dependence of S_c on $\tilde{a}/R$ for all cases. In addition, it predicts the correct qualitative dependence of S_c on θ_0 for angles $\theta_0 \leq 80^\circ$ and for small and moderate cell sizes as shown in the figure's inset. The behavior of S_c is not predicted by the scaling analysis for larger angels and larger cells.

Figure 4.17 shows the dependence of the shear stress $\tau_c \equiv F_x^{shear}/S_c$ over the cell on the problem parameters. For small and moderate cell sizes, τ_c is practically independent of the cell size for all angles, which is in qualitative agreement with the predictions of the scaling analysis. The figure also shows that the scaling analysis fails to predict the increase of τ_c with the spreading angle θ_0; however this increase is rather small even for the entire range of angles studied $5^\circ \leq \theta_0 \leq 160^\circ$. We also note that the dependence of τ_c on the problem parameters is very similar to that of the maximum shear stress magnitude τ^{max} on the cell presented earlier in figure 4.10.

Figure 4.16 and 4.17 show that both surface area S_c and shear stress τ_c increase with the cell size. We note the surface area S_c increases much faster than the shear stress τ_c and thus it contributes more to the shear force F_x^{shear} exerted on the cell. As shown in figure 4.18, the shear force F_x^{shear} increases with the cell size $\tilde{a}/R$, but decreases as the spreading angle θ_0 increases when $\theta_0 \leq 70^\circ$. The dependence of

F_x^{shear} on the problem parameters is very similar to that of the cell surface area S_c. Therefore, the predictions of the scaling analysis for the shear force on the cell is qualitatively valid for the whole range of the parameter space.

The scaling analysis predicts that the normal force F_x^n on the cell may be divided into two distinct components, F_x^{n1} and F_x^{n0}. The first component F_x^{n1} represents the undisturbed pressure gradient acting on the cell and is scaled as

$$F_x^{n1} \sim \Delta p^1 \, A_f \sim \tau_{wall}^{\infty} \, \frac{\tilde{a}^3}{R} \tag{4.9}$$

where Δp^1 and A_f are the corresponding pressure change over the cell and the frontal area of the cell respectively. Both of them may be scaled with the undisturbed shear stress on the vessel wall and the cell size,

$$\Delta p^1 \sim \tau_{wall}^{\infty} (\tilde{a}/R) \, \theta_0^{-1/3} \tag{4.10}$$

$$A_f \sim \tilde{a}^2 \, \theta_0^{1/3} \tag{4.11}$$

The analysis shows that for small cells and small spreading angles the first normal force component F_x^{n1} is independent of the spreading angle.

The other component of the normal force, F_x^{n0}, arises from the disturbance of the base flow owing to the presence of the cell. The pressure change Δp^0 scales as $\tau_{wall}^{\infty}\theta_0$ and thus the associated normal force scales as

$$F_x^{n0} \sim \Delta p^0 \, A_f \sim \tau_{wall}^{\infty} \, \tilde{a}^2 \, \theta_0^{4/3} \tag{4.12}$$

Based on the analysis, we conclude that the pressure gradient normal force component F_x^{n1} is negligible at small cell sizes due to its $\tilde{a}/R$ dependence but becomes

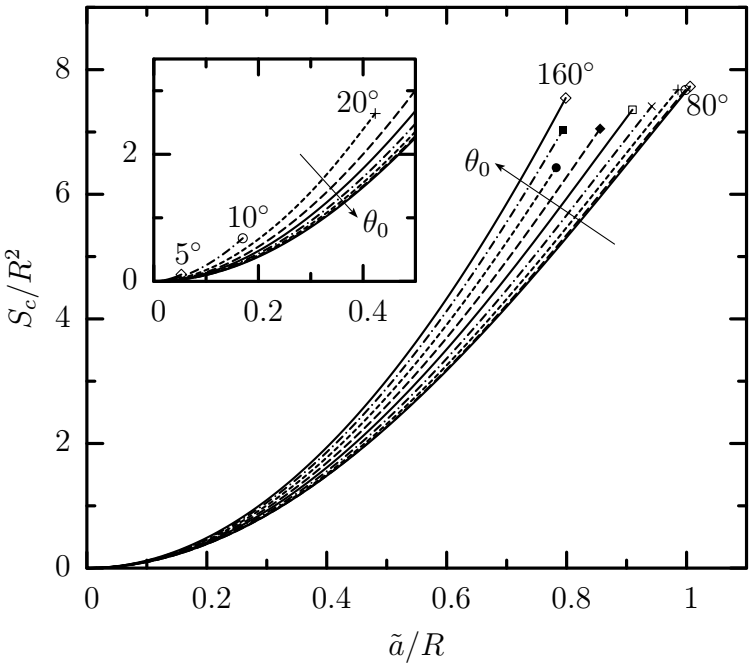

Figure 4.16: The surface area S_c of the cell as a function of the cell size $\tilde{a}/R$. The spreading angle θ_0 varies from 80° to 160° in increments of 10°. The inset shows the same variation for small and moderate angles $5°, 10°, 20°, ..., 80°$.

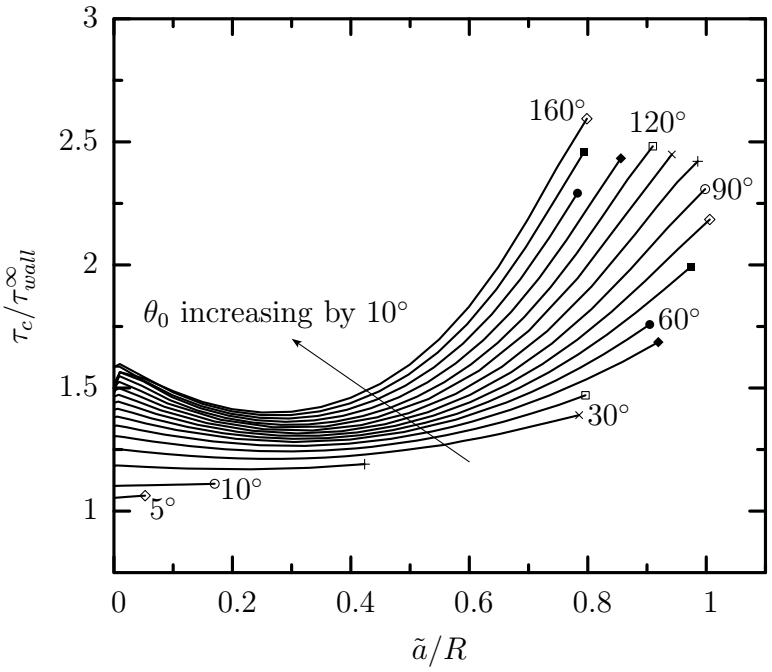

Figure 4.17: The shear stress on the cell $\tau_c \equiv F_x^{shear}/S_c$ as a function of the cell size $\tilde{a}/R$. The spreading angle θ_0 varies from 5° to 160°.

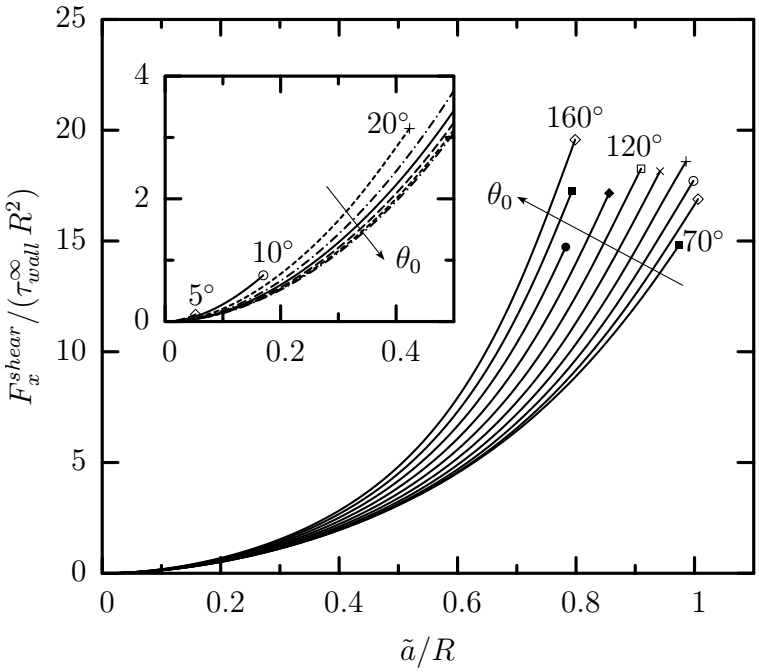

Figure 4.18: The shear force F_x^{shear} exerted on the cell as a function of the cell size $\tilde{a}/R$. The spreading angle θ_0 varies from 70° to 160° in increments of 10°. The inset shows the same variation for small and moderate angles $5°, 10°, 20°, ..., 70°$.

dominant as the cell size increases. On the other hand, the base normal force component F_x^{n0} is negligible compared to F_x^{n1} at moderate and large cell sizes.

The scaling analysis predicts the frontal area of the cell to increase with both the cell size and the spreading angle. As shown in figure 4.19 where we plot the frontal area of the cell A_f as a function of the cell size and the spreading angle based on the numerical computation, the scaling analysis predicts qualitatively the correct behavior of A_f. Figure 4.20 demonstrates the pressure change $\Delta p \equiv F_x^n / A_f$ over the cell as a function of the cell size and the spreading angle. We note that Δp increases with both parameters; the increase is more dramatic at large cell sizes and spreading angles due to the associated pressure gradient increase resulting from the higher flow blocking. For small cell sizes, where the normal force is dominated by its bas component F_x^{n0}, the scaling analysis predicts the pressure to increase with the spreading angle, and to be independent of the cell size. Therefore, the scaling analysis fails to predict the pressure behavior at small cell sizes. However, its prediction of the dependence on θ_0 is in qualitative agreement with the numerical results. We emphasize the fact that Δp does not go to zero as $\tilde{a}/R \to 0$ for finite spreading angles as shown in the figure's inset, is in agreement with the predictions of the scaling analysis.

From the the scaling analysis and our numerical results for the cell's frontal area A_f and the pressure change Δp, it is now clear that the normal force $F_x^n \sim \Delta p A_f$ increases monotonically with both the cell size and the spreading angle; the increase is much more pronounced at large cell sizes and high spreading angles as shown in figure 4.21.

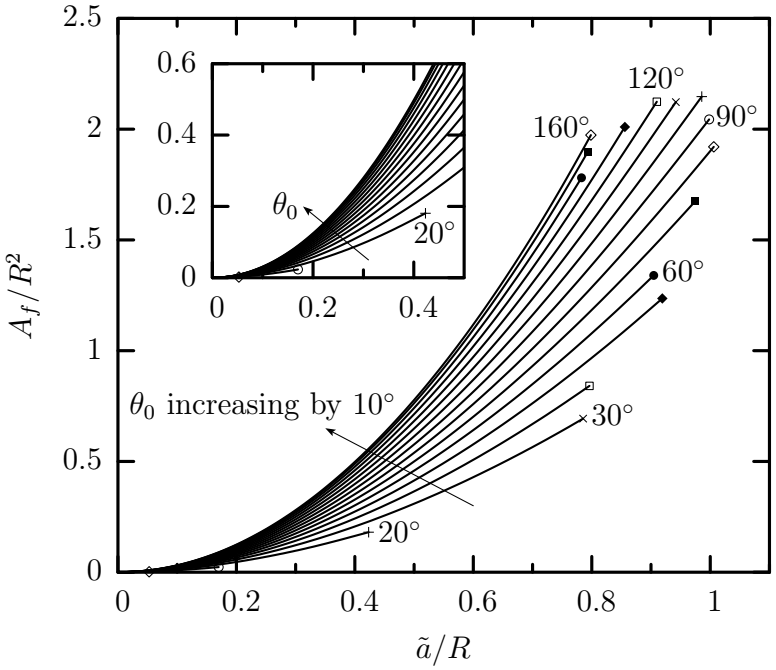

Figure 4.19: The frontal area of the cell A_f as a function of the cell size $\tilde{a}/R$. The spreading angle θ_0 varies from 5° to 160°. The inset shows the same variation for small cell sizes $\tilde{a}/R$.

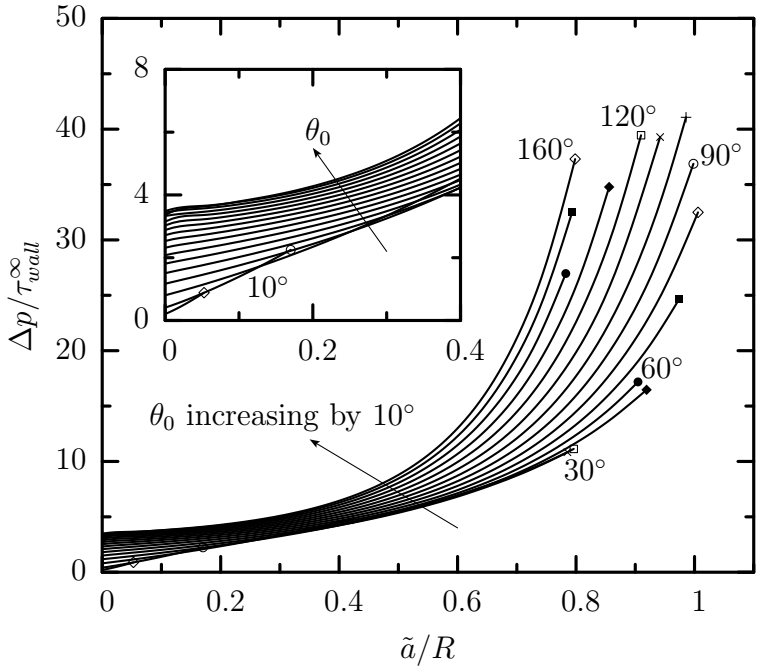

Figure 4.20: The pressure change $\Delta p \equiv F_x^n/A_f$ as a function of the cell size $\tilde{a}/R$. The spreading angle θ_0 varies from 5° to 160°. The inset shows the same variation for small cell sizes $\tilde{a}/R$.

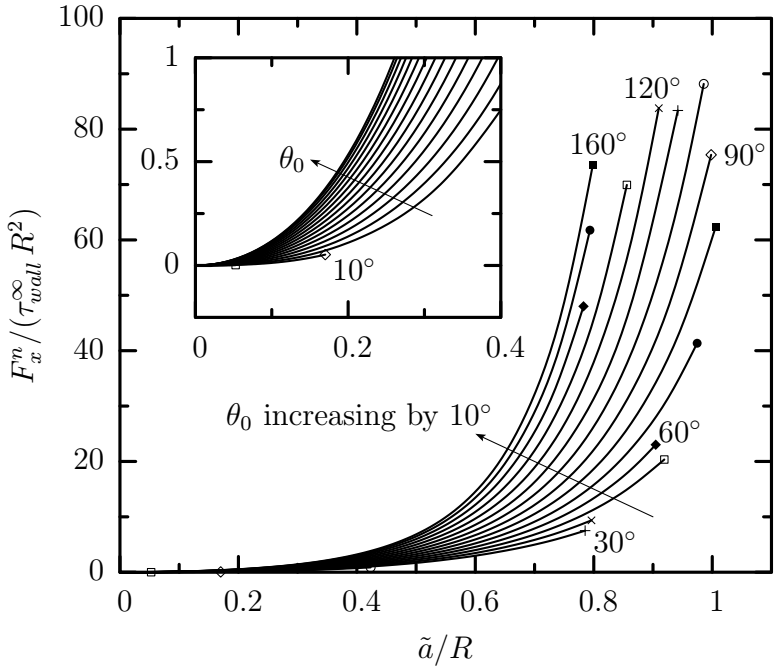

Figure 4.21: The normal force F_x^n exerted on the cell as a function of the cell size $\tilde{a}/R$. The spreading angle θ_0 varies from 5° to 160°. The inset shows the same variation for small cell sizes $\tilde{a}/R$.

Chapter 5

Buoyancy-Driven Motion of a Droplet Along a Solid Wall

In this chapter, we consider the inertialess motion of a buoyant droplet left to rise (or sediment) in an otherwise quiescent fluid near a vertical solid wall. The three-dimensional spectral boundary element method [21, 37] has been employed in our computations. We focus our interest in understanding the transient behavior of the droplets, e.g. the rising speed, lateral migration, and the interfacial shape under the influence of the Bond number. Comparison has been made to previous analytical predictions.

5.1 Problem Description

Figure 5.1 illustrates the motion of a droplet of volume V (fluid 1) with density ρ_1 and viscosity $\lambda\mu$ in an otherwise quiescent viscous fluid (fluid 2) with density ρ_2 and viscosity μ near a stationary vertical solid wall. The gravitational acceleration is g while the surface tension γ is assumed constant. The droplet volume centroid is denoted as $\boldsymbol{x}_c$ and z_{c0} is the initial distance from the wall where the spherical drop is released. The droplet velocity is composed of a rising velocity U_x parallel

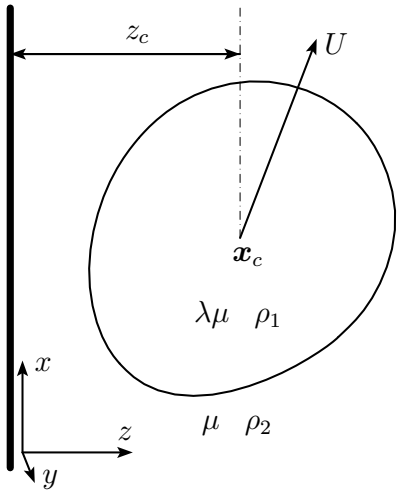

Figure 5.1: Illustration of a droplet moving along a solid wall.

to the wall and a migration velocity U_z perpendicular to the wall, which is incurred either by the droplet deformation or by the inertia. The velocity component in the third direction is zero due to symmetry. For rigid particles, the lateral motion is influenced by the inertia only, while for a deformed droplet, the asymmetry of the flow causes the droplet to migrate laterally. When the particle Reynolds number is approaching zero, the inertia influence may be neglected. The deformation of the droplet breaks the symmetry of the flow and disturbs the balance of the viscous forces exerted all over the droplet, and thus becomes the major cause for the lateral migration.

In the current problem, the characteristic length a of the droplet (defined by $a = (3V/4\pi)^{1/3}$) is employed as the length scale while the time is scaled with the buoyancy time scale $\tau_g = \mu/\Delta\rho g a$ (where $\Delta\rho = |\rho_2 - \rho_1|$), and thus the velocity scale of rising and migration is $U = \Delta\rho g a^2/\mu$. The droplet motion and shape is

affected by the viscosity ratio λ and the Bond number B_d defined by

$$B_d = \frac{\Delta\rho g a^2}{\gamma} \tag{5.1}$$

For convenience, we assume that the density of the droplet is smaller than that of the surrounding fluid, and thus the droplet rises. However, our study also represents a heavier droplet sedimenting in an otherwise quiescent fluid. In this study, we consider highly viscous liquid, i.e., , we neglect the inertia effects on the drop dynamics and assume a diminishing Reynolds number. Therefore, the governing equations of this problem are the Stokes equations and the continuity. The boundary integral equation (2.10) and the boundary conditions (2.8,2.9,2.11,2.12) given in Chapter 2 are employed in problem solving. In addition, the undisturbed velocity and force far from the droplet are defined as $\boldsymbol{u}^{\infty} = 0$ and $\boldsymbol{f}^{\infty} = 0$, respectively.

As shown in figure 5.2, the droplet interface is discretized into six initially equal-sized spectral elements while the solid surface is discretized into a central square element surrounded by a moderate number of rows of elements, each of which is composed by four elements. In our computations, the radius of the solid surface (which formally should extend to infinity) is at least 14 times the characteristic drop radius a; this creates negligible error in all cases. In our discretization method, geometry of the solid wall follows the rising of the droplet by aligning the center of the solid with the droplet centroid. We define the initial location of the solid center as the origin of the global Cartesian coordinate system. To avoid severe grid distortion on the droplet interface due to the droplet's translation, in the kinetics condition of the droplet interface given by equation (3.3) we employ the tangential

velocity as

$$U_t = c_t(\boldsymbol{u} \cdot \boldsymbol{t}) + (1 - c_t)(\boldsymbol{u}_c \cdot \boldsymbol{t}) \tag{5.2}$$

where $\boldsymbol{u}_c$ is the droplet's translational velocity measured from the droplet centroid while in most of the computations we applied $c_t = 0$. We may interpret the combination of equation(3.3) and equation (5.2) as the case that the grid on the droplet interface is first translated by the droplet translational velocity and then deformed (with respect to its new centroid) in a manner similar to that described earlier for free-suspended droplets with a fixed centroid.

5.2 Results and Analysis

Plotted as a function of time, the centroid position of a buoyant droplet with $\lambda = 1$ released at an initial distance $z_{c0} = 1.5$ from a vertical wall is shown in figure 5.3(a,b). The figure demonstrates that the Bond number B_d has rather negligible effects on the vertical position of the droplet but it affects greatly the droplet lateral position. In figure 5.4, the centroid trajectory of the buoyant droplet is plotted with respect to its $x-$ and $z-$ coordinate. The less buoyant droplet (i.e., with smaller B_d) is thus demonstrated to experience more rising than lateral migration.

The influence of Bond number B_d is shown more clearly in figure 5.5 where the droplet velocity is plotted as a function of time. The droplet rising velocity U_x first decreases and then shows a steady increase towards its highest value, i.e., the terminal velocity in an unbounded fluid [52, 86] which in dimensionless form is

$$U_x^{\infty} = \frac{2(1+\lambda)}{6+9\lambda} \tag{5.3}$$

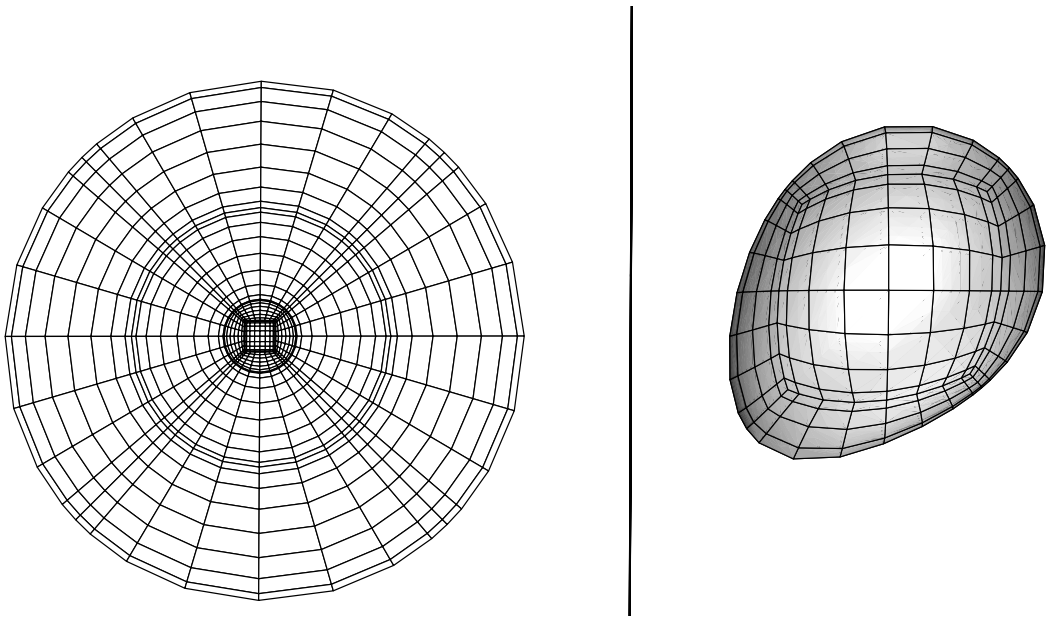

(a) (b)

Figure 5.2: Geometric discretization for a buoyant droplet moving near a vertical wall. (a) The solid wall defined as a circular plate. (b) The interfacial geometry of a droplet with $B_d = 3$ and $\lambda = 1$ at a distance of $z_c = 1.61$ from the wall. The droplet deforms from an initially spherical droplet with $z_{c0} = 1.5$.

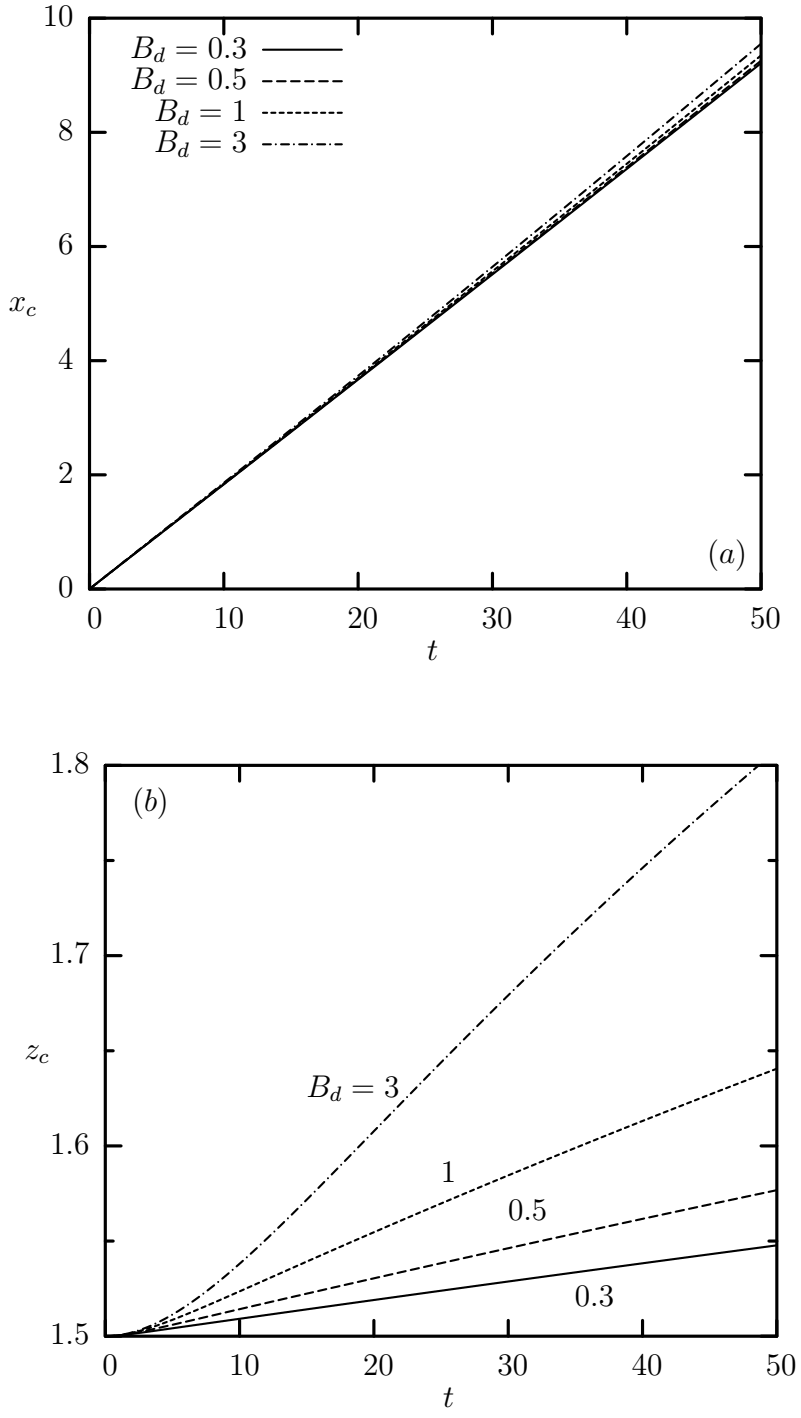

Figure 5.3: Time evolution of the position of a droplet with $\lambda = 1$ for Bond number $B_d = 0.3, 0.5, 1, 3$: (a) droplet centroid coordinate x_c, and (b) droplet centroid coordinate z_c. The initial drop lateral location is $z_{c0} = 1.5$.

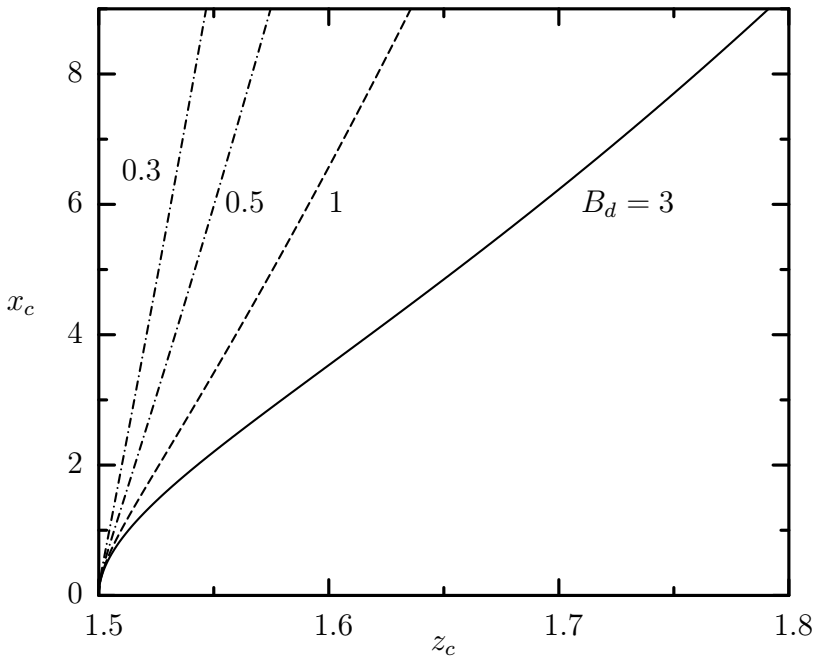

Figure 5.4: Centroid trajectory of a droplet with $\lambda = 1$ for Bond number $B_d = 0.3, 0.5, 1, 3$. The initial drop lateral location is $z_{c0} = 1.5$.

which shows that in an unbounded flow the droplet rising velocity doesn't depend on B_d. However, in the existence of a vertical solid wall, figure 5.5 shows a monotonic increase of the rising velocity U_x with the increase of B_d. On the other hand, as shown in figure 5.5(b), the droplet migration velocity U_z first demonstrates a dramatic increase and then gently diminishes towards its zero value far from the wall. In the figure, the curves for $B_d \leq 1$ do not form a plateau but slowly decreases over time. The migration velocity U_z is larger for higher B_d; this results from both the increased rising velocity U_x as well as the increased interfacial deformation D shown later in figure 5.9.

We now start to investigate the relation between the vertical motion of the droplet and the droplet's lateral position. As shown in figure 5.6, in the existence of a solid wall, the Bond number B_d slightly affects the rising velocity U_x when the drop is in close vicinity to the wall, and the effect extends to a distance of ~ 1.7 times droplet size. As the drop migrates farther away from the wall, the rising velocity becomes completely independent of the Bond number. To show the influence of the solid wall on the droplet velocity for a larger distance, in figure 5.7 we plot U_x versus z_c for droplets with the same Bond number and viscosity ratio, but starting from different initial position, i.e., $z_{c0} = 1.5, 2, 2.5, 3, 3.5$. As the distance between the droplet and the wall increases, the wall influence on the rising velocity becomes weaker and can be negligible after a large distance. We also include in figure 5.7 the rising velocity of a spherical droplet based on the zero-order analysis found in the recent study of Magnaudet, Takagi and Legendre [52]. Based on their spherical approximation, the maximum rising velocity (i.e., that in an unbounded fluid) can

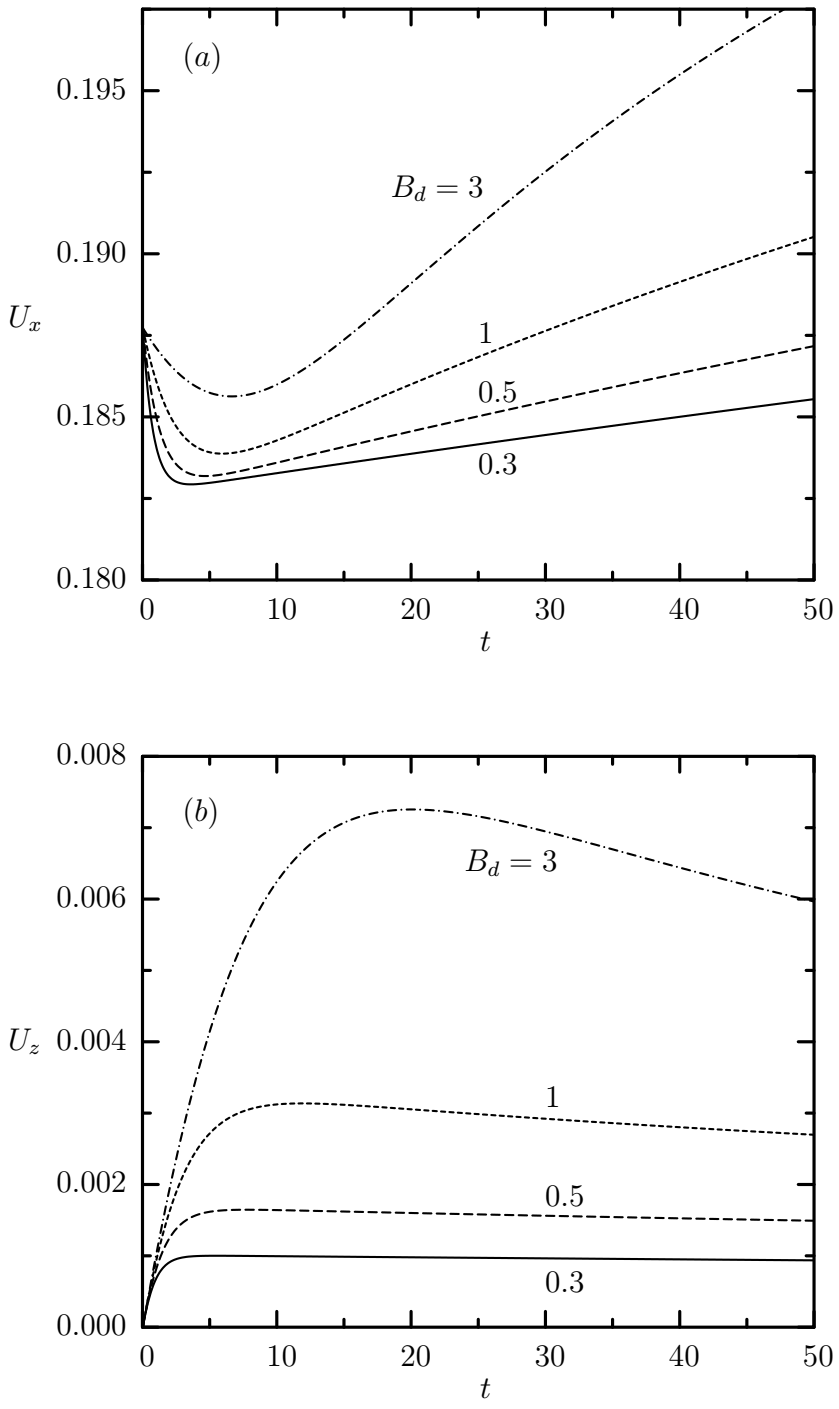

Figure 5.5: Time evolution of the velocity of a droplet with $\lambda = 1$ for Bond number $B_d = 0.3, 0.5, 1, 3$: (a) rising velocity U_x, and (b) migration velocity U_z. The initial drop lateral location is $z_{c0} = 1.5$.

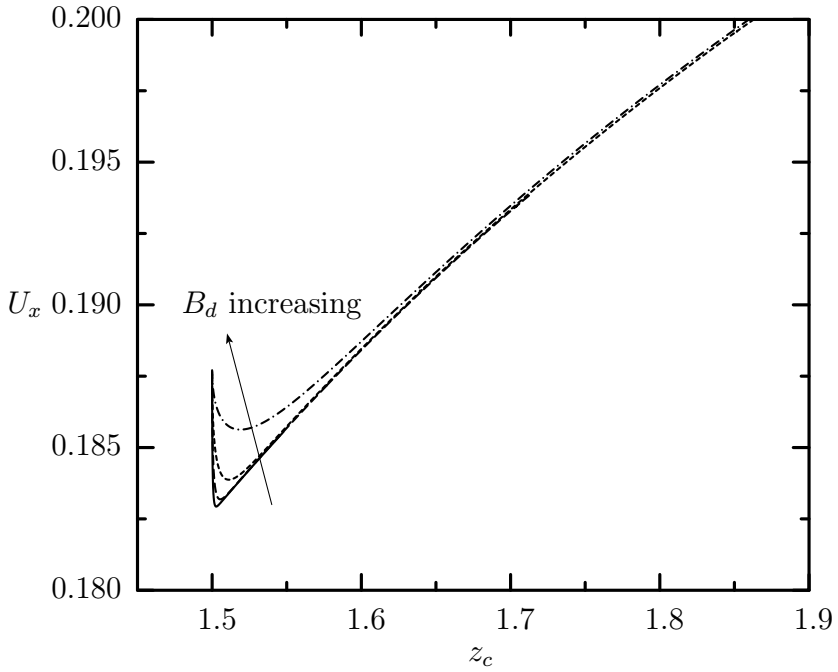

Figure 5.6: Rising velocity U_x of a droplet with $\lambda = 1$ versus its lateral position z_c for $B_d = 0.3, 0.5, 1, 3$. The initial droplet location is $z_{c0} = 1.5$.

be found in a distance from the wall about 20-30 times the droplet size. Comparing our results for the actual rising velocity U_x of a deformed droplet with that from the spherical approximation, we observe that only close to the wall and for a high Bond number the actual U_x shows a variation from its spherical approximation. In addition, this figure also demonstrates that the spherical approximation is only valid for droplets migrating at a distance of a few droplet radii to the wall.

The interfacial shape of the droplet is shown in figure 5.8. The droplet profiles at the intersection with plane $x = x_c$, $y = y_c$ and $z = z_c$ are demonstrated at different times ($t = 0, 20, 90$) during the translation of a droplet with $B_d = 3$ and $\lambda = 1$. The initial spherical shape has been deformed and rotated reaching its

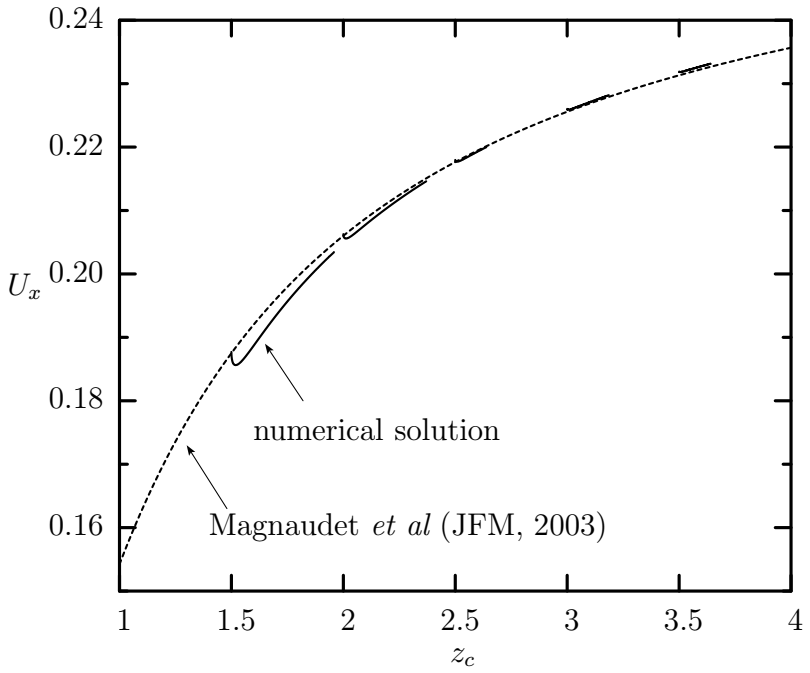

Figure 5.7: Rising velocity U_x of a droplet with $\lambda = 1$ versus its lateral position z_c for $B_d = 3$. The initial droplet location is $z_{c0} = 1.5, 2, 2.5, 3, 3.5$. Also included is the rising velocity of a spherical droplet (- - - -) at a distance z_c from the wall found in Ref. [52].

maximum deformation near time $t = 20$; later the droplet shows a slow relaxation towards its undisturbed shape as it migrates slowly away from the wall.

Figure 5.9 shows the droplet deformation D as a function of time for several different Bond number B_d. We define the deformation parameter as $D = (L - S)/(L + S)$ based on the droplet semi-axes determined as the maximum L and minimum distance S from the droplet centroid. Due to the asymmetric interfacial shape of the droplet moving near a solid wall, the deformation D in this section may differ from that for a free-suspended droplet. Figure 5.9 reveals that the interfacial deformation experiences an initially fast increase followed by a slow decrease towards its zero value far from the wall. The droplet shows an increased deformation by increasing the buoyant effects (i.e., the Bond number B_d). We note that the time evolution of the droplet deformation D is quite similar to that of the migration velocity U_z presented in figure 5.5(b). This similarity verifies the fact that the droplet's lateral motion is deformation-induced under Stokes flow conditions [8, 52].

By defining the orientation angle θ_z between the major semi-axis L of the droplet and the negative z-axis as shown in figure 5.10, we plot the evolution of the droplet orientation θ_z as a function of time under the influence of the Bond number B_d in figure 5.11. We observe that the spherical droplet, immediately after left to rise, shows an initial large rotation, corresponding to $\theta_x \approx 35^\circ$ independent of the Bond number B_d. The droplet orientation then increases rapidly with time while later the droplet rotates slower towards its final configuration far from the wall.

Figure 5.12 shows the droplet deformation D as a function of the lateral position z_c. We observe that the initially spherical droplet deforms significantly at first

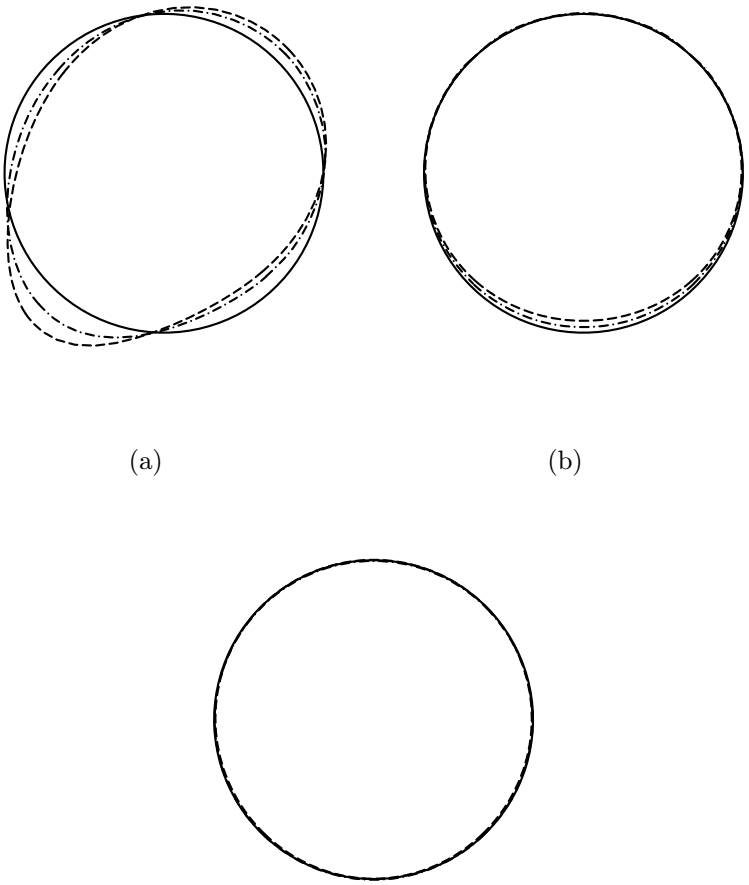

(a) (b)

(c)

Figure 5.8: Droplet profiles at the intersection with plane (a) $y = y_c$, (b) $x = x_c$, and (c) $z = z_c$, for $B_d = 3$ and $\lambda = 1$ at different times: ——, t=0; - - - -, t=20; – · –, t=90. The droplet locations at time $t = 0, 20, 90$ are $(x_c, z_c) = (0, 1.5)$, $(3.74, 1.61)$, $(17.63, 2.02)$ respectively. For all cases, $y_c = 0$. The profiles at different times are aligned at the initial location to demonstrate the interfacial deformation.

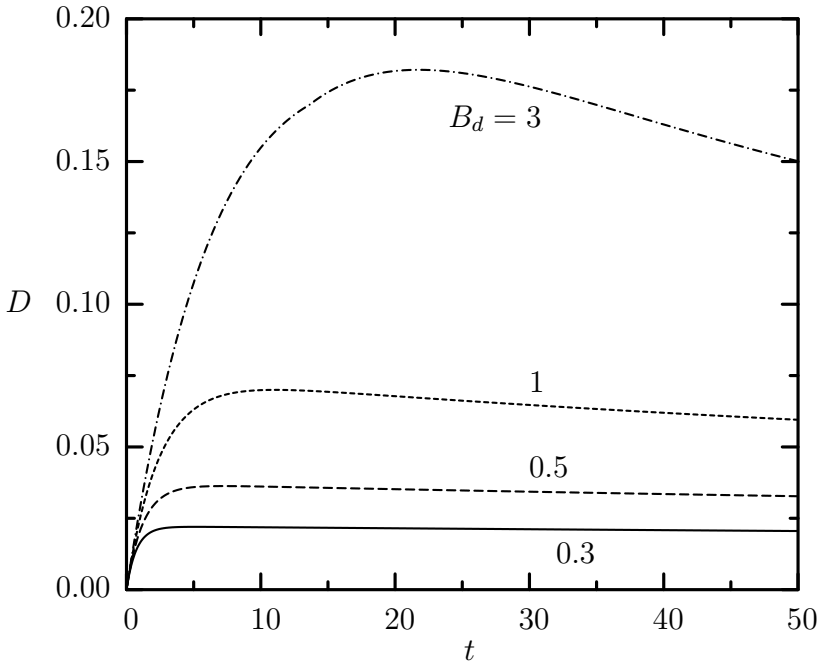

Figure 5.9: Time evolution of the deformation D of a droplet with $\lambda = 1$ for Bond number $B_d = 0.3, 0.5, 1, 3$. The initial drop location is $z_{c0} = 1.5$.

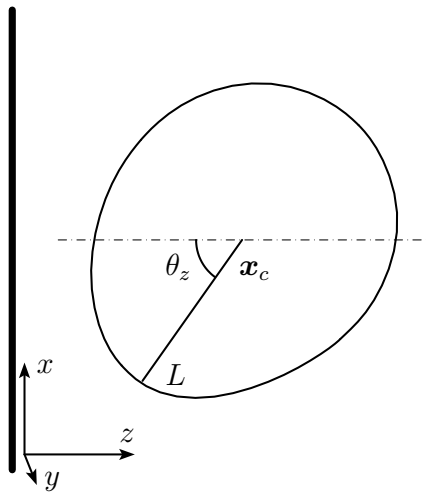

Figure 5.10: Illustration of the droplet orientation θ_z.

without any substantial lateral migration. After the maximum deformation has been reached, the droplet shows a slow relaxation towards its spherical shape as it migrates away from the wall. The figure also shows that the droplet deformation increases with the Bond number B_d. In addition, we include the analytical predictions for the droplet deformation of $O(z_c^{-3})$ and $O(z_c^{-5})$ by employing equation (14b) and (18) from Ref. [52]. (Note that for the analytical prediction of $O(z_c^{-5})$, the terms denoted as M_4 and M_5 have not been provided in Ref. [52] due to the algebraical complexity and their expected limited contribution; this is the reason that we include both predictions in our figure 5.12.) The analytical results for deformation D agree very well with the numerical calculations, especially for the droplet at a further distance from the wall and for smaller Bond numbers.

We consider the migration velocity U_z as a function of the lateral position z_c as shown in figure 5.13 for different Bond numbers and viscosity ratios. The dependence of U_z on z_c is quite similar to that of the interfacial deformation D shown

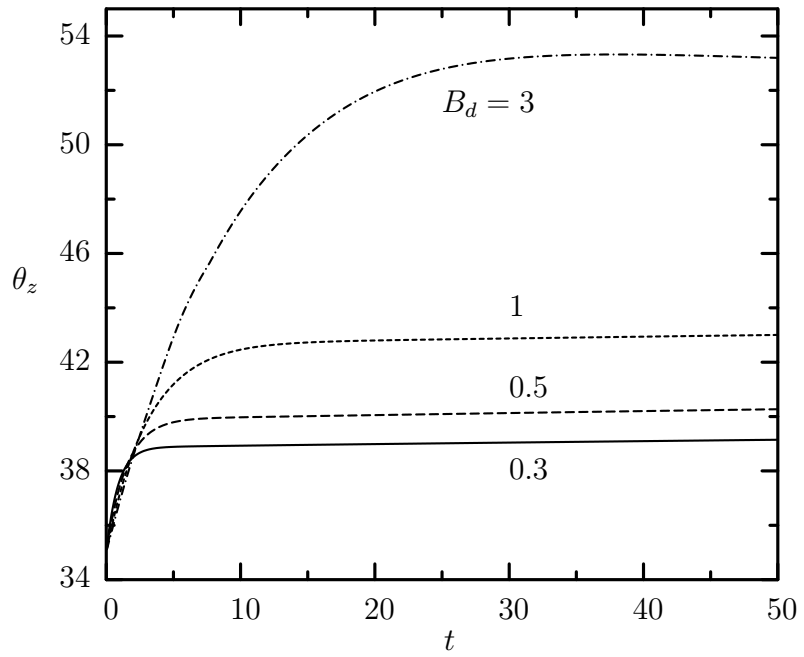

Figure 5.11: Time evolution of the orientation angle θ_z of a droplet with $\lambda = 1$ for Bond number $B_d = 0.3, 0.5, 1, 3$. The initial drop location is $z_{c0} = 1.5$.

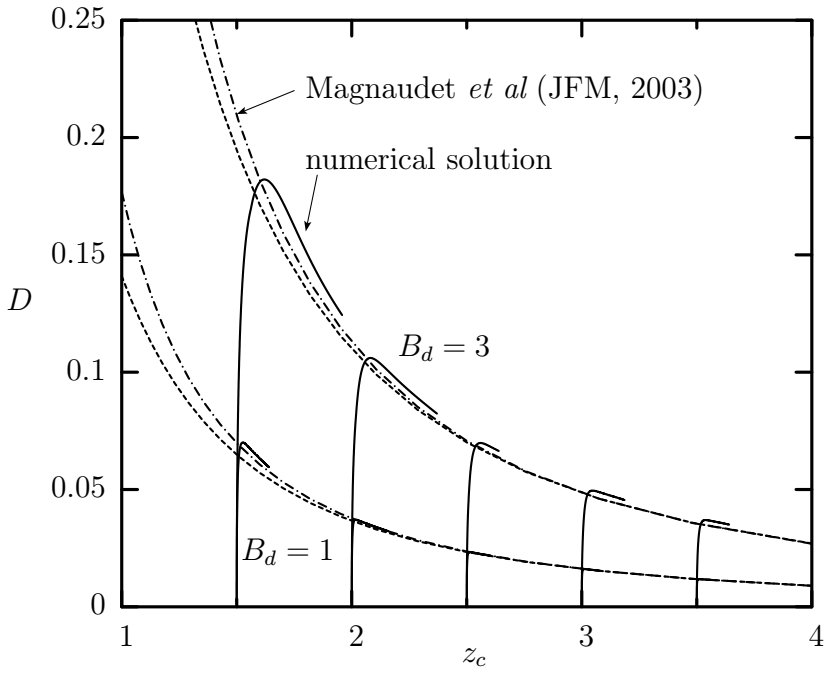

Figure 5.12: Deformation D versus lateral position z_c for a droplet with $\lambda = 1$ and for Bond number $B_d = 1, 3$. The initial drop location is $z_{c0} = 1.5, 2, 2.5, 3, 3.5$. Also included are the analytical predictions for deformation D of $O(z_c^{-3})$ (- - - -) and $O(z_c^{-5})$ (– · –) from Ref. [52].

in figure 5.12. Once the droplet is left to rise at a location close to the solid wall, the droplet migration velocity rapidly increases until the interfacial shape reaches its maximum deformation. Afterwards, as the droplet moves away from the wall, both the deformation and the migration velocity show a slow relaxation towards zero far from the wall. We note that the droplet deformation and migration velocity are higher for a larger Bond number with a given viscosity ratio. The best z_c^{-2} fitting based on the decreasing velocity is provided in the figure. Observe that during the relaxation, the migration velocity decreases inversely with the square of the lateral position for all cases studied as commonly found in drop motion near solid walls [8]. Figure 5.13 also includes the influence of the viscosity ratio on the droplet migration velocity for a given Bond number. The more viscous droplet appears to migrate more slowly in the lateral direction. In order to investigate the viscosity influence on both the deformation D and the migration velocity U_z, we plot D and U_z as functions of time t in figure 5.14. The figure demonstrates that for a smaller viscosity ratio λ, the droplet deforms more rapidly and thus experiences faster increase in the lateral velocity until the droplet reaches its maximum deformation. Afterwards, the less viscous droplet relaxes at a faster rate, so that the migration velocity experiences a faster decrease towards zero far from the wall. Therefore, we conclude that the migration velocity U_z is not only influenced by the droplet deformation but it is also affected by the rate of deformation.

Although our numerical results agree well with the analytical predictions by Magnaudet, Takagi and Legendre [52] in the range of $\lambda B_d \geq 1$ as shown in figure 5.12, we disagree with their prediction based on a quasi-steady assumption,

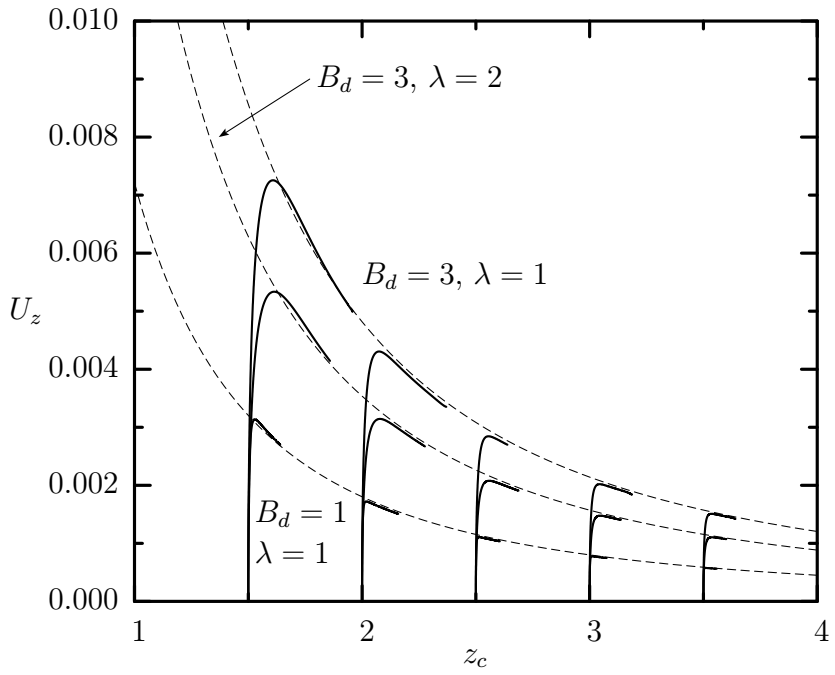

Figure 5.13: Migration velocity U_z versus lateral position z_c for a droplet with $\lambda = 1, 2$ and for Bond number $B_d = 1, 3$. The initial drop location is $z_{c0} = 1.5, 2, 2.5, 3, 3.5$. Also included is the best z_c^{-2} fitting $(- - -)$ based in the decreasing velocity.

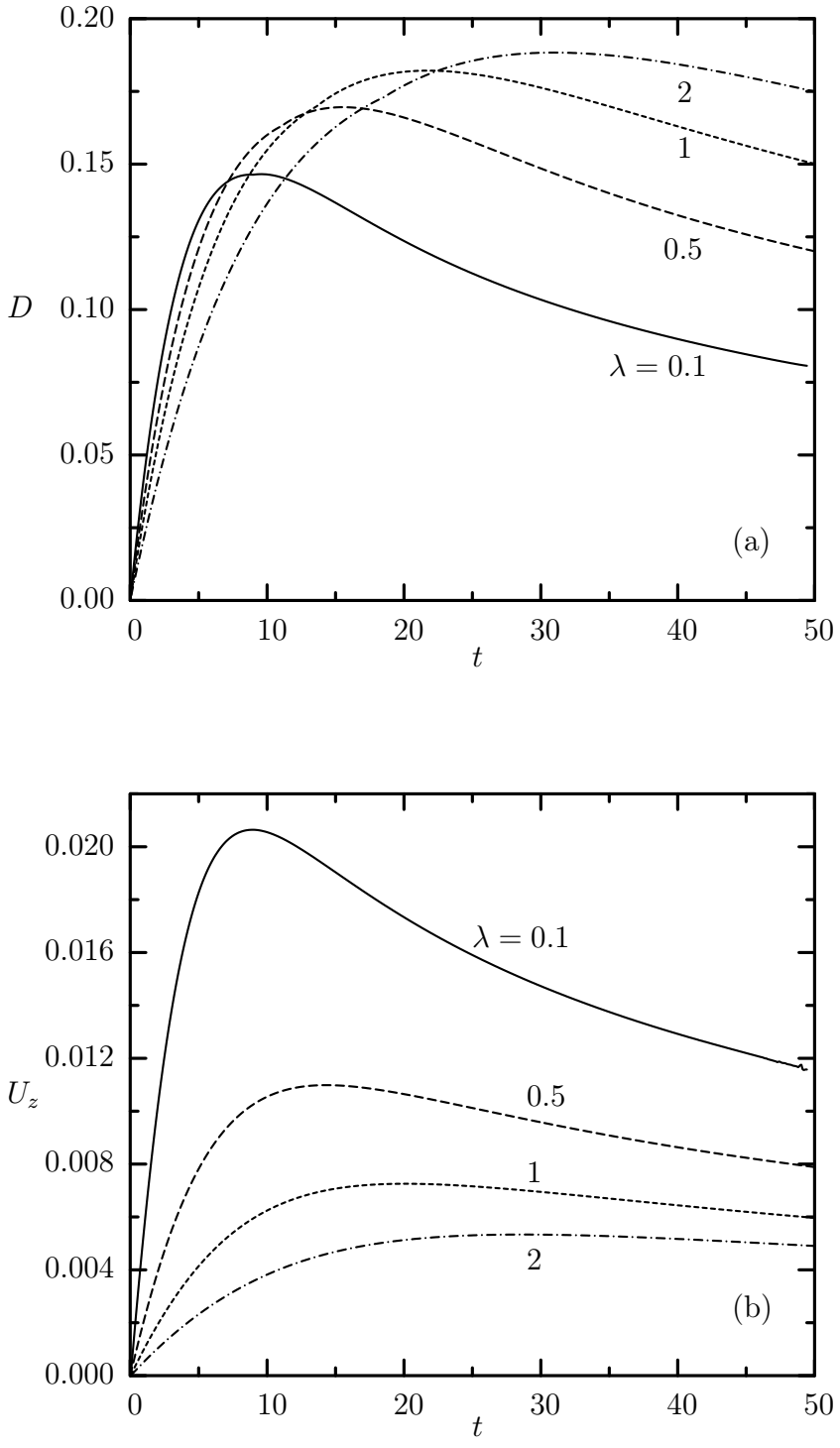

Figure 5.14: Time evolution of the deformation D and migration velocity U_z of a droplet near a vertical wall with Bond number $B_d = 3$ for $\lambda = 0.1, 0.5, 1, 2$. The initial drop lateral location is $z_{c0} = 1.5$.

which concludes that the droplet moves toward the wall for $0.21 < \lambda < 3.12$ when $\lambda B_d < 1$. Figure 5.5 evidently shows the droplet migration away from the wall for $\lambda = 1$ and various B_d. Therefore, we suspect that the analytical prediction of lateral motion towards the wall is erroneous, at least for the parameter space investigated in this study ($B_d \geq 0.3$ and $\lambda \geq 0.1$).

5.3 Conclusions

For this section, we conclude that as a viscous droplet rises or sediments along a solid wall, the droplet migrates away from the wall due to its own deformation. The wall effect diminishes as the droplet translates away from the wall. We find that the influence of the Bond number B_d on the rising velocity U_x only extends to a distance of a few times of the droplet size from the solid wall. The droplet deformation and the migration velocity are higher for a larger Bond number with a given viscosity ratio; while the more viscous droplet shows a smaller migration velocity for a given Bond number. After achieving its maximum value, the migration velocity decreases inversely with the square of the lateral position. Our study on a variety of viscosity ratio also demonstrated that the droplet migration velocity U_z is not only influenced by the deformation but also affected by the rate of deformation. There is no observation that the droplet migrates towards the wall for the viscosity ratio and Bond number considered in this study ($\lambda \geq 0.1$ and $B_d \geq 0.3$).

Chapter 6

Interfacial Dynamics in a Microfluidic Channel

Studying droplet behavior in microfluidic channels is of great importance in applications involving droplet mobilization, such as the enhanced oil recovery, microfluidic devices, and the coating of monolithic structures. In this chapter, we first describe the physical problem and the numerical method we employ. We also validate our method by comparing our results with previous calculations and experimental findings. We then focus on our investigation on the influence of physical parameters (the drop size, capillary number, and the viscosity ratio) on the droplet shape and motion in the channel.

6.1 Problem Description

Figure 6.1 illustrates a droplet (fluid 1) with density ρ_1 and viscosity $\lambda\mu$ driven by another immiscible fluid (fluid 2) with density ρ_2 and viscosity μ to move in a capillary with a comparable size. (Note that we generally refer to a micron-sized channel or tube as a capillary.) The buoyancy influence is neglected. We assume that the fluid is free of surfactant and that the temperature is kept constant; the

surface tension γ is assumed constant over the interfacial surface. The droplet volume V is reflected in its characteristic length $\tilde{a} = (3V/4\pi)^{1/3}$. The size of the capillary is denoted as R, which is the radius of a cylindrical tube or that of the circle subscribing the square cross section of the channel. The droplet translating velocity in the direction of x-axis is denoted as U_x, which may be different from the average flow velocity U, as we will explore later in this chapter.

The droplet volume centroid is denoted as $\boldsymbol{x}_c = (x_c, y_c, z_c)$. In figure 6.1, the drop is aligned with the centerline of the capillary (i.e., $y_c = 0$ and $z_c = 0$). In the case of a droplet released at a location off the capillary centerline, we denote $(0, 0, z_{c0})$ as its initial location. Note that in sections 6.2 – 6.5, we investigate the case of a droplet moving along the capillary centerline, therefore there is no cross-stream droplet migration taking place. We study the droplet cross-stream migration in section 6.6. In this section, the droplet is set free at a location off the center and may migrate in the direction of z-axis. In our study, the droplet velocity in the direction of y-axis is always zero due to the symmetry.

In the current problem, lengths are non-dimensionalized with the size of the channel R, velocity with the average bulk velocity U, and time with R/U. The droplet motion and shape are affected by the capillary number which is defined as $Ca = \mu U/\gamma$, the viscosity ratio λ, and the droplet size $a = \tilde{a}/R$.

For a viscous droplet moving in a capillary, the inertia may be ignored due to the low Reynolds number. The governing equations are the Stokes equation and the continuity. Therefore, the boundary integral equation (2.13) and corresponding boundary conditions presented in section 2.4 are applied. For a channel with a square

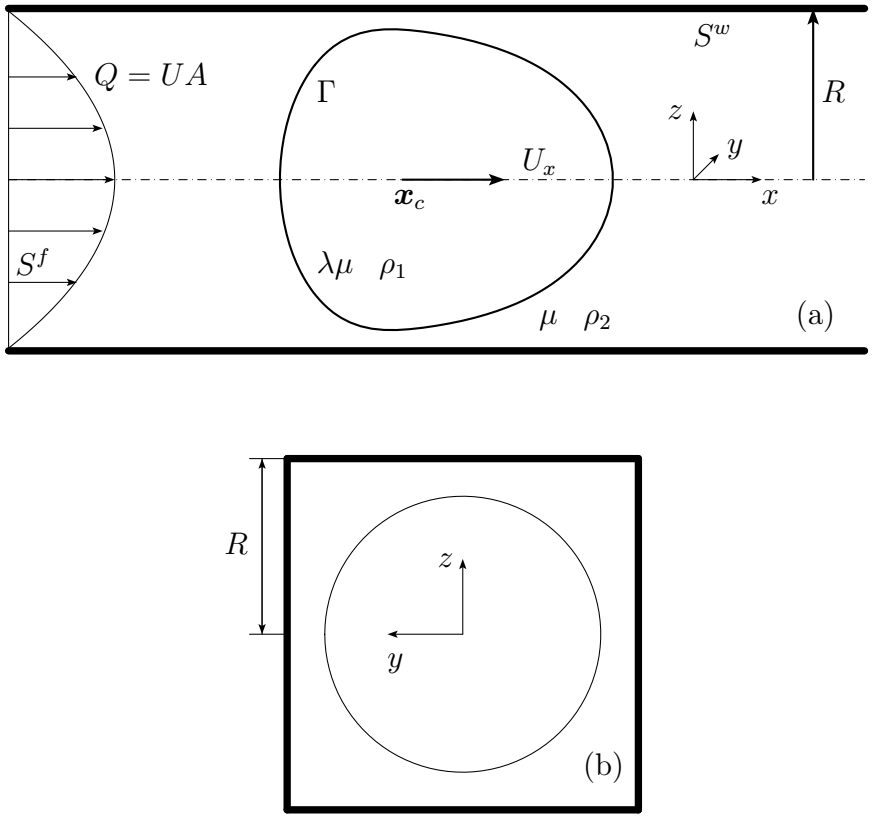

Figure 6.1: Illustration of a droplet moving along the centerline of a micron-sized channel. The geometry is shown at the intersection with (a) xz plane and (b) yz plane.

cross-section, the undisturbed flow far from the droplet $\boldsymbol{u}^{\infty}$ is a steady unidirectional flow [99], and may be expressed as

$$\frac{u_x^{\infty}}{C} = (1 - z^2) + \sum_{n=1}^{\infty} B_n \cosh(\alpha_n y) \cos(\alpha_n z) \tag{6.1}$$

where

$$C = \frac{-(\partial p/\partial x)}{2\mu} \tag{6.2}$$

$$B_n \cosh(\alpha_n) = (-1)^n \frac{4}{\alpha_n^3} \tag{6.3}$$

$$\alpha_n = \frac{(2n-1)\pi}{2} \tag{6.4}$$

The variables y and z are non-dimensionalized with size R. The flow rate Q and the average velocity U in the channel may be derived as

$$\frac{Q}{C} = \frac{8}{3} + \sum_{n=1}^{\infty} (-1)^n \frac{16}{\alpha_n^5} \sin(\alpha_n) \tanh(\alpha_n) \tag{6.5}$$

$$\frac{U}{C} = \frac{Q}{AC} = \frac{2}{3} + \sum_{n=1}^{\infty} (-1)^n \frac{4}{\alpha_n^5} \sin(\alpha_n) \tanh(\alpha_n) \tag{6.6}$$

where A denotes the non-dimensionalized cross-sectional area for the square channel ($A = 4$). By dividing equation (6.1) with equation (6.6), the non-dimensionalized flow velocity u_x^{∞}/U in the square channel is given by

$$\frac{u_x^{\infty}}{U} = \frac{(1 - z^2) + \sum_{n=1}^{\infty} B_n \cosh(\alpha_n y) \cos(\alpha_n z)}{2/3 + 4 \sum_{n=1}^{\infty} (-1)^n \sin(\alpha_n) \tanh(\alpha_n)/\alpha_n^5} \tag{6.7}$$

In our computation, the series in equation (6.7) is cut off after n=40 with a truncation error of $O(10^{-5})$. Note that we only consider a channel with a square cross-section in the current dissertation. The velocity distribution in the channel on a yz plane far from the droplet is shown in figure 6.2.

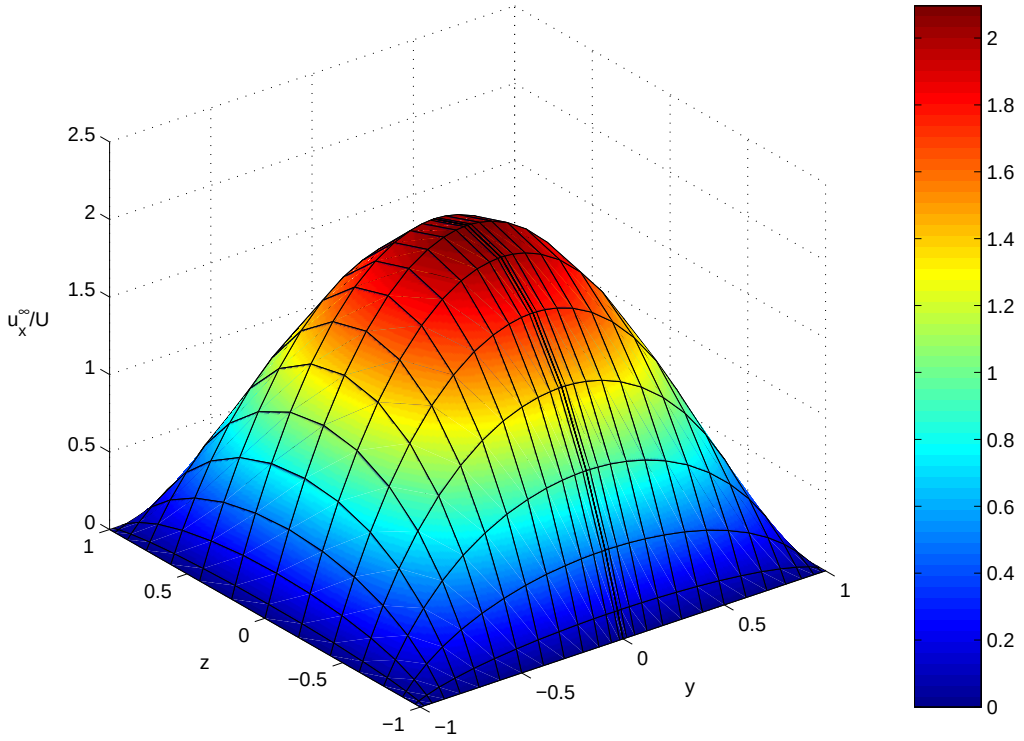

Figure 6.2: Velocity distribution for the unidirectional flow in a channel with square cross-section. The nodal lines correspond to the discretization of the fluid boundary in the spectral boundary element method.

The discretization of the square channel and the droplet is demonstrated in figure 6.3. The fluid boundary on the inlet and outlet of the channel is composed of two elements each as shown in figure 6.3(a). The semi-length of the channel/tube (which formally should extend to infinity) is at least 25 times the drop length in the flow direction; this creates negligible error in all cases. Seven rows of elements with 4 elements each are employed on the channel (only five rows are shown in the figure). For a droplet with size $\tilde{a} < R$, the droplet interface is divided into $N_E = 6$ elements as shown in figure 6.3(b) while the computations start with an initially spherical shape. For a droplet with size $\tilde{a} > R$, the interface is divided into $N_E = 10$ elements as shown in figure 6.3(c). In this case, we define the initial droplet shape as a prolate spheroid [88] having two minor semi-axes with a length of 0.9 and a varying length for the major semi-axis. The droplet's translational velocity is included in the kinetics condition of the droplet interface using equation (5.2) in section 5.1 in order to achieve a reasonable distribution of the spectral points on the interface.

The deformation parameter D for the elongated droplet moving along the channel centerline is defined as the ratio of the droplet length along the x-axis to that along the z-axis, $D = l_1/l_2$, as shown in figure 6.4.

6.2 Validation

We now validate our numerical results for droplet dynamics in cylindrical tubes by comparing with previously computational predictions and experimental findings. Figure 6.5 shows the steady-state profile of a droplet with viscosity ratio $\lambda = 0.1$

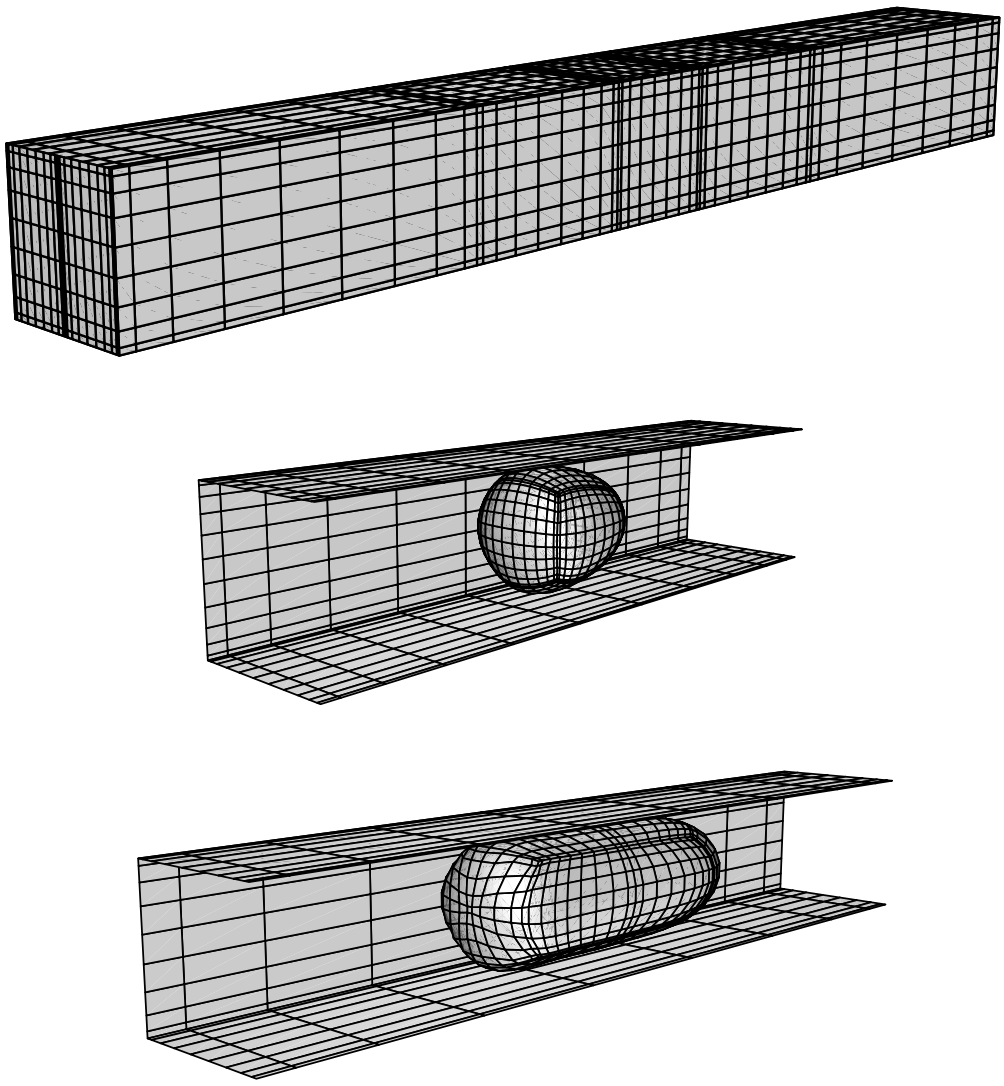

Figure 6.3: Surface discretization of a microfluidic channel and the droplet translating inside it: (a) discretization of the channel (more elements are assigned on the area close to the droplet); (b) a slightly deformed droplet with size $a = 0.9$ and with 6 spectral elements; (c) a significantly elongated droplet with size $a = 1.3$ and with 10 spectral elements.

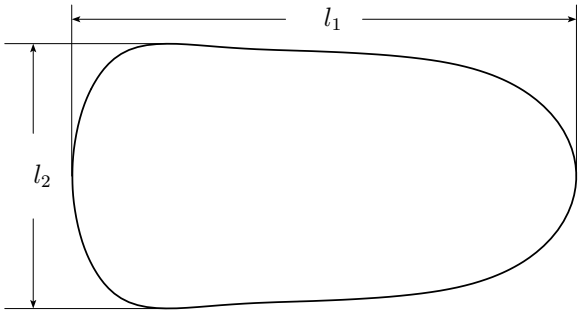

Figure 6.4: Illustration for the measurement of a significantly elongated droplet.

moving along the centerline of a cylindrical tube. Droplet shapes at the intersection with plane $y = 0$ are plotted for different capillary numbers $Ca = 0.05, 0.1, 0.2$. Excellent agreement is found by comparing our results (solid lines) to the computational results (points) by Tsai and Miksis [88]. Note that the nose of the droplet for different capillary numbers is aligned at the same location for the ease of observation.

Comparison has also been made in the case of a buoyant droplet rising in a cylindrical tube filled with another quiescent fluid. As shown in figure 6.6, the steady-state shape of a droplet with size $a = 0.92$, viscosity ratio $\lambda = 0.22$ and Bond number $B_d = 4.1$ is demonstrated and has been compared with figure 3(c) of Ref. [5], where the experimental image was taken for a droplet of UCON-1145 (a polyalkylene glycol based synthetic oil) rising in a suspending water solution with 98.5 wt% corn syrup. At 25 C°, the droplet density and viscosity are $995\,\mathrm{kg/m^3}$ and $528\,\mathrm{mPa\cdot s}$ respectively, while the suspending fluid has a density of $1375\,\mathrm{kg/m^3}$ and a viscosity of $2444\,\mathrm{mPa\cdot s}$. The corresponding interfacial tension is $0.0143\,\mathrm{N/m}$. The good agreement indicates that our method is accurate in predicting the behavior of a droplet moving in a confined geometry regardless of specific physical conditions.

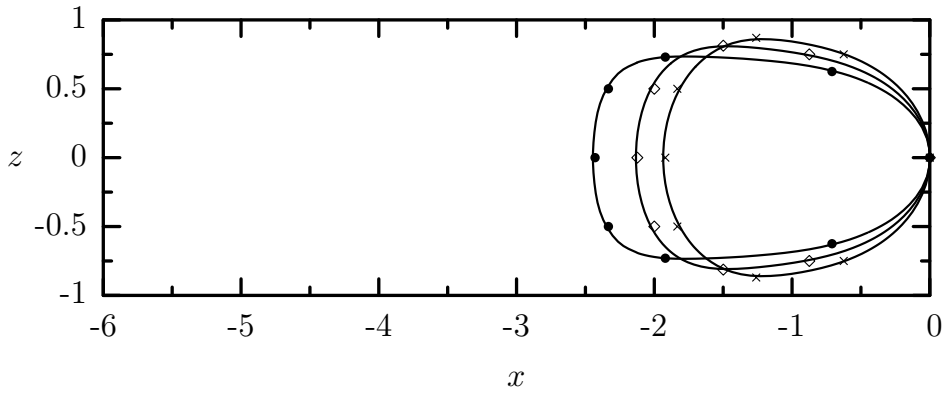

Figure 6.5: The steady-state profile for a droplet with $a = 0.9$, $\lambda = 0.1$ and $Ca = 0.05, 0.1, 0.2$ from right to left. Solid lines represent results from our 3D spectral boundary element method, while the crosses, open diamonds and solid circles denote results from Tsai and Miksis [88] for $Ca = 0.05, 0.1, 0.2$ respectively. The nose of each profile aligns at the same location for convenience of comparison.

6.3 Effect of the Drop Volume

We first examine the time evolution of the droplet shape. As shown in figure 6.7, a spherical droplet is deformed as it translates through the channel. At the beginning, the front region of the droplet is significantly sharpened while the rear is flattened. After a while, the elongation of the droplet body dominates the deformation and the droplet rear starts to regain some level of curvature. Finally at steady state, the droplet interface shows a bullet-like shape with high curvature in the front region. This typical profile is similar to the shape of a droplet moving in cylindrical tubes [39, 53, 88]. The three-dimensional geometry is shown in figure 6.8 for the droplet interface shape at different times.

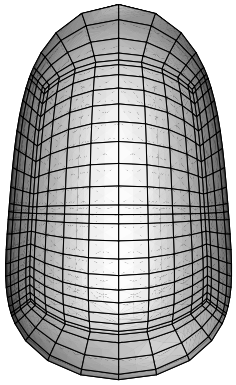

Figure 6.6: The steady-state profile of a droplet rising in a cylindrical tube. The drop size is $a = 0.92$. The viscosity ratio is $\lambda = 0.22$. The Bond number is $B_d = 4.1$. The numerical prediction in this study agrees with the experimental image taken by Borhan and Pallinti [5] in their figure 3(c), where UCON-1145 (a polyalkylene glycol based synthetic oil) was used as the drop fluid while the suspending fluid employed was a 98.5 wt% corn syrup-water mixture.

Now we focus on the behavior of droplets with different sizes. The droplet deformation D is shown as a function of time in figure 6.9(a). Several droplet sizes ($a = 0.6, 0.7, 0.8$) are considered. For all sizes, the droplet deformation D increases with time and eventually reaches a plateau at steady sate. We observe that smaller droplets achieve steady state faster but with a smaller deformation. Due to the relatively smaller size, the droplet is only slightly influenced by the slowly moving fluid near the solid wall. As a result, the shear stresses across the interface is small, and thus a smaller deformation is achieved. In figure 6.9(b), we also plot the time evolution of the droplet velocity in the flow direction. During the droplet translation, the droplet speed first decreases to its minimum value and then increases to reach

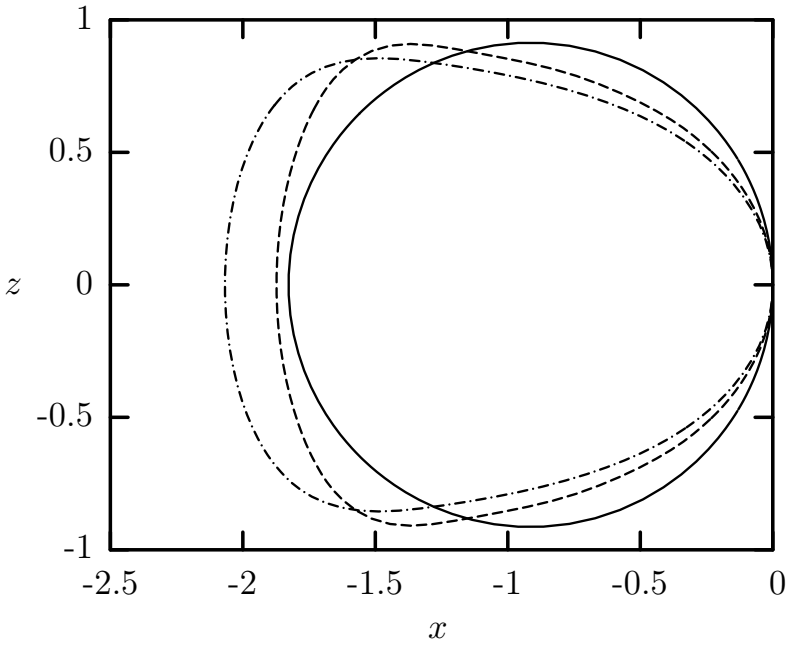

Figure 6.7: Profiles for a droplet with size $a = 0.914$ traveling in a square channel. Droplet shapes at the intersection with plane $y = 0$ are shown for time $t = 0, 0.8, 12$ from right to left. The viscosity ratio is $\lambda = 5$ and capillary number is $Ca = 0.1$. The profiles are presented such that the nose of each droplet begins at the same location for convenience of comparison.

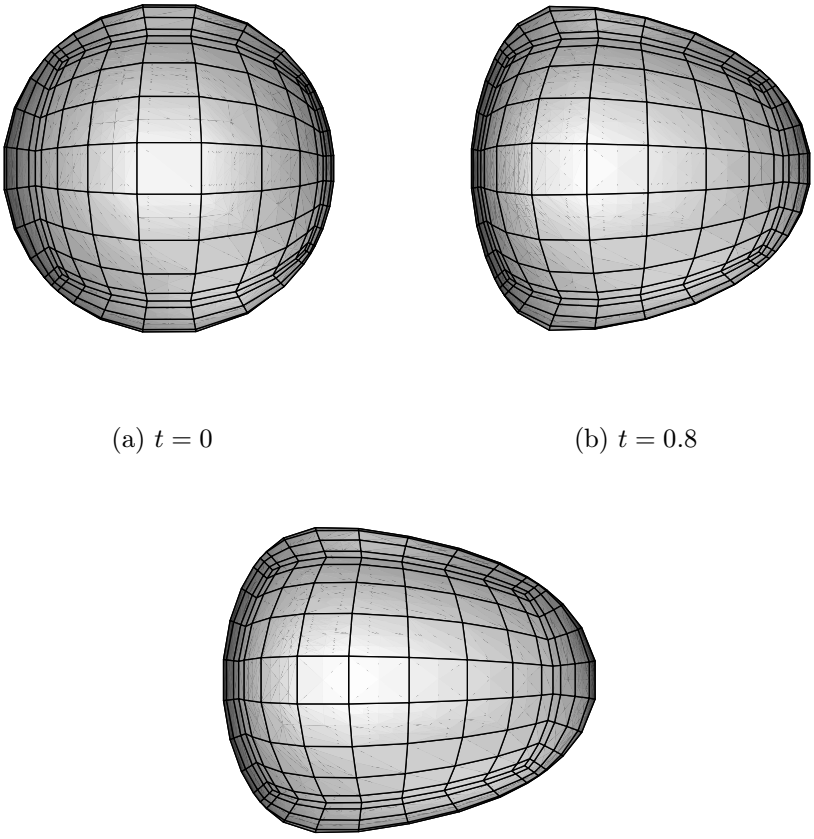

(a) $t = 0$ (b) $t = 0.8$

(c) $t = 12$

Figure 6.8: The time evolution for a droplet with size $a = 0.914$ traveling in a square channel. The viscosity ratio is $\lambda = 5$ and capillary number is $Ca = 0.1$.

a plateau. The velocity of a larger droplet shows a more dramatic change before steady state. We also note that the droplet velocity decreases with the increase of the drop size monotonicly.

The variation in the droplet shape at steady state with droplet size a are shown in figure 6.10. Small droplets (e.g. $a = 0.6$) almost maintain the spherical shape throughout the course of its translation. Larger droplets (e.g. $a = 1.0$ and 1.2), on the other hand, experience larger shear stress close to the channel wall. As a result, they obtain more significant deformation by elongating along the flow direction. The three-dimensional geometry of the corresponding droplet interface is shown in figure 6.11 for different droplet sizes.

6.4 Effect of the Capillary Number

As a measure of the relative importance of viscous forces to surface tension forces, a larger capillary number Ca causes a larger deformation as well as a faster translating velocity for a droplet moving in a channel. The effect of the capillary number Ca on the droplet velocity and deformation is demonstrated in figure 6.12 for a drop size $a = 0.8$ and viscosity ratio $\lambda = 2.04$. As predicted, the droplet deformation and velocity increases monotonicly with the capillary number. We also note that the droplet with a smaller capillary number reaches steady state earlier. As described in the previous section, the droplet initiates the translation at a moderate velocity. The velocity decreases at the beginning but increases dramaticly after a minimum is reached. Finally the droplet velocity achieves a plateau at steady state. For larger

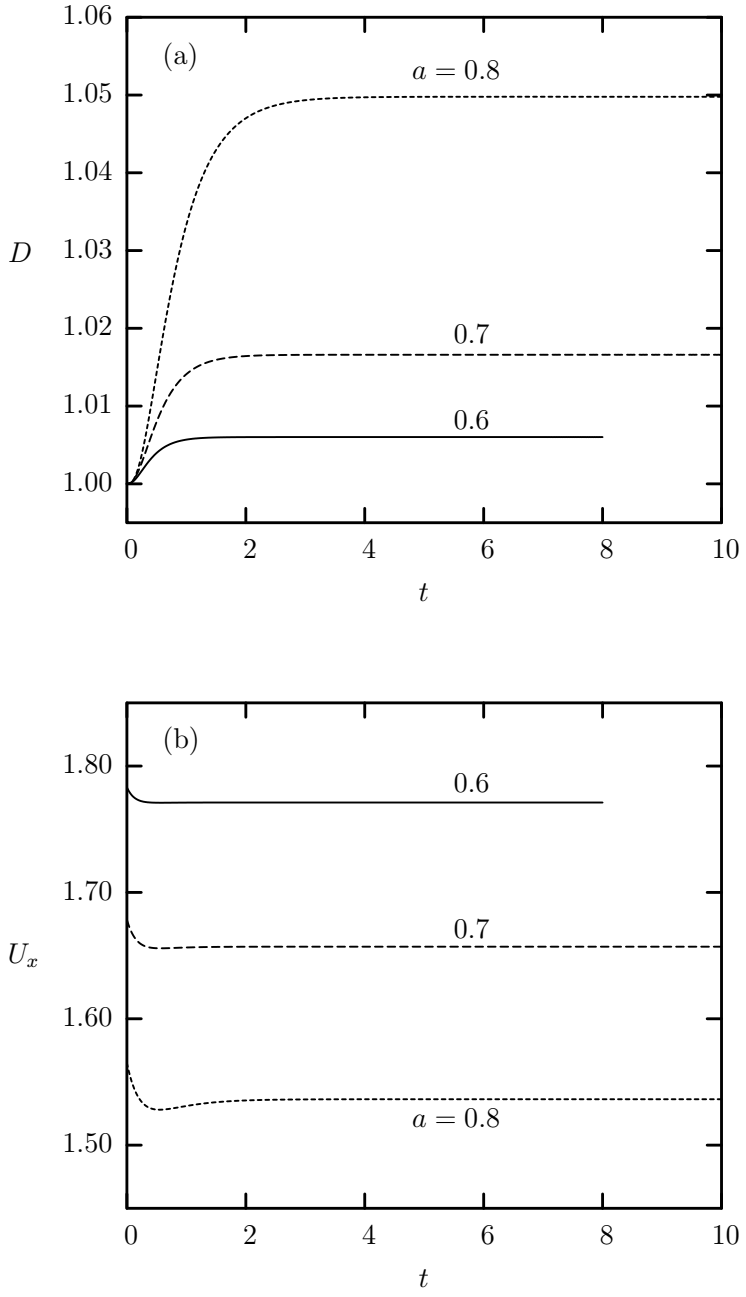

Figure 6.9: Deformation and velocity versus time for droplets with sizes $a = 0.6, 0.7, 0.8$ moving in a square channel. For all cases, the viscosity ratio is $\lambda = 2.04$ and the capillary number is $Ca = 0.1$.

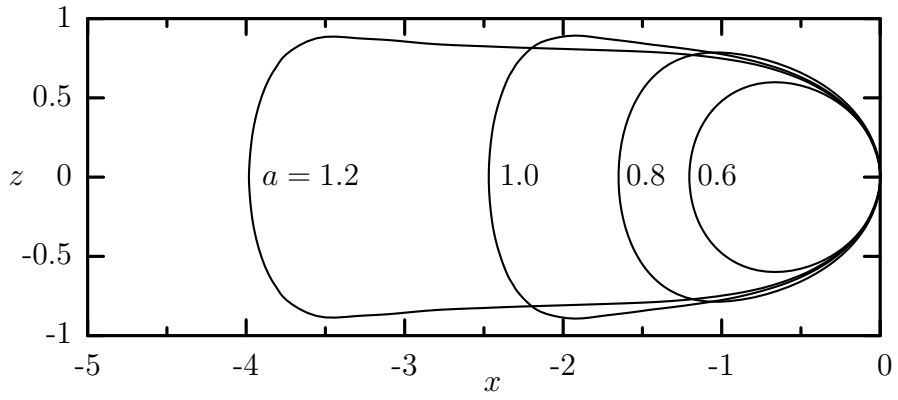

Figure 6.10: Variation in drop profile with drop size a at steady state. Size $a = 0.6, 0.8, 1.0, 1.2$ from right to left. For all cases, the capillary number $Ca = 0.1$ and the viscosity ratio $\lambda = 2.04$. The profiles are aligned at the droplet nose for convenience of comparison.

capillary numbers, the droplet velocity experiences a smaller decrease initially and a more dramatic increase after the minimum is reached.

We now consider the influence of the capillary number on the droplet shape. Figure 6.13 shows the droplet profile at the intersection with the plane $y = 0$ for a variety of capillary numbers. Two different droplet sizes are considered: $a = 0.8$ and 1.03. With the increase of the capillary number, the droplet nose is sharpened, the droplet body is elongated, and the rear is flattened. By comparing different sizes, we notice that the influence of the capillary number on the drop shape is more prominent for relatively larger droplets. As shown in figure 6.13(b), the droplet is obviously narrowed due to the significant elongation for larger capillary numbers. As a result, the minimum distance between the droplet and the channel wall increases

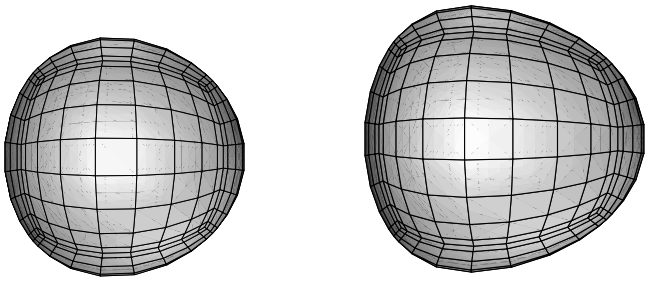

(a) a=0.6 (b) a=0.8

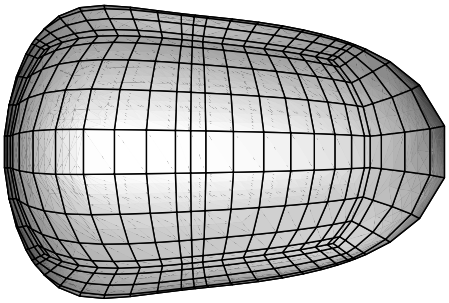

(c) a=1.0

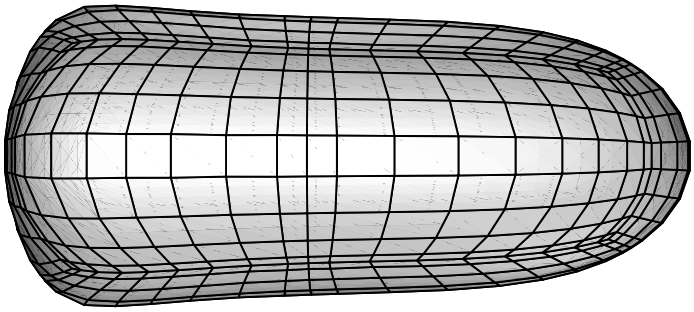

(d) a=1.2

Figure 6.11: Three-dimensional profiles for droplets with size $a = 0.6, 0.8, 1.0, 1.2$ moving in a square channel. For all cases, the capillary number is $Ca = 0.1$ and the viscosity ratio is $\lambda = 2.04$.

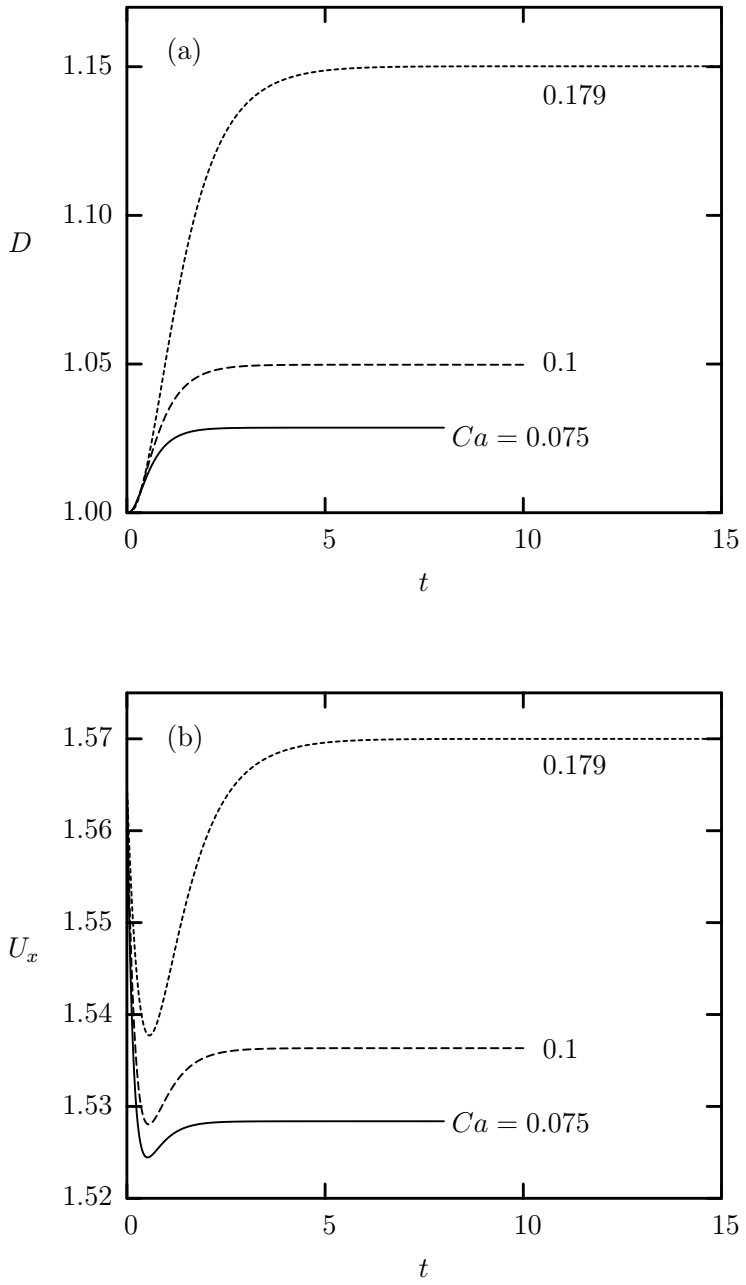

Figure 6.12: Deformation D and velocity U_x versus time t for a droplet with size $a = 0.8$ moving in a square channel. Different capillary numbers are shown $Ca = 0.075, 0.1, 0.179$. For all cases, the viscosity ratio is $\lambda = 2.04$.

with the capillary number, as shown in figure 6.14.

In figure 6.15(a), we plot the steady-state deformation D as a function of size a. Curves for different capillary numbers are included. In agreement with the previous finding, this figure clearly shows the dramatic increase of deformation D with Ca at large sizes. Figure 6.15(b) plots the steady-state velocity of the droplet as a function of the droplet size a for different capillary numbers. We observe that the capillary number has almost no effect on the droplet velocity for droplets with size $a \leq 0.65$. Similar to the deformation D, the droplet velocity U_x shows large increase with the capillary number for larger droplets.

6.5 Effect of the Viscosity Ratio

Figure 6.16 shows the transient behavior of the droplet deformation and velocity for different viscosity ratios. The droplet velocity U_x is significantly influenced by the viscosity ratio λ and shows a monotonic decrease with the increase of λ. On the other hand, the deformation D demonstrates a more complicated behavior with the increase of the viscosity ratio λ. We observe that the steady-state deformation is achieved later for a more viscous droplet, i.e., a more viscous droplet spends more time deforming from the initial shape to its final configuration at steady state.

Steady-state profiles of droplets with a given capillary number $Ca = 0.1$ are plotted in figure 6.17 for different viscosity ratios. Two droplet sizes are considered: $a = 0.8$ and 1.03. We note that for a small droplet, the droplet profile is not affected by the viscosity ratio even for the large range of viscosity ratio considered in this

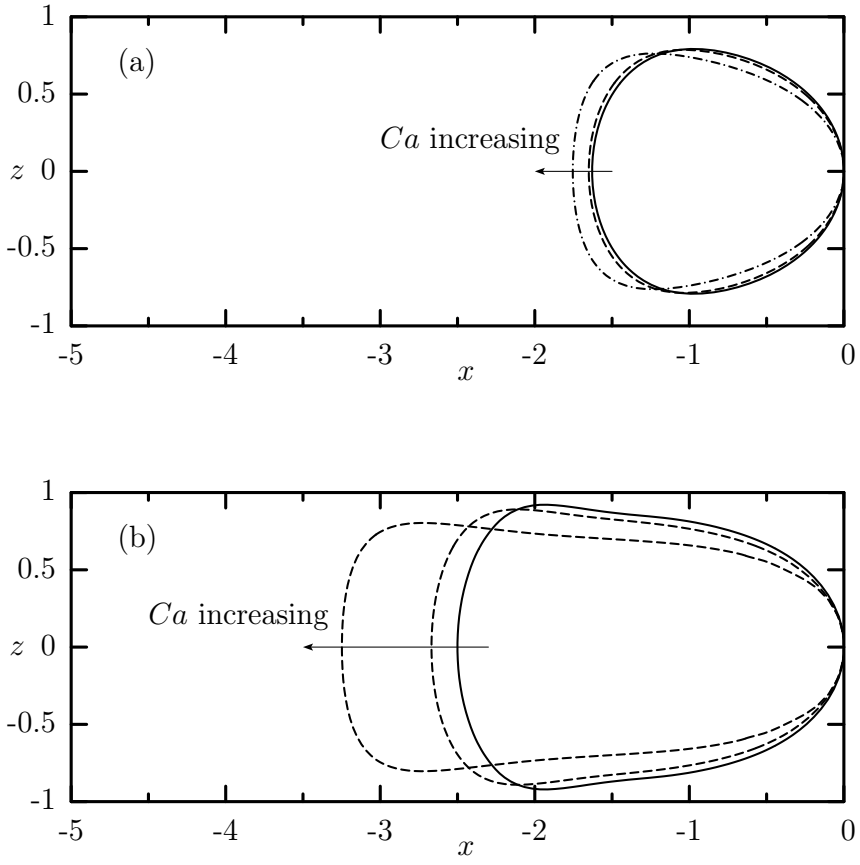

Figure 6.13: Variation in drop profile with the capillary number Ca at steady state. The upper figure shows a droplet with $a = 0.8$ and capillary numbers $Ca = 0.075, 0.1, 0.179$. The lower figure shows the profiles for a droplet with $a = 1.03$ and the same capillary numbers. For all cases the viscosity ratio is $\lambda = 2.04$.

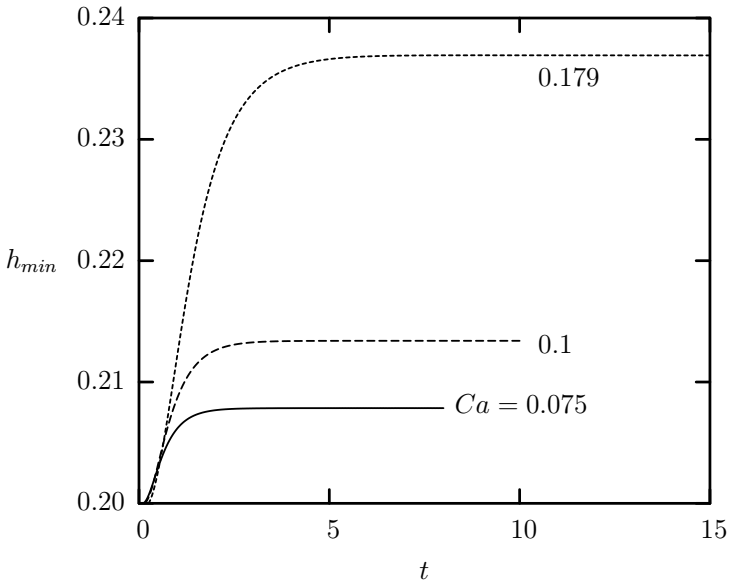

Figure 6.14: Time evolution of the minimum distance between the channel wall and the droplet with size $a = 0.8$. Different capillary numbers are shown $Ca = 0.075, 0.1, 0.179$. For all cases, the viscosity ratio is $\lambda = 2.04$.

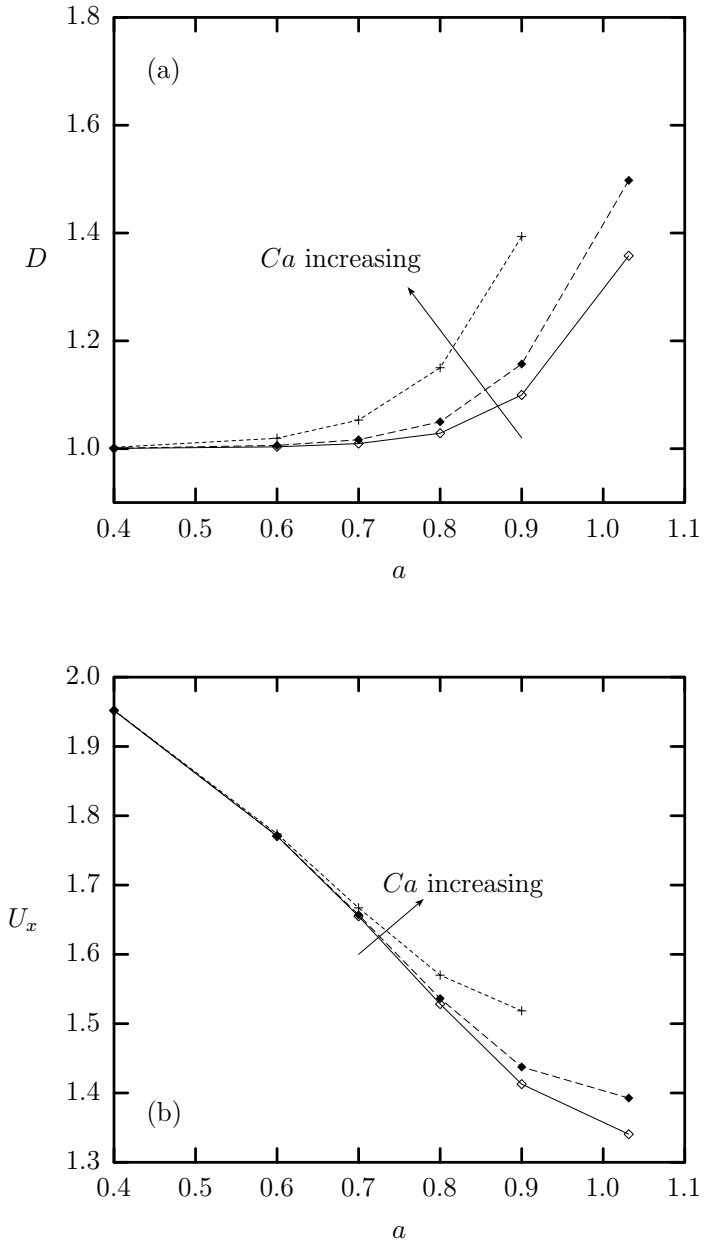

Figure 6.15: Droplet deformation D and velocity U_x as a function of drop size a at steady state for different capillary numbers: $Ca = 0.075$ (blank diamonds), $Ca = 0.1$ (filled diamonds) and $Ca = 0.179$ (crosses). The viscosity ratio for all cases is $\lambda = 2.04$.

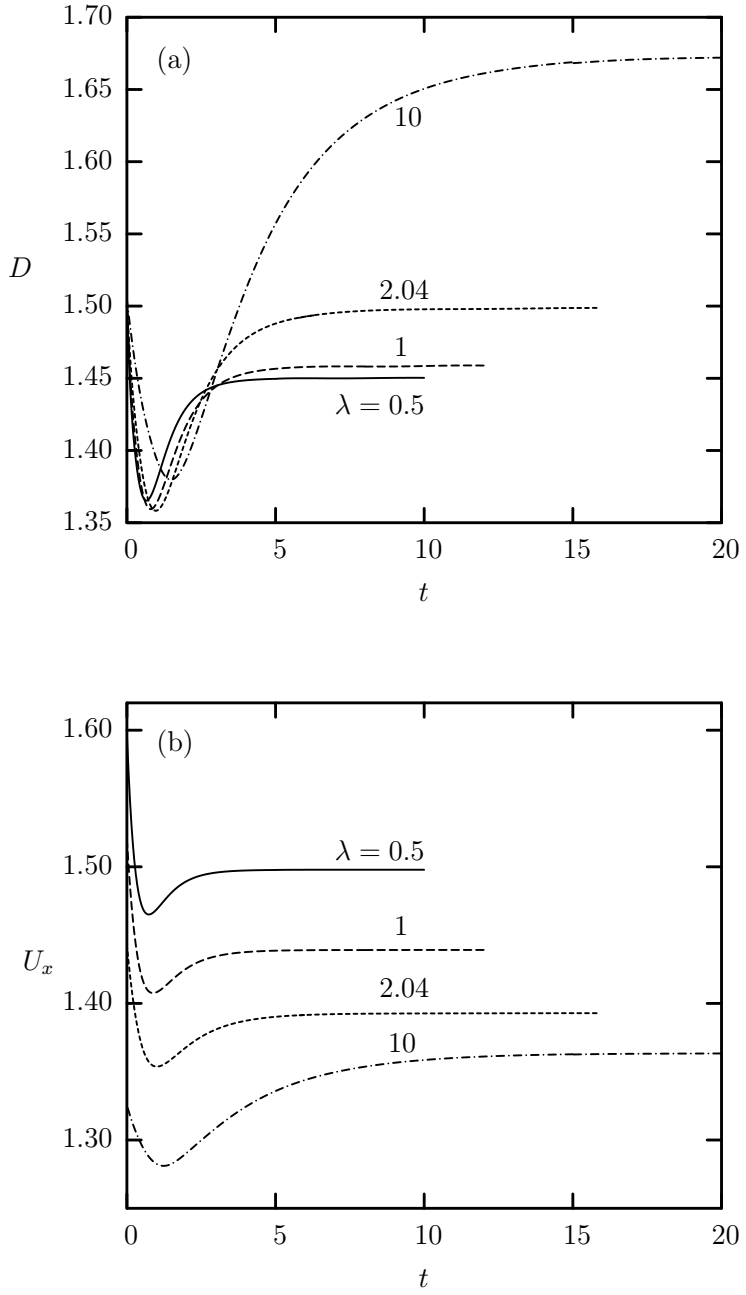

Figure 6.16: Deformation D and velocity U_x versus time t for droplets with size $a = 1.03$ traveling in a square channel. Different viscosity ratio is shown $\lambda = 0.5, 1, 2.04, 10$. For all cases, the capillary number is $Ca = 0.1$.

study ($0.19 \leq \lambda \leq 10$). For a large droplet, on the other hand, larger viscosity ratio causes sharper nose and larger elongation. And a thicker liquid film is also formed between the droplet and the channel wall.

In figure 6.18, we plot the droplet deformation D and velocity U_x at steady state as a function of the droplet size a under the influence of the viscosity ratio. We found that the droplet deformation is only evidently influenced by the viscosity ratio for sizes larger than 0.7, while the viscosity ratio has considerable effects on the steady-state droplet velocity for all sizes.

In order to further investigate the effect of the viscosity ratio, we plot the droplet deformation D as a function of the viscosity ratio λ as shown in figure 6.19(a). The droplet size is $a = 0.914$. The capillary number is given as $Ca = 0.1$. The deformation D shows an increase with the viscosity ratio for $\lambda \geq 1$ while it is almost independent on λ for $\lambda < 1$. The increase of the drop deformation with the viscosity ratio λ was reported in previous literature [53] for a droplet moving in a cylindrical tube. Figure 6.19(b) plots the droplet velocity U_x as a function of the viscosity ratio. The droplet velocity U_x shows a monotonic decrease with the increase of the viscosity ratio λ which qualitatively agree with the computational results by Martinez and Udell [53] as well as the experimental findings by Ho and Leal [39] for a viscous drop moving in a cylindrical tube.

For comparison, we calculate the deformation and velocity of a droplet moving in a cylindrical tube. We consider a droplet with size $a = 0.914$ and capillary number $Ca = 0.1$ translating in a tube with radius $R = 1$ (which subscribes the square channel). For both the channel and tube, the droplet deformation and velocity at

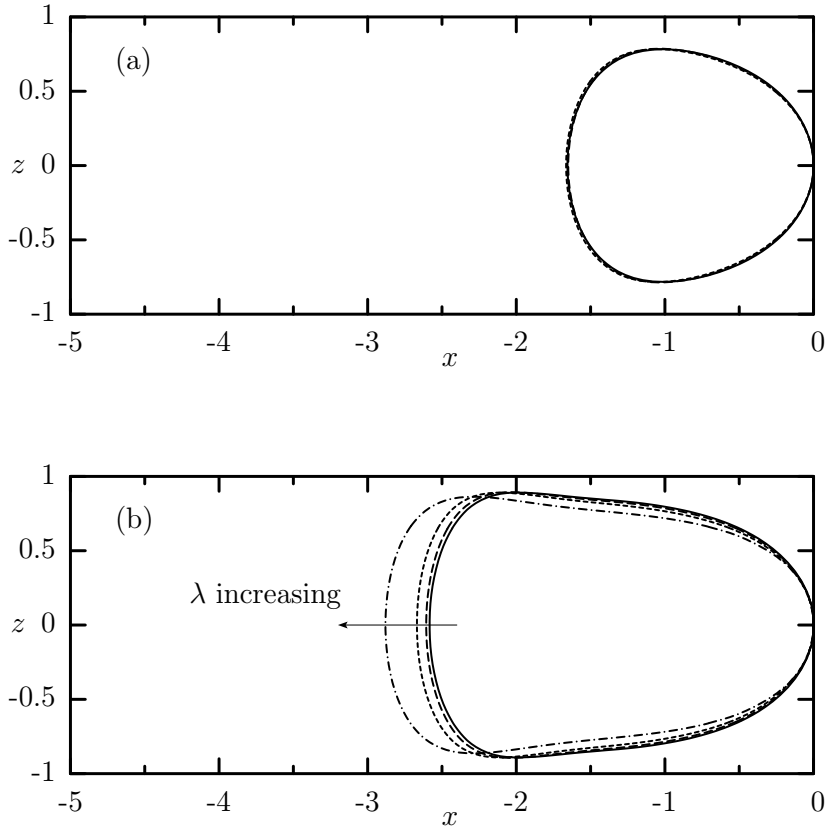

Figure 6.17: Variation in droplet profile with the viscosity ratio λ at steady state. The upper figure shows a droplet with size $a = 0.8$ and viscosity ratio $\lambda = 0.19, 2.04, 10$. The lower figure shows a droplet with with size $a = 1.03$ and viscosity ratio $\lambda = 0.5, 1, 2.04, 10$. For all cases, the capillary number is $Ca = 0.1$.

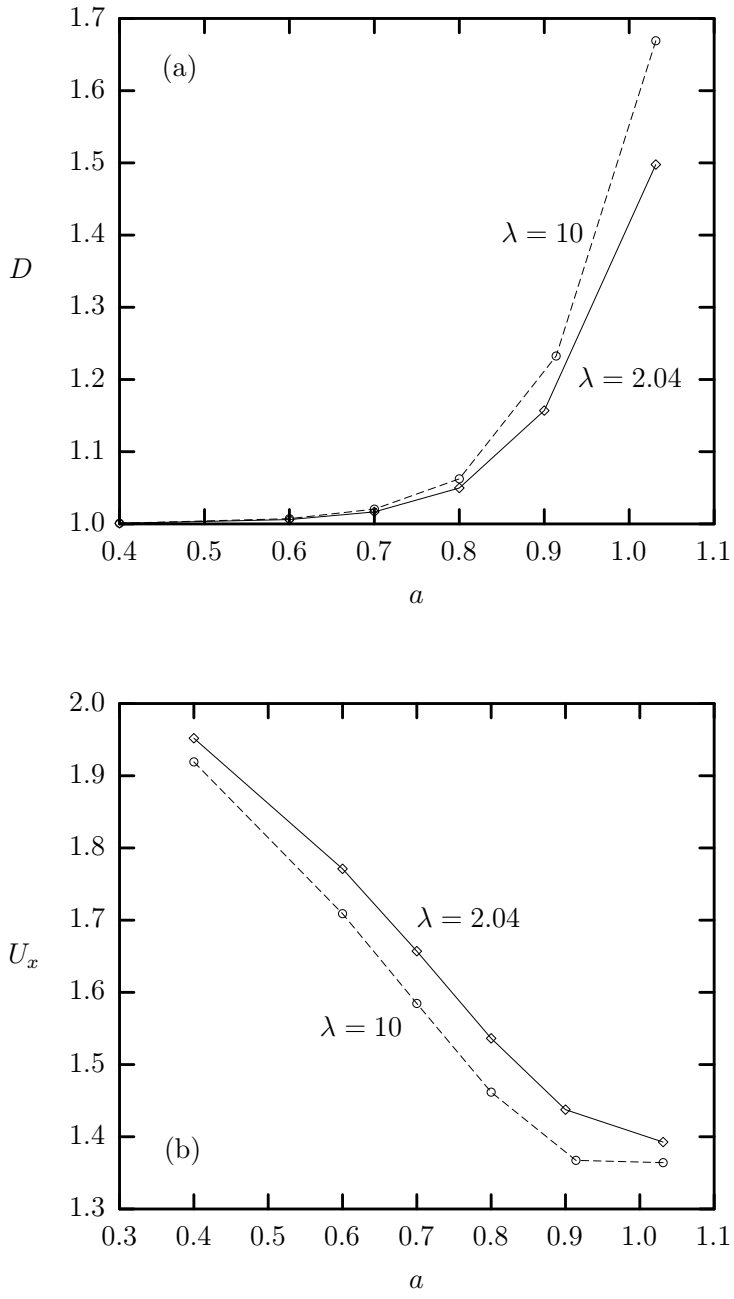

Figure 6.18: Droplet deformation D and velocity U_x as a function of drop size a for viscosity ratio $\lambda = 2.04$ and 10 at steady state. The capillary number for all cases are $Ca = 0.1$.

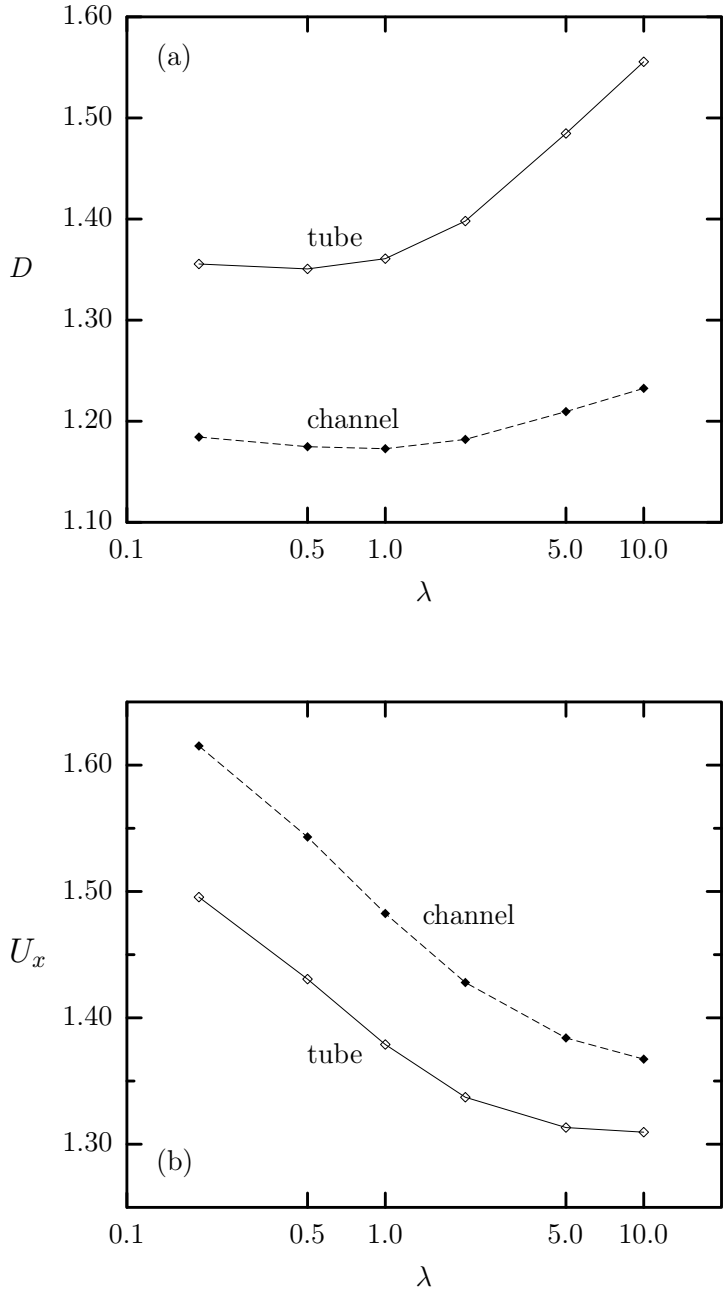

Figure 6.19: Effect of the viscosity ratio λ on the droplet deformation D and velocity U_x at steady state. The results for a droplet translating in a cylindrical tube and a square channel are both presented. For both cases, the droplet size is $a = 0.914$, and the capillary number is $Ca = 0.1$.

steady state are plotted in figure 6.19 as a function of the viscosity ratio. We observe that the droplet experiences a larger deformation in the tube while the droplet speed is higher in the channel for an arbitrary λ. Comparing with the geometry of the cylindrical tube, we note that the extra area in the corner of the square channel allows the suspending fluid to "leak" around the droplet, and thus largely reduces the shear acting on the droplet interface. Hence, the deformation of a droplet moving in a channel is relatively smaller than that in a tube. Figure 6.20(a) shows the steady-state droplet shape at the intersection with the plane $y = 0$ for both the square channel and the cylindrical tube. In this figure, the droplet demonstrates a less deformed shape in the channel flow. Figure 6.20(b) shows the droplet profile at the intersection with plane $x = x_{min}$, where x_{min} is the x coordinate of the point on the droplet interface with the shortest distance to the channel/tube wall. In this figure, profiles for the channel and the droplet inside are denoted by solids lines, while those for the tube and the droplet inside are expressed in dashes. We note that the droplet blocks 56.8% of the cross-sectional area of the channel while 61.6% of the cross-sectional area of the tube is occupied by the drop. The less blocking of the droplet to the channel flow leads to the higher droplet speed in the channel.

6.6 Droplet Released at a Position Off the Centerline

So far, we have discussed the deformation and translation of a droplet moving along the centerline of the square channel. In this section, we investigate the motion of a droplet set free at an initial position off the centerline. As a complement to the

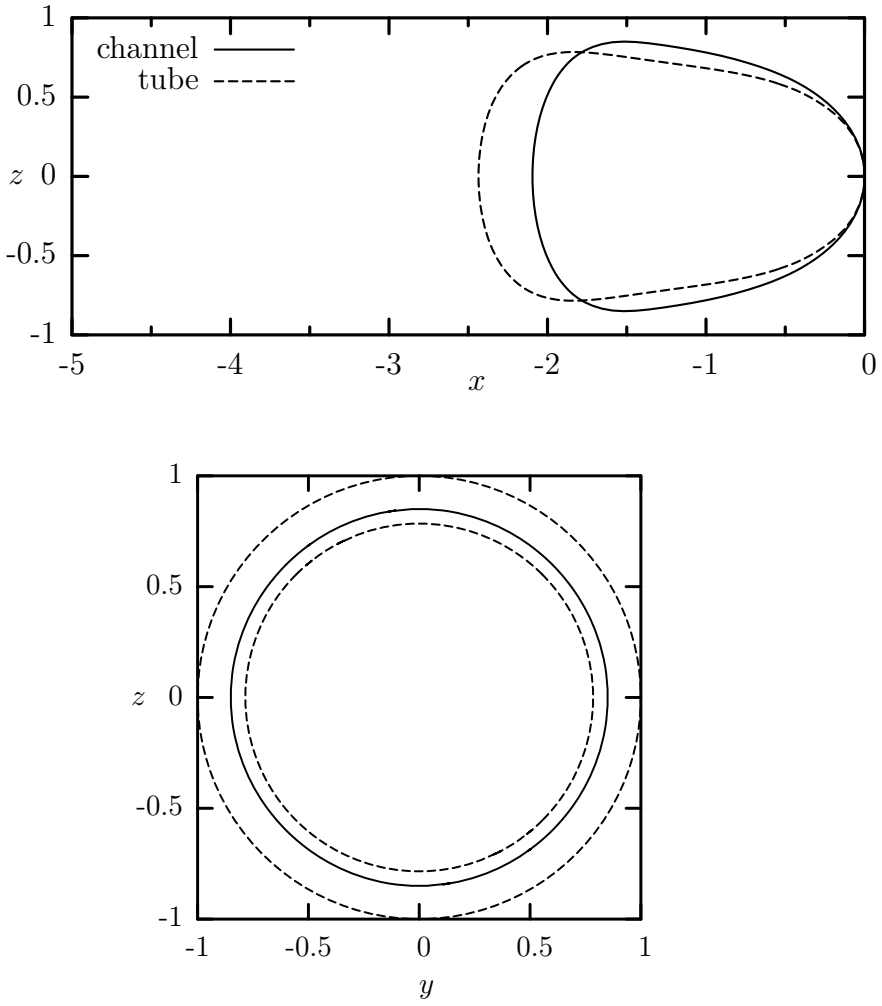

Figure 6.20: Comparison of droplet profiles for a droplet with size $a = 0.914$ in a cylindrical tube and a square channel at steady state. For both cases, the capillary number is $Ca = 0.1$ and the viscosity ratio is $\lambda = 10$. The profiles at plane $y = 0$ and $x = x_{min}$ are plotted. Note that x_{min} is the x coordinate of the point on the droplet interface with the shortest distance to the channel/tube wall.

previous sections, here we focus on the droplet cross-stream migration behavior.

We first investigate the influence of the droplet size on the droplet migration. In figure 6.21, the position of the droplet centroid is plotted as a function of time for capillary number $Ca = 0.125$ and viscosity ratio $\lambda = 1$. Droplet sizes $a = 0.25, 0.4, 0.7$ are considered. We note that a smaller droplet (e.g. $a = 0.25$) nearly maintains its original distance to the centerline while larger droplets migrates significantly towards the center.

At low Reynolds number, the cross-stream migration of a droplet in the channel results from the droplet deformation, which is again directly related to the capillary number. In figure 6.22, we plot the droplet position z_c as a function of time under the influence of the capillary number. Results for different drop sizes are presented (i.e., $a = 0.25$ and 0.7). For a given size, a more deformable droplet (i.e., with larger capillary number) migrates faster to the center of the channel. Figure 6.23 shows the geometry of the droplet interface for a deformed droplet with size $a = 0.7$. The interfacial shapes at the maximum deformation are shown for each capillary number we consider. As predicted, the droplet with more deformed shape experiences a faster cross-stream migration.

We now investigate the influence of the viscosity ratio on the droplet migration for a given size and capillary number. Figure 6.24 shows the time evolution of the droplet location z_c for different viscosity ratios. We note that for a moderate size (e.g. $a = 0.7$), a less viscous droplet migrates faster towards the channel centerline. The effect of the viscosity ratio is also examined for a relatively small droplet with $a = 0.25$ for capillary number $Ca = 0.125$ as shown in figure 6.25. We found

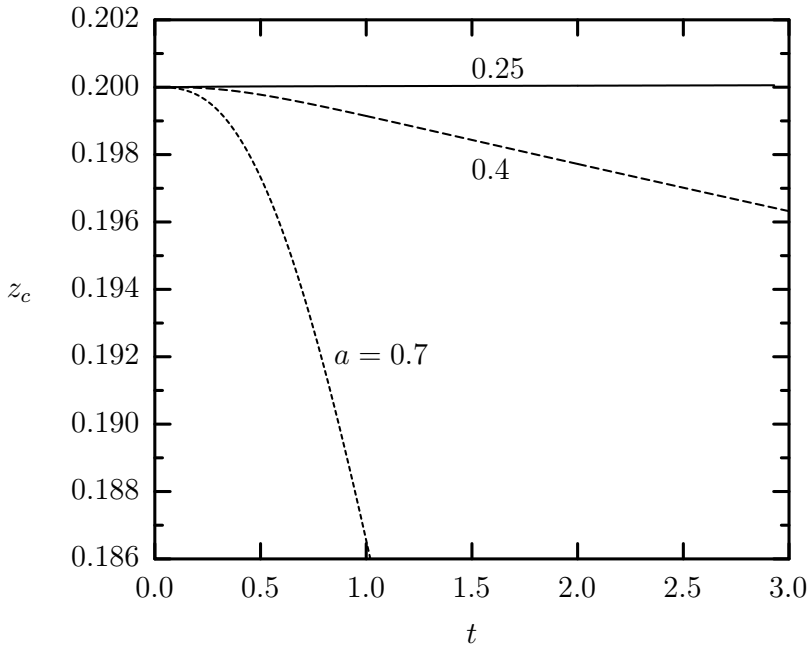

Figure 6.21: Influence of drop size a on the droplet centroid location z_c. Sizes $a = 0.25, 0.4, 0.7$ are included. For all cases, the capillary number is $Ca = 0.2$ and the viscosity ratio is $\lambda = 1$. The droplet is set free at $z_{c0} = 0.2$.

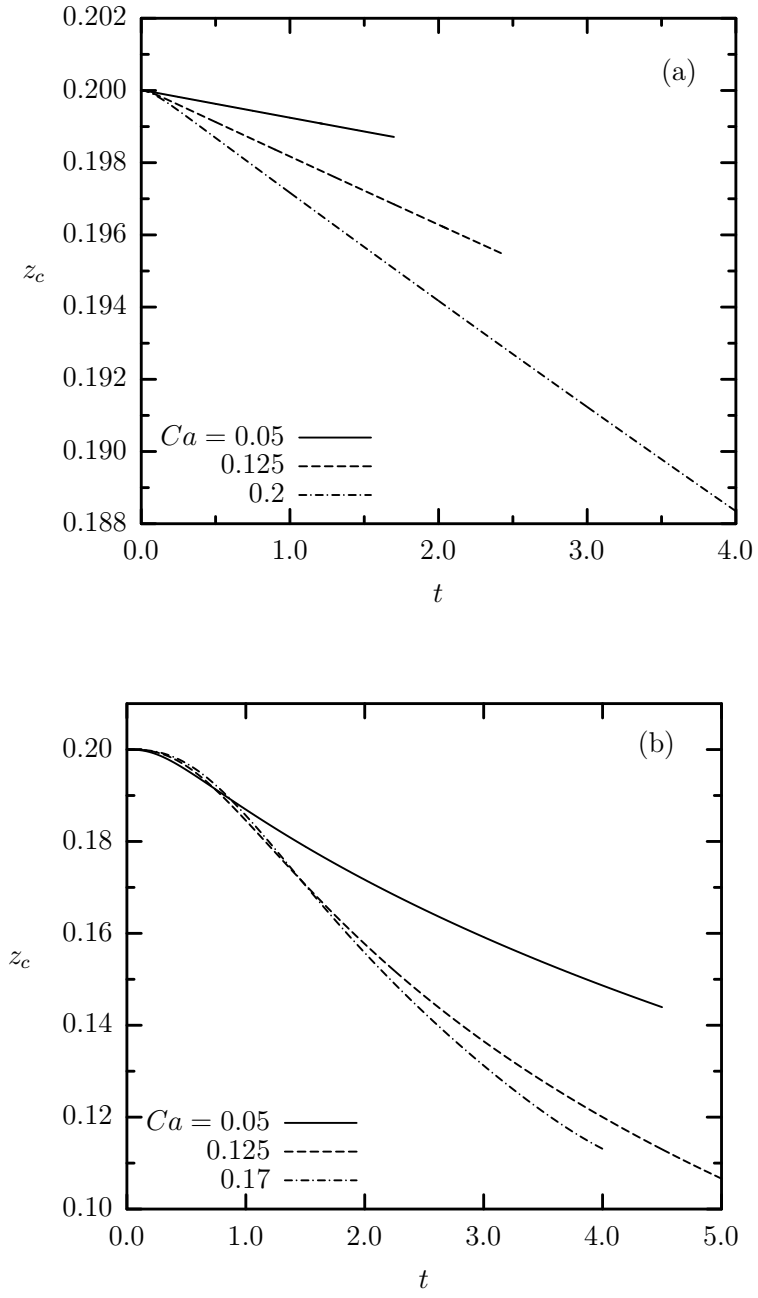

Figure 6.22: Influence of the capillary number Ca on the droplet centroid location z_c. (a) A small droplet with size $a = 0.25$ deforms at capillary numbers $Ca = 0.05, 0.125, 0.2$ and viscosity ratio $\lambda = 0.125$. (b) A droplet with $a = 0.7$ deforms at capillary numbers $Ca = 0.05, 0.125, 0.17$ and viscosity ratio $\lambda = 1$. The droplet is set free at $z_{c0} = 0.2$.

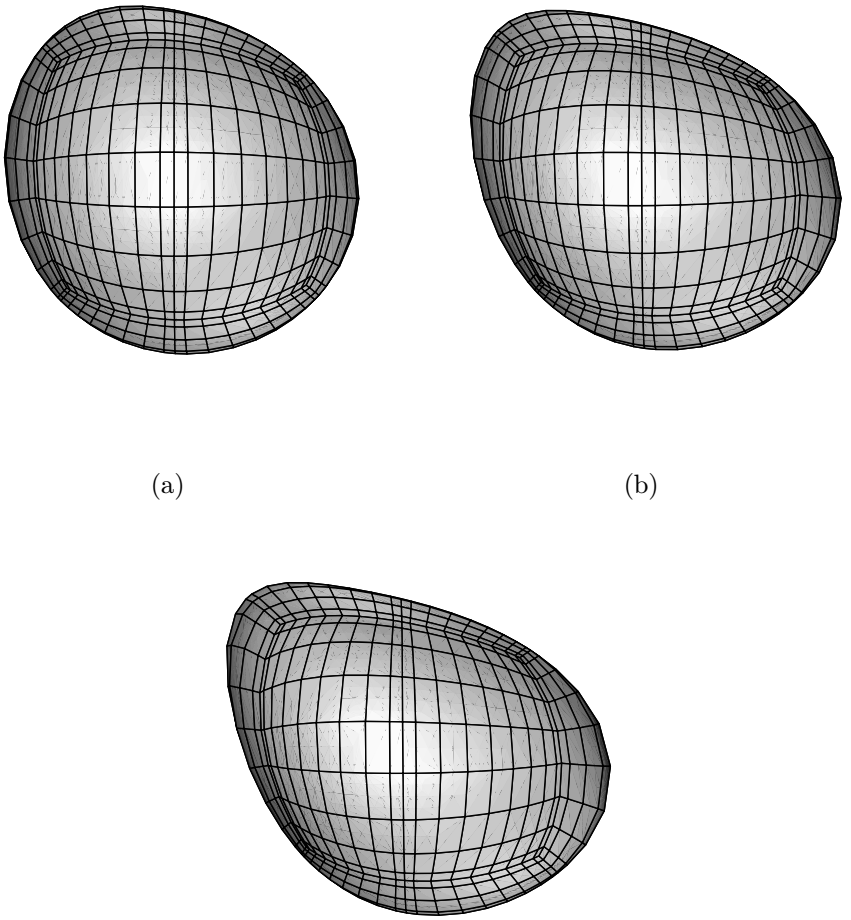

(a) (b)

(c)

Figure 6.23: Three-dimensional profiles of droplets set free at $z_{c0} = 0.2$ with viscosity ratio $\lambda = 1$ and size $a = 0.7$: (a) $Ca = 0.05$ at $t = 0.6$ (b) $Ca = 0.125$ at $t = 1$ and (c) $Ca = 0.2$ at $t = 1.2$. The geometries shown are the most deformed droplet interfaces.

that a less viscous droplet (i.e., $\lambda = 0.125$) migrates towards the centerline in a noticeable manner, while the droplet with a higher viscosity almost maintains its original distance to the channel centerline.

6.7 Conclusions

In this chapter, we examined the motion of a single droplet in a microfluidic channel filled with another immiscible fluid. We first investigated the influence of the droplet size, capillary number and viscosity on the droplet interfacial shape as well as the droplet translation speed along the channel centerline. We found that as we increase the droplet size, the droplet deformation (i.e., elongation along the flow direction) increases due to the confinement of the channel wall. On the other hand, the droplet speed decreases with the increase of the droplet size due to the larger interfacial area exposed in the region with higher shear force in the channel flow. A higher capillary number is found to incur a larger elongation and a thicker fluid film between the droplet and the channel wall. The effect of the capillary number on the droplet shape is more prominent for large drops. With a fixed droplet size but an elongated shape, the droplet for a larger capillary number blocks less area in the micro-channel. As a result, a higher droplet velocity is achieved. Nevertheless, the effect of the capillary number on the droplet velocity is evident only for droplets with size $a > 0.65$. Our results also indicate that a less viscous droplet moves faster in the channel with other parameters fixed. The droplet speed decreases with the increase of the viscosity ratio, while the droplet deformation shows a monotonic increase with the

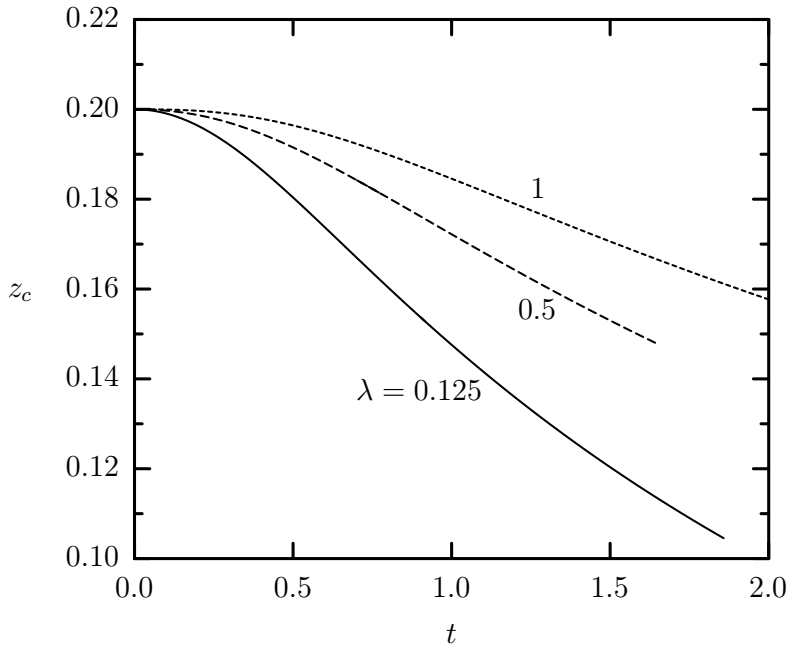

Figure 6.24: Influence of viscosity ratio λ on droplet centroid location z_c. Viscosity ratios $\lambda = 0.125, 0.5, 1$ are included. For all cases, the droplet size is $a = 0.7$ and the capillary number is $Ca = 0.125$. The droplet is set free at $z_{c0} = 0.2$.

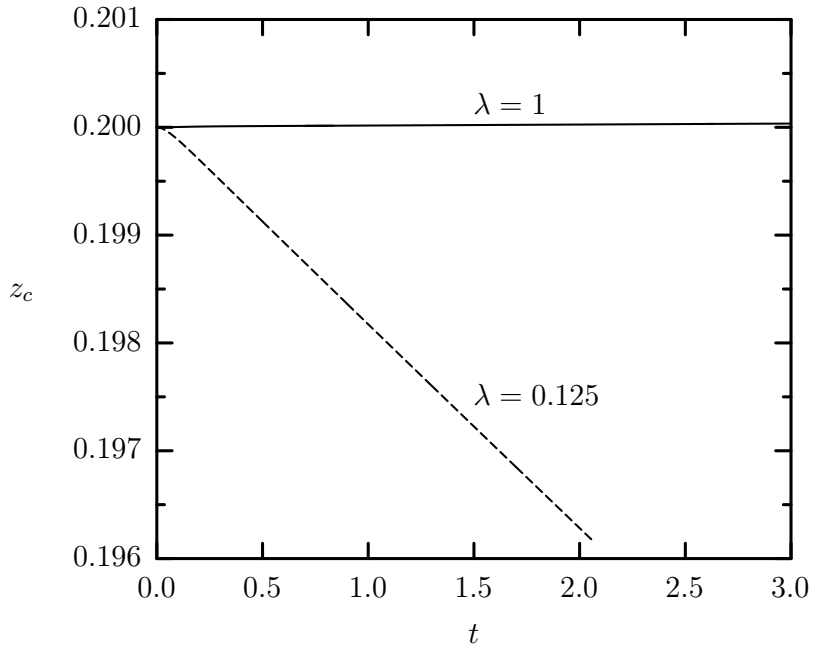

Figure 6.25: Influence of viscosity ratio λ on droplet centroid location z_c. Viscosity ratio $\lambda = 0.125$ and 1 are included. For both cases, the droplet size is $a = 0.25$ and the capillary number is $Ca = 0.125$. The droplet is set free at $z_{c0} = 0.2$.

viscosity ratio for $\lambda \geq 1$. For $\lambda < 1$, the droplet deformation is almost independent on λ. By comparing the droplet behavior in the square channel with that in a cylindrical tube, we found that the droplet deformation is smaller and the droplet speed is higher if the capillary cross-section is square.

The cross-stream motion of the droplet set free at a location off the centerline is also of great interest in microfluidics. We found that a droplet with a moderate size moves fast towards the channel centerline while the migration of a very small droplet is extremely slow. A droplet with a larger capillary number or a smaller viscosity ratio was found to travel faster towards the centerline.

Our numerical study investigates the velocity and shape of a droplet traveling in a microfluidic channel, predicts the influence of the droplet size, capillary number and the viscosity ratio on the droplet behavior, and thus may guide the design or operation of microfluidic devices, especially for droplet sorting devices.

Bibliography

[1] I. B. Bazhlekov, P. D. Anderson and H. E. H. Meijer, Nonsingular boundary integral method for deformable drops in viscous flows. *Phys. Fluids* **16**(4), 1064–1081 (2004).

[2] B. J. Bentley and L. G. Leal, An experimental investigation of drop deformation and breakup in steady, two-dimensional linear flows. *J. Fluid Mech.* **167**, 241–283 (1986).

[3] S. A. Berger, W. Goldsmith, and E. R. Lewis, *Introduction to Bioengineering.* Oxford University Press, Oxford (1996).

[4] Q. C. Bi and T. S. Zhao, Taylor bubbles in miniaturized circular and noncircular channels. *Intl. J. Multiphase Flow* **50**(2), 183–199 (1995).

[5] A. Borhan and J. Pallinti, Buoyancy-driven motion of viscous drops through cylindrical capillaries at small Reynolds numbers. *Ind. Eng. Chem. Res.* **34**, 2750–2761 (1995).

[6] F. P. Bretherton, The motion of long bubbles in tubes. *J. Fluid Mech.* **10**, 166–188 (1961).

[7] C. Canuto, M. Y. Hussaini, A. Quarteroni and T. A. Zang, *Spectral Methods in Fluid Dynamics.* Springer, New York (1998).

[8] P. C. Chan and L. G. Leal, The motion of a deformable drop in a second-order fluid. *J. Fluid Mech.* **92**, 131–170 (1979).

[9] G. B. Chapman and G. R. Cokelet, Model studies of leukocyte-endothelium-blood interactions. I. The fluid flow drag force on the adherent leukocyte. *Biorheology* **33**, 119–138 (1996).

[10] G. B. Chapman and G. R. Cokelet, Model studies of leukocyte-endothelium-blood interactions. II. Hemodynamic impact of leukocytes adherent to the wall of post-capillary vessels. *Biorheology* **34**, 37–56 (1997).

[11] G. B. Chapman and G. R. Cokelet, Flow resistance and drag forces due to multiple adherent leukocytes in postcapillary vessels. *Biophys. J.* **74**, 3292–3301 (1998).

[12] J.-D. Chen, Measuring the film thickness surrounding a bubble inside a capillary. *J. Colloid Interface Sci.* **109**, 314–349 (1986).

[13] M. F. Coughlin and G. W. Schmid-Schönbein, Pseudopod projection and cell spreading of passive leukocytes in response to fluid shear stress. *Biophys. J.* **87**, 2035–2042 (2004).

[14] C. Coulliette and C. Pozrikidis, Motion of an array of drops through a cylindrical tube. *J. Fluid Mech.* **358**, 1–28 (1998).

[15] V. Cristini, J. Blawzdziewicz and M. Loewenberg, An adaptive mesh algorithm for evolving surfaces: simulations of drop breakup and coalescence. *J. Comp. Phy.* **168**, 445–463 (2001).

[16] B. Das, P. C. Johnson, and A. S. Popel, Computational fluid dynamic studies of leukocyte adhesion effects on non-Newtonian blood flow through microvessels. *Biorheology* **37**, 239–258 (2000).

[17] R. H. Davis, Buoyancy-driven viscous interaction of a rising drop with a smaller trailing drop. *Phys. Fluids* **11** (5), 1016–1028 (1999).

[18] K. M. DeBisschop, M. J. Miksis and D. M. Eckmann, Bubble rising in an inclined channel. *Phys. Fluids* **14** (1), 93–106 (2002).

[19] L. Demaio, Y. S. Chang, T. W. Gardner, J. M. Tarbell and D. A. Antonetti, Shear stress regulates occludin content and phosphorylation. *Am. J. Physiol. Heart Circ. Physiol.* **281**, H105–H113 (2001).

[20] P. Dimitrakopoulos and J. J. L. Higdon, Displacement of fluid droplets from solid surfaces in low-Reynolds-number shear flows. *J. Fluid Mech.* **336**, 351–378 (1997).

[21] P. Dimitrakopoulos and J. J. L. Higdon, On the displacement of three-dimensional fluid droplets from solid surface in low-Reynolds-number shear flows. *J. Fluid Mech.* **377**, 189–222 (1998).

[22] P. Dimitrakopoulos, Displacement of fluid droplets from solid surfaces. Ph.D. thesis, University of Illinois (1998).

[23] P. Dimitrakopoulos and J. J. L. Higdon, On the gravitational displacement of three-dimensional fluid droplets from inclined solid surfaces. *J. Fluid Mech.* **395**, 181–209 (1999).

[24] P. Dimitrakopoulos and J. J. L. Higdon, On the displacement of three-dimensional fluid droplets adhering to a plane wall in viscous pressure-driven flows. *J. Fluid Mech.* **435**, 327–350 (2001).

[25] P. Dimitrakopoulos and J. J. L. Higdon, On the displacement of fluid bridges from solid surfaces in viscous pressure-driven flows. *Phys. Fluids* **15**(10), 3255–3258 (2003).

[26] J. A. Frangos, S. G. Eskin, L. V. McIntire and C. L. Ives, Flow effects on prostacyclin production by cultured human-endothelial cells. *Science* **227**, 1477–1479 (1985).

[27] J. A. Frangos, T. Y. Huang and C. B. Clark, Steady shear and step changes in shear stimulate endothelium via independent mechanisms - Superposition of transient and sustained nitric oxide production. *Biochem. Biophys. Res. Commun.* **224**, 660–665 (1996).

[28] D. P. Gaver and S. Kute, A theoretical model study of the influence of fluid stresses on a cell adhering to a microchannel wall. *Biophys. J.* **75**, 721–733 (1998).

[29] M. D. Giavedoni and F. A. Saita, The axisymmetric and plane cases of a gas phase steadily displacing a Newtonian liquid - a simultaneous solution of the governing equations. *Phys. Fluids* **9**, 2420–2428 (1997).

[30] M. D. Giavedoni and F. A. Saita, The rear meniscus of a long bubble steadily displacing a Newtonian liquid in a capillary tube. *Phys. Fluids* **11**, 786–794 (1997).

[31] A. J. Goldman, R. G. Cox and H. Brenner, Slow viscous motion of a sphere parallel to a plane wall. Part I. Motion through a quiescent liquid. *Chem. Engng Sci.* **22**, 637–651 (1967).

[32] S. Guido and M. Villone, Three-dimensional shape of a drop under simple shear flow. *J. Rheol.* **43**(2), 395–415 (1998).

[33] J. Happel and H. Brenner, *Low Reynolds Number Hydrodynamics*. Prentice Hall, Englewood Cliffs (1965)

[34] A. L. Hazel and T. J. Pedley, Vascular endothelial cells minimize the total force on their nuclei. *Biophys. J.* **78**, 47–54 (2000).

[35] A. L. Hazel and M. Heil, The steady propagation of a semi-infinite bubble into a tube of elliptical or rectangular cross-section. *J. Fluid Mech.* **470**, 91–114 (2002).

[36] B. P. Helmke, R. D. Goldman and P. F. Davies, Rapid displacement of vimentin intermediate filaments in living endothelial cells exposed to flow. *Circ. Res.* **86**, 745–752 (2000).

[37] J. J. L. Higdon and G. P. Muldowney, Resistance functions for spherical particles, droplets and bubbles in cylindrical tubes. *J. Fluid Mech.* **298**, 193–210 (1995).

[38] J. J. L. Higdon, Stokes flow in arbitrary two-dimensional domains: shear flow over ridges and cavities. *J. Fluid Mech.* **159**, 195–226 (1985).

[39] B. P. Ho and L. G. Leal, The creeping motion of liquid drops through a circular tube of comparable diameter. *J. Fluid Mech.* **71**, 361–383 (1975).

[40] S. R. Hodges and O. E. Jensen, Spreading and peeling dynamics in a model of cell adhesion. *J. Fluid Mech.* **460**, 381–409 (2002).

[41] S. R. Hodges, O. E. Jensen and J. M. Rallison, The motion of a viscous drop through a cylindrical tube. *J. Fluid Mech.* **501**, 279–301 (2004).

[42] T. K. Hsiai, S. K. Cho, P. K. Wong, M. Ing, A. Salazar, A. Sevanian, M. Navab, L. L. Demer and C. M. Ho, Monocyte recruitment to endothelial cells in response to oscillatory shear stress. *FASEB J.* **17**, 1648–1657 (2003).

[43] H. J. Keh and P. Y. Chen, Slow motion of a droplet between two parallel plane walls. *Chem. Eng. Sci.* **56**, 6863-6871 (2001).

[44] W. B. Kolb and R. L. Cerro, Coating the inside of a capillary of square cross section. *Chem. Eng. Sci.* **46** (9), 2181–2195 (1991).

[45] W. B. Kolb and R. L. Cerro, Film flow in the space between a circular bubble and a square tube. *J. Colloid Interface Sci.* **A 159**, 302–311 (1993).

[46] W. B. Kolb and R. L. Cerro, The motion of long bubbles in tubes of square cross section. *Phys. Fluids* **A 5** (7), 1549–1557 (1993).

[47] D. R. Link, S. L. Anna, D. A. Weitz and H. A. Stone, Geometrically mediated breakup of drops in microfluidic devices. *Phys. Rev. Letters* **92** (5), 054503 (2004).

[48] X. H. Liu and X. Wang, The deformation of an adherent leukocyte under steady shear flow: a numerical study. *J. Biomech.* **37**, 1079–1085 (2004).

[49] M. Loewenberg and E. J. Hinch, Numerical simulation of a concentrated emulsion in shear flow. *J. Fluid Mech.* **321**, 395–419 (1996).

[50] M. Loewenberg and E. J. Hinch, Collision of two deformable drops in shear flow. *J. Fluid Mech.* **338**, 299–315 (1997).

[51] G. Q. Lu and C. Y. Wang, Electrochemical and flow characterization of a direct methanol fuel cell. *J. Power Sources* **134**, 33–40 (2004).

[52] J. Magnaudet, S. Takagi and D. Legendre, Drag, deformation and lateral migration of a buoyant drop moving near a wall. *J. Fluid Mech.* **476**, 115–157 (2003).

[53] M. J. Martinez and K. S. Udell, Axisymmetric creeping motion of drops through circular tubes. *J. Fluid Mech.* **210**, 565–591 (1990).

[54] S. Mortazavi and G. Tryggvason, A numerical study of the motion of drops in Poiseuille flow. Part 1. Lateral migration of one drop. *J. Fluid Mech.* **71**, 361–383 (1975).

[55] G. P. Muldowney and J. J. L. Higdon, A spectral boundary element approach to three-dimensional Stokes flow. *J. Fluid Mech.* **298**, 167–192 (1995).

[56] N. A. N'Dri, W. Shyy, and R. Tran-Soy-Tay, Computational modeling of cell adhesion and movement using a continuum-kinetics approach. *Biophys. J.* **85**, 2273–2286 (2003).

[57] W. L. Olbricht and D. M. Kung, The deformation and breakup of liquid drops in low Reynolds number flow through a capillary. *Phys. Fluids A* **4**(7), 1347–1354 (1992).

[58] M. E. O'Neill and K. Stewarson, On the slow motion of a sphere parallel to a nearby plane wall. *J. Fluid Mech.* **27**, 706–724 (1967).

[59] A. S. Popel and P. C. Johnson, Microcirculation and hemorheology. *Ann. Rev. Fluid Mech.* **37**, 43–59 (2005).

[60] C. Pozrikidis, *Boundary Integral and Singularity Methods for Linearized Viscous Flow.* Cambridge University Press, Cambridge (1992).

[61] C. Pozrikidis, Shear flow over a protuberance on a plane wall. *J. Eng. Math.* **31**, 29–42 (1997).

[62] C. Pozrikidis, Effect of pressure gradient on viscous shear flow past an axisymmetric depression or protuberance on a plane wall. *Comp. Fluids* **29**, 617–637 (2000).

[63] C. Pozrikidis, Interfacial dynamics for Stokes flow. *J. Comput. Phys.* **169**, 250–301 (2001).

[64] J. M. Rallison, A numerical study of the deformation and burst of a viscous drop in general shear flows. *J. Fluid Mech.* **109**, 465–482 (1981).

[65] T. C. Ransohoff and C. J. Radke, Weeping flow around nonwetting bubbles trapped in constricted noncircular pores. PCH,*PhysicoChem. Hydrodyn.* **8**, 255–263 (1987).

[66] J. Ratulowski and H. Chang, Transport of gas bubbles in capillaries. *Phys. Fluids* **A 1**(10), 1642–1655 (1989).

[67] N. Resnick, H. Yahav and A. Shay-Salit, Fluid shear stress and the vascular endothelium: for better and for worse. *Prog. Biophys. Molecular* **81**, 177–199 (2003).

[68] G. Segre and A. Silberberg, Behavior of macroscopic rigid spheres in Poiseuille flow. Part 1. Determination of local concentration by statistical analysis of particle passages through crossed light beams. *J. Fluid Mech.* **14**, 115–135 (1962).

[69] G. Segre and A. Silberberg, Behavior of macroscopic rigid spheres in Poiseuille flow. Part 2. Experimental results and interpretation. *J. Fluid Mech.* **14**, 136–157 (1962).

[70] M. Shapira and S. Haber, Low Reynolds number motion of a droplet in shear flow including wall effects. *Intl J. Multiphase Flow* **16**, 305–321 (1990).

[71] M. Shapira and S. Haber, Low Reynolds number motion of a droplet between two parallel plates. *Intl J. Multiphase Flow* **14**, 483–506 (1988).

[72] S. Sheikh, G. E. Rainger, Z. Gale, M. Rahman and G. B. Nash, Exposure to fluid shear stress modulates the ability of endothelial cells to recruit neutrophils

in response to tumor necrosis factor-a: a basis for local variations in vascular sensitivity to inflammation. *Blood* **102**, 2828–2834 (2003).

[73] E. I. Shen and K. S. Udell, A finite element study of low Reynolds number two-phase flow in cylindrical tubes. *Trans. ASME: J. Appl. Mech.* **52**, 253–256 (1985).

[74] H. W. Sill, Y. S. Chang, J. R. Artman, J. A. Frangos, T. M. Hollis and J. M. Tarbell, Shear stress increases hydraulic conductivity of cultured endothelial monolayers. *Am. J. Physiol. Heart Circ. Physiol.* **268**, H535–H543 (1995).

[75] J. R. Smart and D. T. Leighton, Jr., Measurement of the drift of droplet due to the presence of a plane. *Phys. Fluids* **A 3** (1), 21–28 (1991).

[76] H. Song, J. D. Tice and R. F. Ismagilov, A microfluidic system for controlling reaction networks in time. *Angew. Chem. Int. Ed.* **42** (7), 767–772 (2003).

[77] M. Sugihara-Seki and R. Skalak, Force acting on spheres adhered to a vessel wall. *Biorheology* **34**, 249–260 (1997).

[78] M. Sugihara-Seki, Flow around cells adhered to a microvessel wall. I. Fluid stresses and forces acting on the cells. *Biorheology* **37**, 341–359 (2000).

[79] M. Sugihara-Seki, Flow around cells adhered to a microvessel wall. II. Comparison to flow around adherent cells in channel flow. *Biorheology* **38**, 3–13 (2001).

[80] M. Sugihara-Seki and G. W. Schmid-Schönbein, The fluid shear stress distribution on the membrane of leukocytes in the microcirculation. *J. Biomech. Eng.* **125**, 628–638 (2003).

[81] F. Takemura, S. Takagi, J. Magnaudet and Y. Matsumoto, Drag and lift forces on a bubble rising near a vertical wall in a viscous liquid. *J. Fluid Mech.* **461**, 277–300 (2002).

[82] F. Takemura and J. Magnaudet, The transverse force on clean and contaminated bubbles rising near a vertical wall at moderate Reynolds number. *J. Fluid Mech.* **495**, 235–253 (2003).

[83] F. Takemura, Migration velocities of spherical solid particles near a vertical wall for Reynolds number for 0.1 to 5. *Phys. Fluids* **16**(1), 204–207 (2004).

[84] Y. Tan, J. S. Fisher, A. I. Lee, V. Cristini and A. P. Lee, Design of microfluidic channel geometries for the control of droplet volume, chemical concentration, and sorting. *Lab Chip* **4**, 292–298 (2004).

[85] G. I. Taylor, The viscosity of a fluid containing small drops of another fluid. *Proc. Roy. Soc.* A **138**, 41–48 (1932).

[86] T. D. Taylor and A. Acrivos, On deformation and drag of a falling viscous drop at low Reynolds number. *J. Fluid Mech.* **18**, 466–476 (1964).

[87] T. C. Thulasidas, M. A. Abraham and R. L. Cerro, Bubble-train flow in capillaries of circular and square cross section. *Chem. Engng. Sci.* **50**(2), 183–199 (1995).

[88] T. M. Tsai and M. J. Miksis, Dynamics of a drop in a constricted capillary tube. *J. Fluid Mech.* **274**, 197–217 (1994).

[89] W. S. J. Uijttewaal, E. J. Nijhof and R. M. Heethaar, Droplet migration, deformation, and orientation in the presence of a plane wall: A numerical study compared with analytical theories. *Phys. Fluids* **A 5** (4), 819–825 (1993).

[90] W. S. J. Uijttewaal and E. J. Nijhof, The motion of a droplet subjected to linear shear flow including the presence of a plane wall. *J. Fluid Mech.* **302**, 45–63 (1995).

[91] P. Vasseur and R. G. Cox, The lateral migration of spherical particles sedimenting in a stagnant bounded fluid. *J. Fluid Mech.* **80**, 561–591 (1977).

[92] Y. Wang, Numerical studies of Stokes flow in confined geometries. M.S. thesis, University of Maryland (2004).

[93] Y. Wang and P. Dimitrakopoulos, Normal force exerted on vascular endothelial cells. *Phys. Rev. Lett.* **96**, 028106 (2006).

[94] Y. Wang and P. Dimitrakopoulos, Nature of the hemodynamic forces exerted on vascular endothelial cells or leukocytes adhering to the surface of blood vessels. *Phys. Fluids* **18**, 087107 (2006).

[95] Y. Wang and P. Dimitrakopoulos, A three-dimensional spectral boundary element algorithm for interfacial dynamics in Stokes flow. *Phys. Fluids* **18**, 082106 (2006).

[96] S. Weinbaum, X. Zhang, Y. Han, H. Vink and S. C. Cowin, Mechanotransduction and flow across the endothelial glycocalyx. *Proc. Natl. Acad. Sci. USA* **100**, 7988–7995 (2003).

[97] H. Wong, C. J. Radke and S. Morris, The motion of long bubbles in polygonal capillaries. Part 1. Thin films. *J. Fluid Mech.* **292**, 71–94 (1995).

[98] H. Wong, C. J. Radke and S. Morris, The motion of long bubbles in polygonal capillaries. Part 2. Drag, fluid pressure and fluid flow. *J. Fluid Mech.* **292**, 95–110 (1995).

[99] C. Yih, *Fluid Mechanics* West River Press, Michigan (1979).

[100] G. K. Youngren and A. Acrivos, On the shape of a gas bubble in a viscous extensional flow. *J. Fluid Mech.* **76**, 433–442 (1976).

[101] L. Zeng, S. Balachandar and P. Fischer, Wall-induced forces on a rigid sphere at finite Reynolds number. *J. Fluid Mech.* **536** , 1–25 (2005).

[102] A. Z. Zinchenko, M. A. Rother and R. H. Davis, A novel boundary-integral algorithm for viscous interaction of deformable drops. *Phys. Fluids* **9**(6), 1493–1511 (1997).

[103] A. Z. Zinchenko and R. H. Davis, A multipole-accelerated algorithm for close interaction of slightly deformable drops. *J. Comput. Phys.* **207**, 695–735 (2005).

Vita

Yechun Wang was born in October 1980, in Nanchang, China. She attended Nanchang No.2 High School from September 1994 to July 1997. She then moved to Shanghai, China and got enrolled at the East China University of Science and Technology (ECUST) in the School of Chemical Engineering, in September 1997. In July 2001, she graduated with honor and received her Bachelor's degree in Chemical Engineering and Technology. Her undergraduate thesis focused on the carbon dioxide removal process in the ammonia production with the title of "Absorption of CO_2 into piperazine activated methyldiethanolamine solution under elevated pressures". In September 2002, she was enrolled at the graduate program of the Department of Chemical and Biomolecular Engineering at the University of Maryland at College Park. She conducted research in the area of computational fluid dynamics under the guidance of Professor Panagiotis Dimitrakopoulos. Her graduate work involved the study of the hemodynamic forces exerted on biological cells in blood vessels, the development of numerical techniques in interfacial dynamics problems, and the physical problems related to microfluidics. In December 2004, she received her Master of Science degree in Chemical Engineering with thesis "Numerical studies of Stokes flow in confined geometries". In January 2007, she defended her dissertation for the Doctor of Philosophy in Chemical Engineering.